## Mémoire

**Auteur :** Robin, Hadrien
**Promoteur(s) :** Soret, Lauriane
**Faculté :** Faculté des Sciences
**Diplôme :** Master en sciences spatiales, à finalité approfondie
**Année académique :** 2022-2023
**URI/URL :** http://hdl.handle.net/2268.2/18747

# *Time Variations of the Martian Dayglow*


## Hadrien ROBIN

**Promotor: Dr. Lauriane SORET**

Master in Space Sciences

**Department of Astrophysics, Geophysics, and Oceanography**

**Faculty of Sciences**

**University of Liège**

**Belgium**


**August 16, 2023**

# Contents

# *Time Variations of the Martian Dayglow*

Hadrien ROBIN

August 16, 2023

# Acknowledgements

I would like to acknowledge the people who have helped me in the making of my thesis. This work would not exist without them.

First, I would like to express my most sincere gratefulness to Dr. Lauriane Soret. She offered me the possibility of working under her guidance when I needed it the most. I have learned so much from her expertise and work on the topic of the Martian airglow.

I am deeply grateful to Dr. Benoît Hubert for seeking and finding a thesis topic amongst his peers. I would not have been able to have a proper guidance for my thesis without him. His advices and help throughout the year have been invaluable.

I would like to sincerely thank my parents for the important role they played throughout the redaction of this thesis, my studies, and my life in general. They constantly believed in me, loved me, and supplied with ample amounts of coffee for as long as I can remember. Thank you for everything.

I am profoundly grateful for the support my beloved girlfriend, Ness, has offered me over the last six years. I would not have been able to finish my bachelor and my master degrees without her presence at my side.

Last but not least, I would like to mention the many friends with whom I have shared my academic journey. Those who provided their advice for this work, those who helped me in my darkest moments, and those with whom we leave our fate to the roll of a die.

# 1. Introduction

The concept of airglow covers a series of phenomena of different origins, yet of similar expressions. The term refers to any non-thermal radiation emitted by an atmosphere, induced by the sunlight. They differ from auroral emissions, which find their origin in the interaction of solar winds with a magnetosphere. The timescale of the different emission processes involved can vary significantly. The presence or absence of sunlight can lead to different atomic excitation processes to dominate, hence, a distinction is made between dayglow and nightglow. The first mention of airglow in a scientific context was made by Anders Ångström in 1868 [Ångström, 1868], while the first quantitative measurements of the phenomenon were made by Gavin J. Burns in 1899 (according to [Silverman, 1970]) and Simon Newcomb in 1901. The latter incorrectly attributed its cause to be a multitude of imperceptible faint stars [Newcomb, 1901]. While airglows have also been observed on Earth [Krasovskij and Sefov, 1965] and Venus [Krasnopolsky, 2010], the present work will focus exclusively on the Martian dayglow.

Airglows are composite emissions resulting from complex photochemistry networks. Different atoms, molecules, and even ions will emit radiation at specific wavelengths, thus allowing their identification. The shape of the airglow spectrum will vary depending on the local atmospheric composition, the thermodynamic state of the atmosphere and the conditions of the incoming solar energy. For example, as the sunlight penetrates the atmosphere, the amount of solar energy available for absorption decreases, while the atmospheric density increases. Thus, each emission occurs at a specific wavelength and reaches its maximum at a specific altitude. This behaviour can clearly be observed on a plot of the intensity of the emission of a given wavelength, as a function of the altitude. This kind of figures, called limb profiles, can provide interesting information on the vertical structure of the atmosphere.

Measurement of the emissions in the Martian airglow can provide much information on the state of the atmosphere and its variation over time. Atmospheric densities and temperatures can be retrieved from dayglow limb profiles, even at altitudes where in-situ measurements cannot be performed [Aoki et al., 2022]. In the same manner, $CO_2$ density has been retrieved using a combination of airglow observations, photochemistry model and orbital solar EUV measurements [Gkouvelis et al., 2018]. While a correlation between the insolation and the airglow brightness has already been identified, a complete description of the seasonal and annual variations has yet to be made. This work intends to accomplish that, as it could lead to an improvement of the evaluation of the short term atmospheric variations.

There are two possible ways of observing the airglow emission from an orbiter. Either track the emission at a fixed altitude over time in a "limb tracking" mode, or lock the spectrometer line of sight in a direction and scan through the atmosphere to produce "inertial" observations. Figure 1.0.1 illustrates the situation with the example of the Venus Express orbiter scanning the atmosphere of Venus in inertial mode. Around the planet are drawn the profiles of the emission density. This quantity is integrated over the line of sight of the spectrometer as it scanned the atmosphere, resulting in a measurement of the intensity of the airglow, as show on the left side of the figure. Some precautions need to be taken when comparing one quantity to the other. The emission density is the amount of photons emitted in a volume over a given period, while the airglow intensity is only the amount of photons received by the spectrometer over a given period coming from the line of sight of the instrument. Thus, when the spectrometer is aimed at a point at a given altitude over the surface, it is not necessary the altitude at which all observed photons have been emitted. This results in smoother intensity profiles than their associated emission density profiles. Peaks of intensity are also lower than their emission equivalents, as the line of sight will cross the layer at which the peak of emission occurs, when looking at lower layers in the atmosphere. [Soret et al., 2022]

The most common calendar on Earth is the Gregorian calendar, which is based on the rotations of the Earth on itself and around the Sun. This system is not very useful when working on the seasonal and daily cycles of other planets. Thus, a Martian timekeeping system has been agreed upon and is often used to simplify discussions concerning the time on Mars. A rotation of Mars on itself relative to the Sun is called a Sol, and lasts 24 hours 39 minutes and 35 seconds, slightly

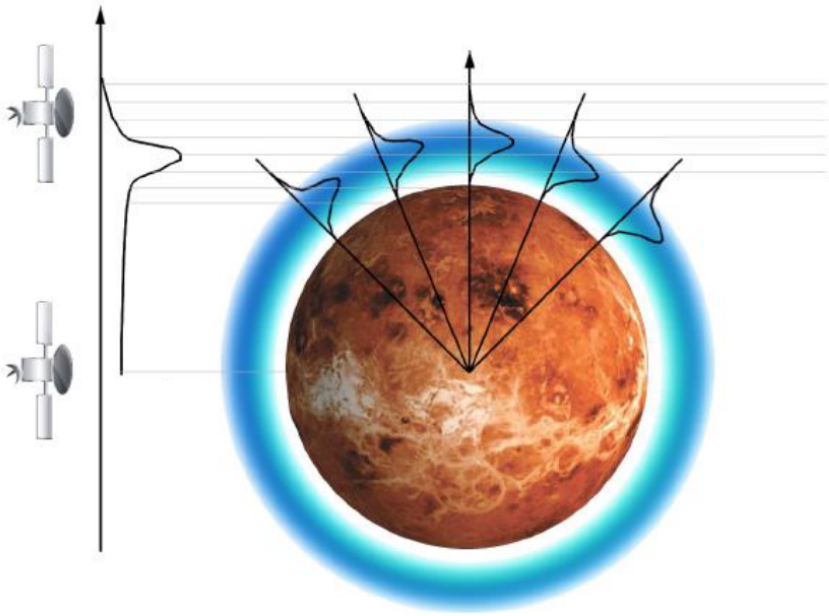

Figure 1.0.1: Schematisation of the observation process of the Venusian airglow by the Venus Express orbiter in inertial mode. The curves on the right side of the figure are the emission profile at different locations, while the one on the left is the resulting intensity measured by the orbiter. Adapted from Cox, 2010 (Thesis), via [Stiepen, 2014].

more than a day on Earth. Sols are divided in 24 fractions called local Martian hours. Noon occurs on Mars when the Sun is at his highest point in the sky and correspond to a local time of 12 hours. A Martian year corresponds to a full rotation of the planet around the Sun and lasts equivalently 668 sols, 687 days or 1.88 Earth years. Martian years start when the planet is at the vernal equinox, the point at which the planet's orbit crosses its equatorial plane. Figure 1.0.2 shows a diagram of the Martian orbit. MY1, the first Martian year in the numbering system, has been chosen arbitrarily and began on April 11, 1955. [Piqueux et al., 2015]

The solar longitude Ls is the angle formed between the planet, the Sun and the vernal point. This metric is more significant than the Sols when analysing seasonal cycle, as the planet seasons have different lengths, but always correspond to ranges of Ls of 90°. [Allison and McEwen, 2000]

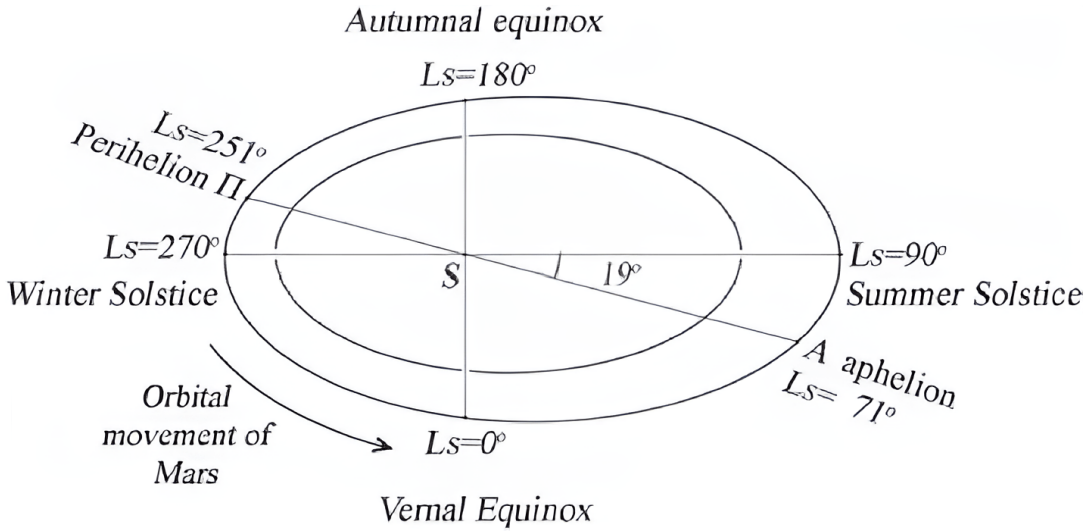


Figure 1.0.2: Diagram of the Martian orbits, with the solstices, equinoxes, perihelion and aphelion indicated. Adapted from [Tarasashvili et al., 2013].

While Mars has a similar rotation rate and obliquity as Earth, it has a much higher eccentricity value of e = 0.0934. This configuration produces a strong asymmetric seasonal cycle, with long southern winters. As a result, a larger amount of the $CO_2$ condenses in the southern polar cap, leading in turn to a decrease of the atmospheric pressure. About 25% of the Martian atmosphere is stored inside the southern polar cap during the aphelion. [Haberle, 2015]

# 2. Martian exploration

Theoretical studies of a hypothetical airglow in the Martian atmosphere started in the 1960s soon after the identification of $CO_2$ in the Martian atmosphere, although the lack of a proper method of determining the atmospheric pressure lead to incorrect hypotheses. It was assumed at the time that the Martian atmosphere was mostly composed of nitrogen with only 10% of $CO_2$, while the atmospheric pressure was in the order of 100mb [Inn, 1964][Owen, 1982].

The first observation of the Martian airglow was made in July 1969 during a fly-by of Mars by the Mariner VI spacecraft. The on-board ultraviolet spectrometer analysed the spectrum emitted by the sunlit atmosphere and identified characteristic emissions of atomic hydrogen, atomic oxygen, ionized carbon dioxide and carbon monoxide [Barth et al., 1969]. This was the first observation of the latter two components in the Martian atmosphere [Owen, 1982].

Mariner VII, the twin mission of Mariner VI, performed a flyby of Mars in August 1969 and collected additional ultraviolet spectra of the atmospheric emissions. The spectrometers on board Mariner VI and VII had a spectral range from 110 to 430 nm. Due to their flyby trajectories, both missions only managed to observe the upper atmosphere twice, once ahead of them, and once behind them, for a total of four observations. This drastically limited the amount of data collected, compared to more recent missions in orbit around Mars. The combined analysis of both Mariner VI and Mariner VII data lead to the discovery of additional bands and lines of emissions, as well as the first detection of neutral atomic carbon in the Martian atmosphere. The mean spectrum obtained from the four observations is given in Figure 2.0.1 [Barth et al., 1971].

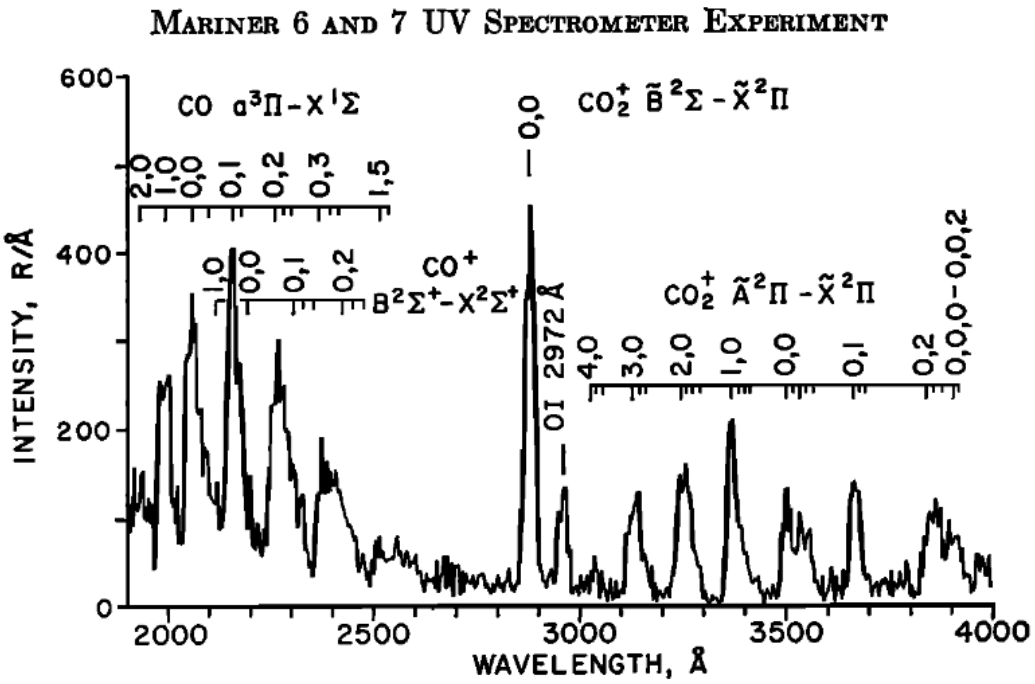


Figure 2.0.1: Spectrum of the upper Martian atmosphere from 1900 to 4000 Å with a 20 Å resolution. This spectrum was made by averaging the four observations made by Mariner VI and VII. Measurements were made tangentially at altitudes between 160 and 180 km [Barth et al., 1971].

The next two missions in the Mariner program attempted to place twin spacecrafts in orbit around Mars. Unfortunately, Mariner VIII crashed in the Atlantic Ocean a few minutes after its launch. On the other hand, Mariner IX became the first spacecraft to orbit a planet other than Earth and managed to accomplish all of its scientific objectives [Siddiqi, 2018]. Measurements of the Martian airglow with the on-board ultraviolet spectrometer were made from November 14, 1971 to October 27, 1972. The instrument had a spectral range going from 110 to 430 nm, simi-

larly to the ones on-board Mariner VI and VII [Barth et al., 1973]. The multitude of limb scans allowed the generation of the first limb intensity profile. A linear relation was observed between the intensity of the CO emissions in the Cameron bands (see Section 3.2) and the solar EUV flux, as well as a constant proportionality between the emissions of CO and $CO_2{}^+$ [Stewart et al., 1972].

The Soviet orbiters Mars 2 and 3 were equipped with photometers able to detect wavelengths from 105 to 134 nm. In 1971, Mars 3 observed the 121.6 nm hydrogen and 130 nm oxygen airglows. Following a computer failure, Mars 4 was not able to manoeuvre itself in orbit around Mars. Its successor, Mars 5 observed the airglow in the same frequencies as Mars 3. An unsuccessful attempt to observe the nightglow in the visible spectra was made in 1976 with Mars 5 with a visible spectrometer. The lack of detection set an upper limit of 50 R[1] on the 557.7 nm oxygen emission in the nightglow. [Krasnopolsky, 2013]

The ESA Mars Express (MEx) orbiter is equipped with the Spectroscopy for Investigation of Characteristics of the Atmosphere of Mars (SPICAM), a two-channel ultraviolet/infrared spectrometer. Its UV spectral range was from 118 to 320 nm [Bertaux et al., 2006], while its IR range was from 1000 to 1700 nm [Korablev et al., 2006]. SPICAM has been operating continuously since December 23, 2003, but the UV channel has been sending dark frames since December 2014. The collected data in the UV range therefore cover MY27 to MY30. SPICAM produced the first measurement of the seasonal evolution of the 1270 nm $O_2$ dayglow, a significant discovery as this emission results from the photolysis of the ozone, thus offering a proxy for the measurement of the ozone density. The nightglow 1270 nm emission, on the other hand, is the result of the recombination of atomic oxygen and can serve as a proxy for $O_2$ density on the night hemisphere [Montmessin et al., 2017]. The UV channel observed for the first time on Mars the $N_2$ Vegard-Kaplan bands in the dayglow. Measurements of the Cameron and UVD emissions have been compared to the ones made more than 30 years before by the Mariner missions, offering for the first time an insight on the long term variations of the airglow [Leblanc et al., 2006].

The NASA Mars Atmosphere and Volatile Evolution (MAVEN) orbiter is equipped with the Imaging Ultraviolet Spectrograph (IUVS), a spectrometer capable of observing airglow from 115 to 330 nm. IUVS has been collecting data since Fall 2014. It notably made the first imaging of the Martian nightglow, while observing the ultraviolet recombination emissions from nitric oxide [McClintock et al., 2015]. MAVEN is also equipped with the EUV Monitor, a noteworthy piece of equipment as it measures the solar irradiance of Mars in the EUV range. Data from this instrument serves in the study of the correlation between the UV irradiance and the intensity of the airglow [Soret et al., 2022]. We will be using EUVM data when reproducing this analysis in Section 6.

The Nadir and Occultation for Mars Discovery (NOMAD) is a spectrometer on board of the ongoing Trace Gas Orbiter (TGO) mission of the ESA and ROSCOSMOS. TGO has been orbiting Mars since 2016, and after a series of aerobraking manoeuvres to achieve its scientific orbit, has started its scientific mission in April 2018 [Willame et al., 2022]. One of the components of the NOMAD spectrometer is the Ultraviolet and Visible Spectrometer (NOMAD/UVIS), whose primary function is to perform solar occultations and observe backscattered ultraviolet solar radiations. [Soret et al., 2022] UVIS observable spectrum ranges from 200 to 650 nm, with a resolution ranging from 1.2 nm to 1.6 nm from short to long wavelengths. As this instrument offers the first possibility of observing Martian visible airglow since Mars 5 attempt in 1976, it led notably to the first observations of the three main UV and visible emissions of neutral atomic oxygen at 297.2, 557.7 and 630 nm [Gérard et al., 2020][Gérard et al., 2021][Soret et al., 2022]. The present study is mostly based on data from the UVIS instrument.

Since February 2021, the Emirates Mars Mission is orbiting Mars and observing the Martian atmosphere with its Emirates Mars Ultraviolet Spectrometer (EMUS). This instrument is capable of observing the Martian dayglow from 83 to 180 nm. The spacecraft has a high-altitude orbit with a 54.5-hour period, offering a near-permanent monitoring of a whole hemisphere. [Holsclaw et al., 2021]

In addition to orbital observation, the Martian airglow has been observed from orbit around Earth using telescopes, including the Hopkins Ultraviolet Telescope (e.g [Feldman et al., 2000]), the Extreme Ultraviolet Explorer (e.g.[Krasnopolsky and Gladstone, 1996]) and the Hubble Space

[1]The rayleigh is a unit of photon flux. 1 rayleigh = $4\pi \times 10^{10}$ photons cm$^{-2}$ s$^{-1}$ sr$^{-1}$.

Telescope (e.g. [Bhattacharyya et al., 2017]). The possibility of airglow observation by the James Webb Space Telescope has been suggested [Villanueva et al., 2015]. While those instruments offer the possibility of observing a full hemisphere of the planet at the same time, they lack the angular resolution needed to study spatial variation of the airglow, and their observations are constrained by the orbital disposition of Earth and Mars. They are therefore more adapted for the study of atmosphere component budgets, than the regional climate.

# 3. Emission frequencies

| Constituent | Abundance |
|---|---|
| $CO_2$ | 95.32% |
| $N_2$ | 2.7% |
| Ar | 1.6% |
| $O_2$ | 0.13% |
| CO | 0.07% |
| $H_2O$ | 0.03% (variable) |
| Ne | 2.5 ppm |
| Kr | 0.3 ppm |
| Xe | 0.08 ppm |
| $O_3$ | 0.04-0.2 ppm (variable) |

Table 3.0.1: Abundance of the main components of the lower Martian atmosphere. While $H_2O$ and $O_3$ are the most variable components, other variations of the composition may occur. Notable processes inducing variation include the $CO_2$ cycle and the atmospheric photochemical processes [Haberle, 2015].

The Martian lower atmosphere is composed mostly of $CO_2$, $N_2$, Ar, $O_2$ and CO. Table 3.0.1 shows the volume mixing ratio of those components. The mean surface atmospheric pressure is about 6.1 hPa, but this value can vary vastly through seasonal variations. Indeed, $CO_2$ forms polar caps in winter as it deposits on the surface, then sublimates back to the atmosphere in spring. The combined effect of both polar caps produce a transfer of about 25% of the atmosphere from one cap to the other. [Haberle, 2015]

At higher altitudes, many photochemical processes alter the atmospheric composition, hence creating unstable components in the upper atmosphere, including O I, C I and OH, but also ions such as $O_2^+$, $CO^+$ and $CO_2^+$. [Haberle et al., 2017]

The brightest emission in the visible Martian dayglow is by far the neutral atomic oxygen, while the UV part of the Martian dayglow is mainly emitted by a combination of O, CO, $CO_2^+$, H, $N_2$, N, and C, in order of total contribution to the brightness. Figure 3.0.1 shows the atmospheric conditions at the perihelion of MY35.

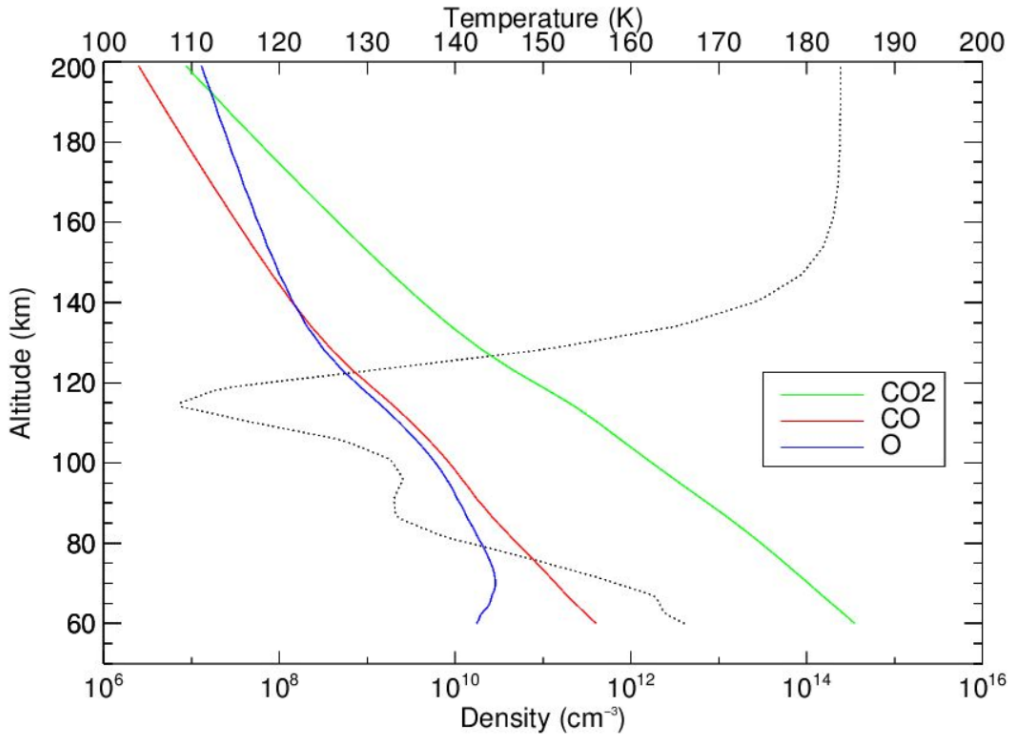


Figure 3.0.1: Number density profiles of the $CO_2$ (green), CO (red) and O (blue) in the upper atmosphere, given in $cm^{-3}$. The black line shows the temperature profile, given in K. Data are taken from the MCD in a simulation of the MY35 at solar noon for Ls = 71° and coordinates (0°, 0°).

Figure 3.0.2 shows the spectrum we obtained by averaging all the NOMAD UVIS spectra between 115 km and 125 km. This range of altitude have been specifically chosen for its variety of frequencies present in the airglow. This work will focus exclusively on the Martian dayglow emissions of neutral atomic oxygen and of the carbonic oxides.

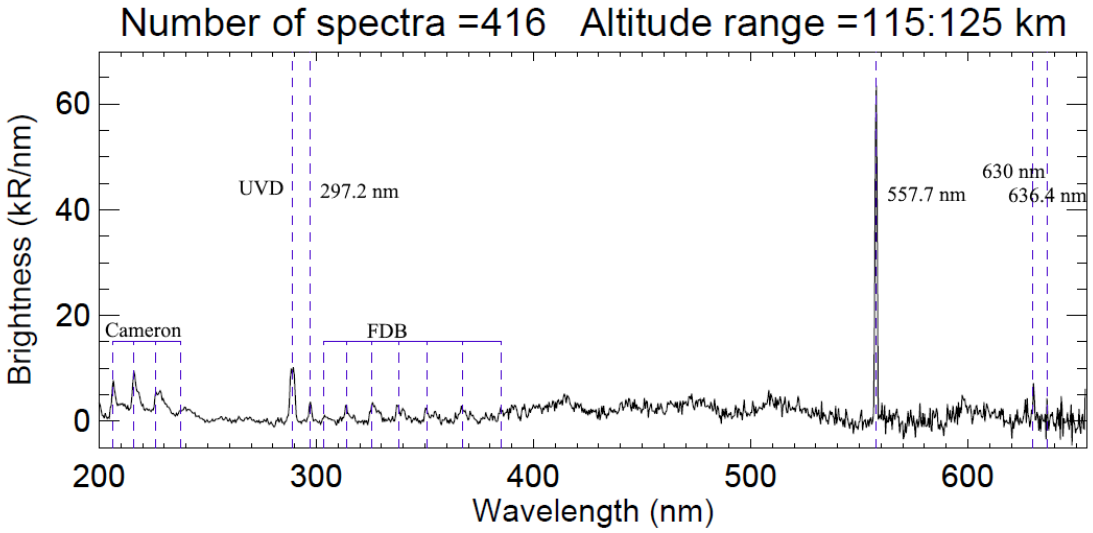


Figure 3.0.2: Mean spectrum obtained from 416 spectra observed between 115 and 125 km altitude. The dashed grey lines correspond from left to right to the (0,0), (0,1), (0,2) and (0,3) emission lines of the CO Cameron bands, the $CO_2^+$ UV doublet at 288 and 289 nm, the O I UV line at 297.2 nm, the (4,0), (3,0), (2,0), (1,0), (0,0), (0,1) and (0,2) emission lines of the $CO_2^+$ FDB, the O I green line at 557.7 nm and the O I red doublet at 630 and 636.4 nm.

## 3.1 Neutral atomic oxygen emission lines

The most noticeable emission line in Mars atmosphere is by far the 557.7 nm green line, produced by a transition of neutral atomic oxygen from the O($^1$S) to O($^1$D). The transitions of the O($^1$S) state are shown on Figure 3.1.1. On Earth, this emission is the source of the polar aurora green colour and of the green atmospheric dayglow. It was first discovered on Mars by Gérard et al. in 2020, using data from UVIS. This was the first observation of a dayglow on Mars in the visible spectrum. Two peaks in the limb intensity profiles were observed : one around 77 km altitude mainly due to the photodissociation of $CO_2$ by solar Lyman $\alpha$ and another one near 130 km altitude mainly due to extreme ultraviolet radiation [Gérard et al., 2020]. Figure 3.1.2 shows the limb profile of the 557.7 nm airglow observed by Gérard et al.

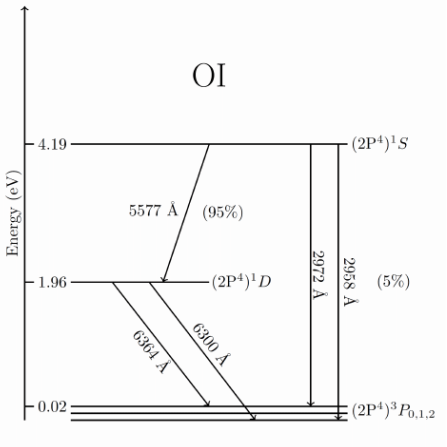


Figure 3.1.1: Energy level diagram of atomic oxygen for the transitions from $^1S$ and $^1D$ states. From Bhardwaj and Susaria, 2012.

A follow-up study by Soret et al.(2022) identified the same two peaks, but slightly higher and more intense, using a larger sample of data from UVIS. This is expected, as the original database covers a period where Mars was closer to its aphelion. Soret et al. hence identified a seasonal increase of the peak altitude and intensity as Mars approaches its perihelion [Soret et al., 2022]. The main source of O($^1$S) in the Martian atmosphere has been identified as the photodissociation of $CO_2$ by EUV light. The altitude of the lowest peak of the 557.7 nm line seems to be primarily influenced by the $CO_2$ density. The airglow emission of the O($^1$S) state have therefore been identified as possible proxy for the density variations of the $CO_2$ [Gkouvelis et al., 2018][Soret et al., 2022].

The 630 nm and 636.4 nm red emission lines are both produced by the transition from the excited state O($^1$D) to the ground triplet state O($^3$P). They were first identified in the Martian atmospheric dayglow, respectively, by Gérard et al. in 2021 [Gérard et al., 2021] and Soret et al. in 2022 [Soret et al., 2022]. In the same study, Soret et al. measured a ratio between the two emissions $R = I(630nm)/I(636.4nm)$ with a value of $R = 2.997$ in agreement with the theoretical value ranging from 2.997 to 3.10. They also measured a peak intensity of 5.3 kR, located at 137.5 km.

The 297.2 nm UV emissions are produced by the O($^1$S) upper state, which also produces the 557.7 nm green emission. The theoretical ratio between the 557.7 nm green line and 297.2 nm UV line, $R = I(557.7nm)/I(297.2nm)$ is, according to NIST, $R = 16.7$. Gérard et al. found a ratio of $16.5 \pm 0.4$ from observing the Martian dayglow in agreement with the theoretical value [Gérard et al., 2020]. Soret et al. in 2023, measured this ratio at $R = 15.8 \pm 2.4$ using a wider sample of data from UVIS [Soret et al., 2023].

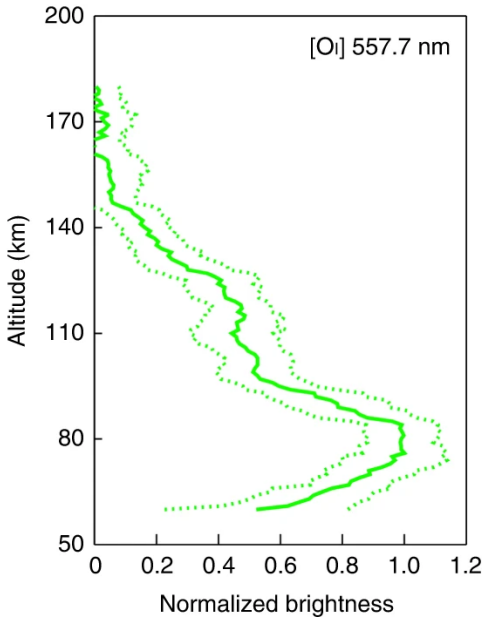


Figure 3.1.2: Limb profile of the 557.7 nm dayglow observed by Gérard et al., 2020, made from averaging measurements from 16 UVIS limb scans with a binning of 5 km. Brightness has been normalised by its peak value. Doted lines indicate a variability of $1\sigma$ [Gérard et al., 2020].

## 3.2 Carbon oxides emission bands

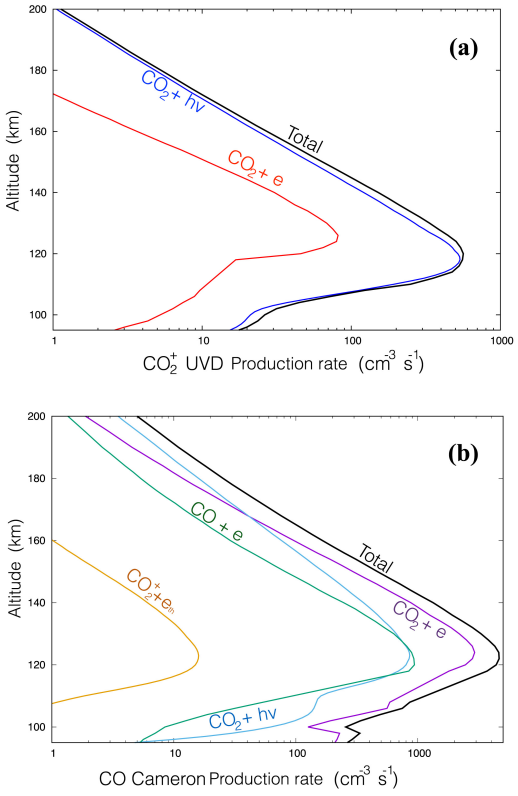


Figure 3.2.1: Evaluation of the production rate of $CO_2^+$ UVD (a) and CO Cameron emissions (b) associated to the different production processes in the Martian atmosphere via a photochemistry model [Gérard et al., 2019].

Atmospheric CO has two main contributions to the airglow spectrum; the Cameron bands and the fourth-positive group bands. The Cameron bands range from 180 to 280 nm and are produced by a transition from CO($a^3\Pi$) to CO($X^1\Sigma^+$) [Lee et al., 2022].

The formation of CO($a^3\Pi$) is possible through four different processes, an excitation by electron impact of a CO molecule (1), an electrodissociation of $CO_2$ (2), a photodissociation of $CO_2$ (3) or the dissociative recombination of $CO_2{}^+$ (4) [Stiepen et al., 2015].

1. $CO + e \longrightarrow CO(a^3\Pi) + e$
2. $CO_2 + e \longrightarrow CO(a^3\Pi) + O^* + e$
3. $CO_2 + h\nu \longrightarrow CO(a^3\Pi) + O^*$
4. $CO_2{}^+ + e \longrightarrow CO(a^3\Pi) + O^*$

Cameron airglow has been measured in the Martian atmosphere with a peak intensity of 175kR at an altitude of 122.5 km [Soret et al., 2023]. At the peak altitude, the main processes generating CO($a^3\Pi$) in the Martian atmosphere are the photoelectron impacts with $CO_2$ (E>11.5 eV) and, an order of magnitude lower, the photodissociation of $CO_2$ by EUV photons ($\lambda$<108 nm) and electron collisions with CO (E>6 eV). Estimation of the production rate of CO($a^3\Pi$) by a photochemical model

are given in Figure 3.2.1 (b) [Gérard et al., 2019].

The fourth-positive group (4PG) bands range from 111 to 280 nm and result from a transition from $CO(A^1\Pi)$ to $CO(X^1\Sigma_1^+)$ [Lee et al., 2022]. These emission bands were previously observed in the Martian airglow in the Mariner 6 and 7 data, but only below 180 nm [Gérard, 1982]. The 200 nm to 280 nm part of the UVIS spectra are dominated by the Cameron bands, thus it has not yet been detected in UVIS data.

Carbon dioxide produces emissions in the airglow, but only when ionized. The brightest ones are the Fox-Duffendack-Barker (FDB) bands and the UV doublet (UVD) emissions. The FDB bands result from the transition from the $CO_2^+(A^2\Pi_g)$ to the $CO_2^+(X^2\Pi_g)$ states [Barth et al., 1971] [Soret et al., 2023]. The $CO_2^+(A^2\Pi_g)$ energy state results from photoionisation of $CO_2$ (1), electro-ionization of $CO_2$ and fluorescent scattering of sunlight by ${CO_2}^+$ (3).

1. $CO_2 + h\nu \longrightarrow {CO_2}^+(A^2\Pi_g) + e$
2. $CO_2 + e \longrightarrow {CO_2}^+(A^2\Pi_g) + 2\,e$
3. ${CO_2}^+ + h\nu \longrightarrow {CO_2}^+(A^2\Pi_g) \longrightarrow {CO_2}^+(X^2\Pi_g)$

The latter is the dominant source above 160 km [Fox and Dalgarno, 1979].

The UV doublet (288.3-289.6 nm) is the result of a transition from $CO_2^+(B^2\Sigma)$ to $CO_2^+(X^2\Pi)$. The main processes of formation of $CO_2^+(B^2\Sigma)$ in the Martian atmosphere are the photoionization of $CO_2$ by EUV ($\lambda < 69$ nm) (1), and in an order of magnitude lower by photoelectron impacts (E>18.1 eV) (2).

1. $CO_2 + h\nu \longrightarrow {CO_2}^+(B^2\Sigma) + e$
2. $CO_2 + e \longrightarrow {CO_2}^+(B^2\Sigma) + 2\,e$

Estimation of the production rate of $CO(a^3\Pi)$ by a photochemical model are given in Figure 3.2.1 (a) [Gérard et al., 2019].

Both emissions of $CO_2^+$ peak at 122.5 km. The FDB emission reached 75 kR, while the UVD emission reached 25 kR. Constant ratios between the Cameron, the UVD and the FDB emissions have been deduced from limb observations. Estimations of their values based on UVIS data are the following [Soret et al., 2023] :

$$I(Cam)/I(UVD) = 6.9, \qquad I(Cam)/I(FDB) = 2.3, \qquad I(FDB)/I(UVD) = 3.0.$$

# 4. Sampled data and statistics

UVIS usually acquires 1024-bin spectra, but during periods of low transmission rates a horizontal binning mode can be applied to reduce the data volume. This process consist in a binning by 4 of the measured spectrum, reducing the definition from 1024 to 256 bins. While this data have been used indiscriminatly from the 1024-bin data in previous study [Soret et al., 2022], we decided to set them aside because of their high uncertainty. They will nonetheless be presented in some section to facilitate the comparison with previous works.

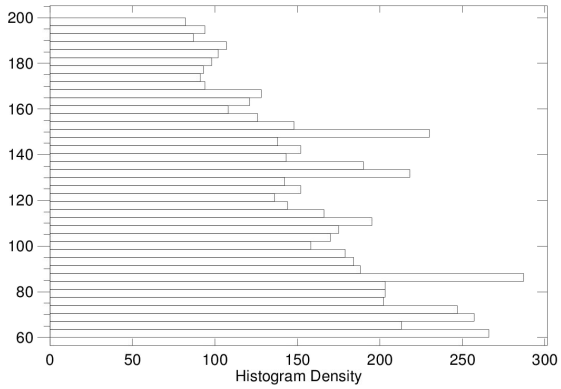


Figure 4.0.1: Altitude distribution of the 6417 spectra selected, with a binning of 3.5 km.

This work uses data collected from May 29, 2019 (MY 35, Ls 31.92°) to February 18, 2023 (MY 37, Ls 25.88°). During that interval, 35545 spectra were observed by UVIS. Among those, low altitude observations have to be rejected as their emissions would primarily originate from the scattering of sunlight in the atmosphere. Similarly, high altitude observations have to be rejected to avoid contamination from the sky background. A constraint on the solar zenithal angle (SZA) is needed in order to select exclusively the airglow emissions. Hence, the observations have been filtered to keep only those at an altitude between 60 and 200 km and a solar zenithal angle between 0 and 70°. We only used data with a 1024 spectral binning. A total of 6417 spectra were kept for this study. As Figure 4.0.1 shows, the whole range of altitude is correctly covered by our data.

This set of data was subdivided into eight subsets of data, corresponding to four quadrants over two Martian revolutions. The quadrants are defined based on the aphelion (Ls = 71°) and perihelion (Ls = 251°) to reflect four orbital seasons. The Martian orbital calendar is given on Figure 1.0.2. The precise values of Martian solar longitude associated to these quadrants are given in Table 4.0.1. Note that by definition, quadrants Q1 and Q5 are centred around the aphelion, while the quadrants Q3 and Q7 are centred around the perihelion.

| Quadrant | Ls range | Nb. of spectra | Orbital quadrant | Ls range | Nb. of spectra |
|---|---|---|---|---|---|
| Q1 | 26° (MY35) - 116° (MY35) | 262 | Q5 | 26° (MY36) - 116°(MY36) | 1483 |
| Q2 | 116° (MY35) - 206° (MY35) | 275 | Q6 | 116° (MY36) - 206° (MY36) | 936 |
| Q3 | 206° (MY35) - 296° (MY35) | 592 | Q7 | 206° (MY36) - 296° (MY36) | 1009 |
| Q4 | 296° (MY35) - 26° (MY36) | 1115 | Q8 | 296° (MY36) - 26° (MY37) | 745 |
| Revolution 1 | 26° (MY35) - 26° (MY36) | 2244 | Revolution 2 | 26° (MY36) - 26° (MY37) | 4173 |

Table 4.0.1: Solar longitude ranges associated to the different orbital quadrants and revolutions, as well as the number of corresponding spectra in each dataset.

Histograms of the repartition of the altitude for the different quadrants are given in Figure 4.0.2. All quadrants have a good coverage of the altitude range of this study, except for Q2 which lacks observations under 80 km, and Q3 which as only a few values under 80 km. This should be considered while analysing limb profiles at those altitudes, as some of them are incomplete. As the altitude bins with the lower counts have the largest error margin on their intensity, we can identify that the less reliable results will be associated to Q1, Q2 above 100 km and Q3 under 90 km.

For the purpose of analysing the annual variations, we will use a revolution period starting and ending at Ls = 26°, rather than using Martian years. The two revolutions studied therefore correspond to the two columns in Table 4.0.1. This choice is motivated by the time period covered in our dataset and by the possibility of an easy comparison with the seasonal quadrants. Both revolutions will be referred thereafter as Revolutions 1 and 2, or simply R1 and R2.

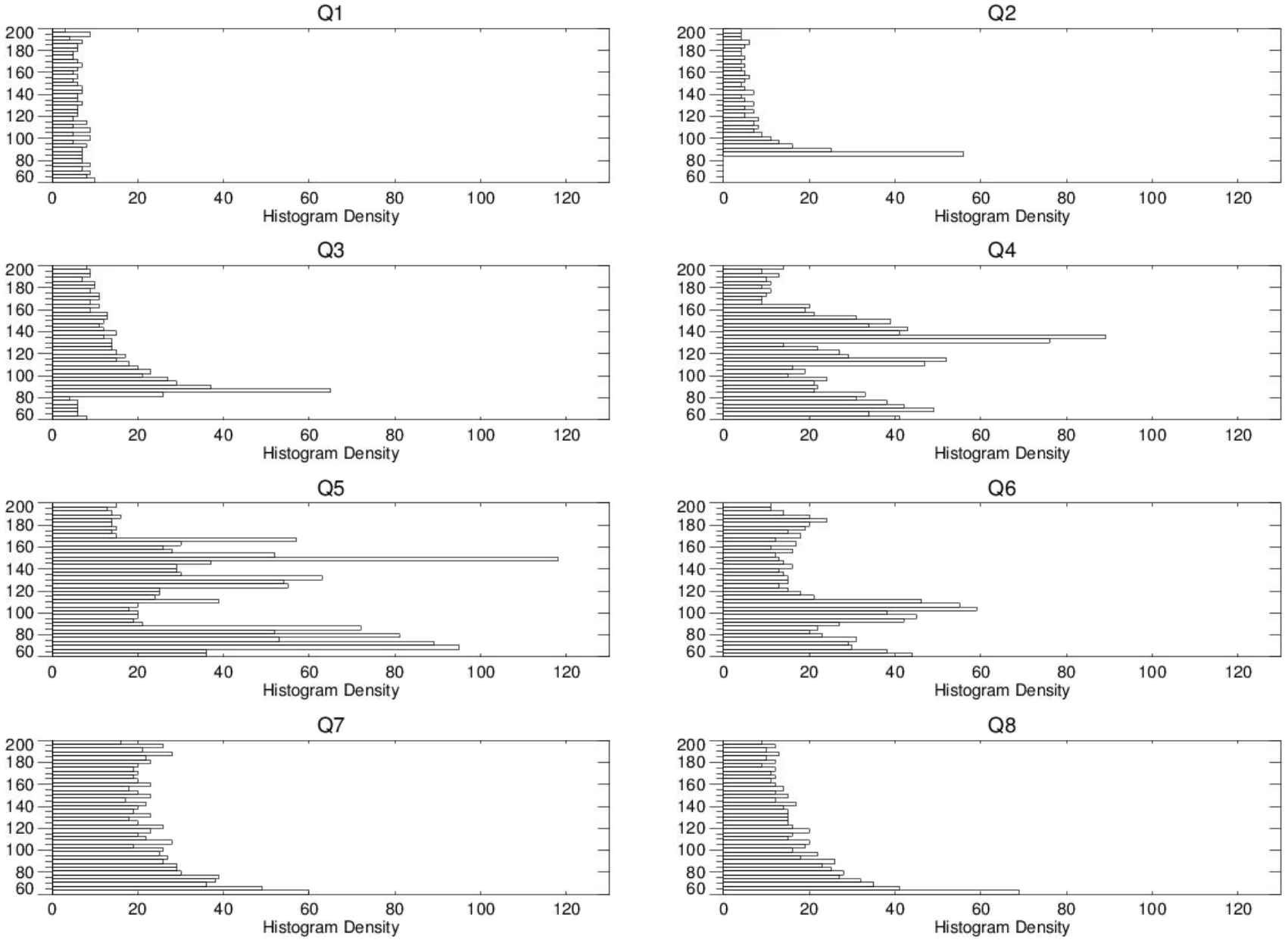


Figure 4.0.2: Altitude distribution of the 6417 selected spectra distributed in quadrants with a binning of 3.5 km.

# 5. Limb profiles

A limb profile is a plot of the brightness at a given frequency as a function of the altitude. It is a great visualisation of the average state of an air column and can provide a lot of information on the composition of an atmospheric layer and the processes occurring inside it.

The construction of those plots were made using the 6802 spectra dataset with the following method :

- First, we filtered the spectra corresponding to the range of Ls we want to study.
- Then, we subdivided the spectra in 3.5 km bin from 60 to 200 km, for a total of 39 bins.
- For every bin, we created an average spectrum of the airglow during this period in this range of altitude.
- We identified the intensity of the spectrum in the wavelengths of interest, as well as the error margins on those values.
- We plotted the resulting intensity as a function of the altitude.

## 5.1 557.7 nm limb profiles

A mean limb profile for the green line was made for both revolutions, and for all eight quadrants. The two revolution profiles are shown on Figure 5.1.1, in black for R1 and in green for R2. The profile for the second revolution is, with only two small exceptions, always more intense than the first profile. The limb profile for Revolution 1 shows a peak of 129.0 ± 3.3 kR at an altitude of 86.25 km. The upper peak has an altitude of 124.75 km and an intensity of 55.6 ± 1.9 kR. The limb profile for Revolution 2 shows a lower peak of 144.2 ± 2.5 kR at 89.75 km. Concerning the upper peak, R2 profile shows two different upper peaks, one of 75.6 ± 2.2 kR at 117.75 km and a second of 52.6 ± 2.2 kR at 135.25 km. This double peak shape does not appear in any seasonal plot. The 117.75 km peak is link to Q5 and Q8, which also have their upper peaks at this altitude. The origin of the 135.25 km peak is less clear, as both Q6 and Q7 have their upper peaks under this altitude.

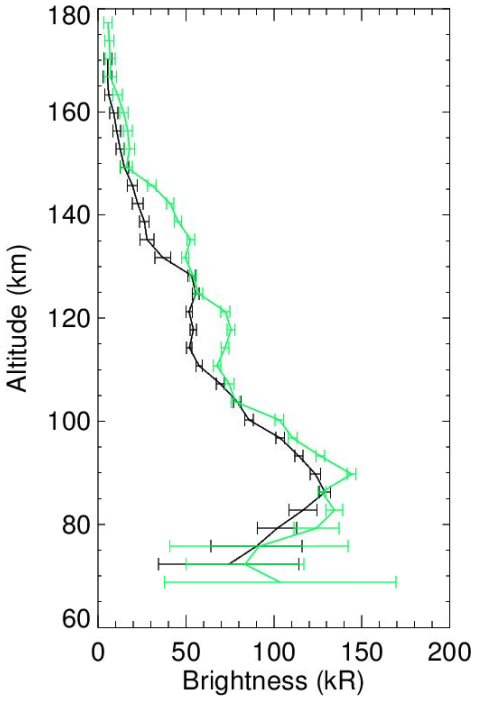


Figure 5.1.1: Average limb profiles for the 557.7 nm oxygen green line for Revolution 1 (black line) and Revolution 2 (green line) as defined in Table 4.0.1. Intensities have been gathered in bins of 3.5 km in altitude.

A similar analysis of the seasonal profiles can be made. Figure 5.1.2 shows the average limb profiles for each quadrant. Q1 and Q5 show profiles of similar intensity above 90 km. Q1 has a lower peak more intense than Q5, with a respective peak intensity of 123.8 ± 4.8 kR at 75.75 km and of 107.4 ± 2.5 kR at 82.75 km. While Q1 presents a slight upper peak of 57.5 ± 4.3 kR at 114.25 km, Q5 shows a well-defined peak of 58.0 ± 2.4 kR at 117.75 km. Q1 shows similar values of intensity at the same altitude. The average ratio of the intensity of Q5 to Q1 is 0.95.

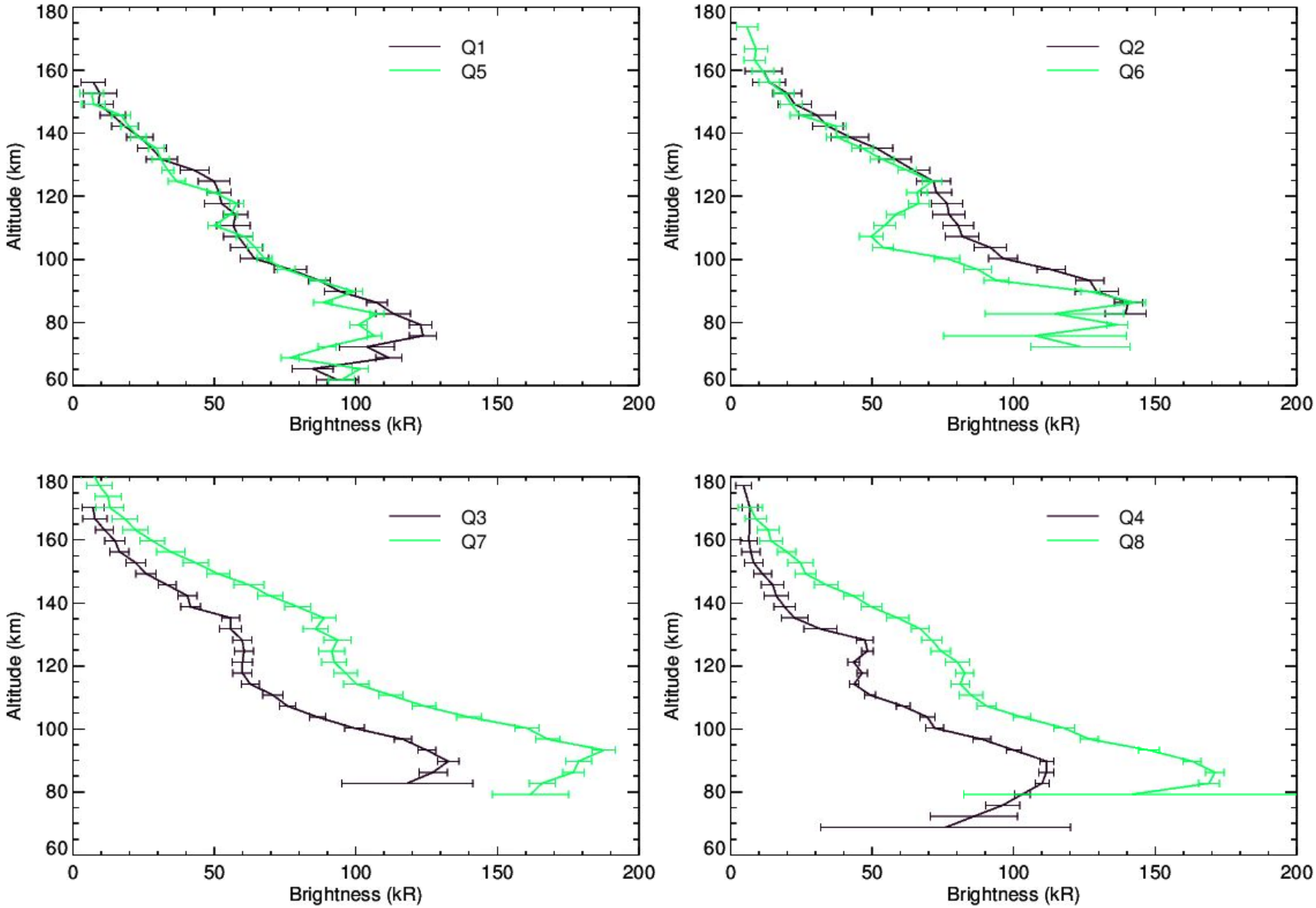


Figure 5.1.2: Average limb profiles of the 557.7 nm emission for the different quadrants. Each subplot represents a different solar longitude range: 26°-116° (Q1-Q5), 116°-206° (Q2-Q6), 206°-296° (Q3-Q7) and 296°-26° (Q4-Q8).

The Q2 limb profile is very smooth in contrast to the sharp double peaks of that of Q6. Q2 profile is always either larger or about the same value as Q6 profile. Q2 profile shows a lower peak of 140.5 ± 5.0 kR at 86.25 km. Above that, the profile shows a monotonic decrease with altitude. Q6 lower peak has an intensity of 142.8 ± 3.7 kR at 86.25 km; while its upper peak reaches an intensity of 71.25 ± 3.4 kR at 124.75 km. The average ratio of the intensity of Q6 to Q2 is 0.87.

Both Q3 and Q7 have profiles of similar shapes, but of drastically different intensity. Q3 profile has a lower peak with an intensity of 132.7 ± 3.8 kR at 89.75 km, while Q7 profile has a lower peak with an intensity of 187.6 ± 4.1 kR at 93.25 km. Q3 and Q7 profiles show upper peaks respectively of 59.9 ± 3.3 kR and of 93.6 ± 4.8 kR at 128.25 km. The average ratio between the intensities for Q7 and Q3 is 1.69.

A similar situation can be observed for Q4 and Q8 profiles. Q4 profile has an upper peak at 111.7 ± 2.5 kR at 89.75 km, and a second smaller one at 48.4 ± 2.1 kR at 124.75 km. Q8 profile only has a lower peak at 171.1 ± 3.3 kR at 86.25 km, and an upper peak of 82.7 ± 3.2 kR at 117.75 km. The average ratio between the intensity for Q8 and Q4 is 1.89.

As could be expected, the altitude of the peak is lower during Q1 and Q5, corresponding to the aphelion, than during Q3 and Q7, corresponding to the perihelion. Section 6 will discuss in details the mechanism responsible for those variations.

## 5.2 297.2 nm limb profiles

The limb profiles of the 297.2 nm airglow for the two revolutions are given in Figure 5.2.1. The 297.2 nm airglow is emitted by the same energy level of the neutral atomic oxygen as the 557.7 nm. As expected, we can see that both profiles have the same shape. The R1 profile has a peak intensity of 6.3 ± 1.2 kR at 93.25 km, while the R2 profile has a peak intensity of 9.16 ± 0.97 kR at 89.75 km.

Concerning the seasonal limb profiles, they are given in Figure 5.2.2. The profile for Q1 has a maximum of 7.1 ± 1.1 kR at 79.25 km high, while the profile for Q5 has a maximum of 6.61 ± 0.99 kR at 82.75 km. The ratio of the brightness between Q5 and Q1 is 1.07.

The Q2 profile never reaches its maximum before reaching the lower limit of the observation, but if we assume there exists a peak below, it must be brighter than 8.7. Meanwhile, the Q6 profile as a maximum of 8.5 ± 1.1 kR at 89.75 km. The ratio between Q6 and Q2 is 0.83.

The Q3 profile has a maximum of 6.95 ± 0.84 kR at 96.75 km, the profile for Q7 has a maximum of 11.3 ± 1.7 kR at 89.75 km. The ratio between Q7 and Q3 is 1.59.

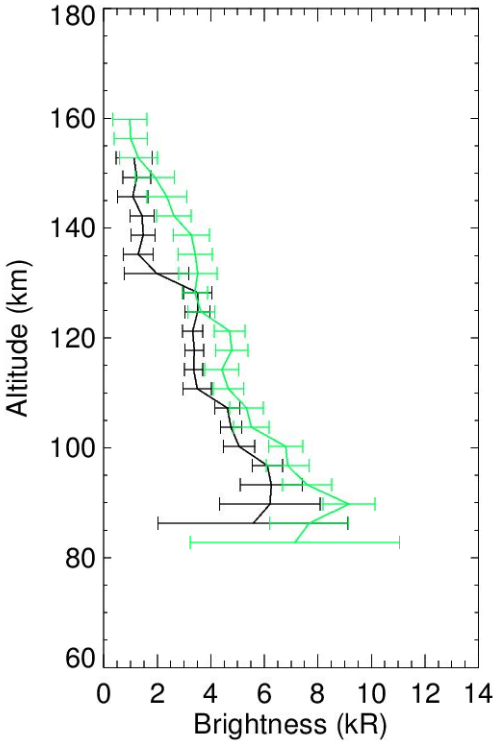


Figure 5.2.1: Average limb profiles for the 297.2 nm oxygen line for Revolution 1 (black line) and Revolution 2 (green line) as defined in Table 4.0.1. Intensities have been gathered in bins of 3.5 km in altitude.

The Q4 profile has a maximum of 6.8 ± 1.0 kR at 86.25 km, the profile for Q8 has a maximum of 10.61 ± 0.94 kR at 86.25 km. The ratio between Q8 and Q4 is 1.79.

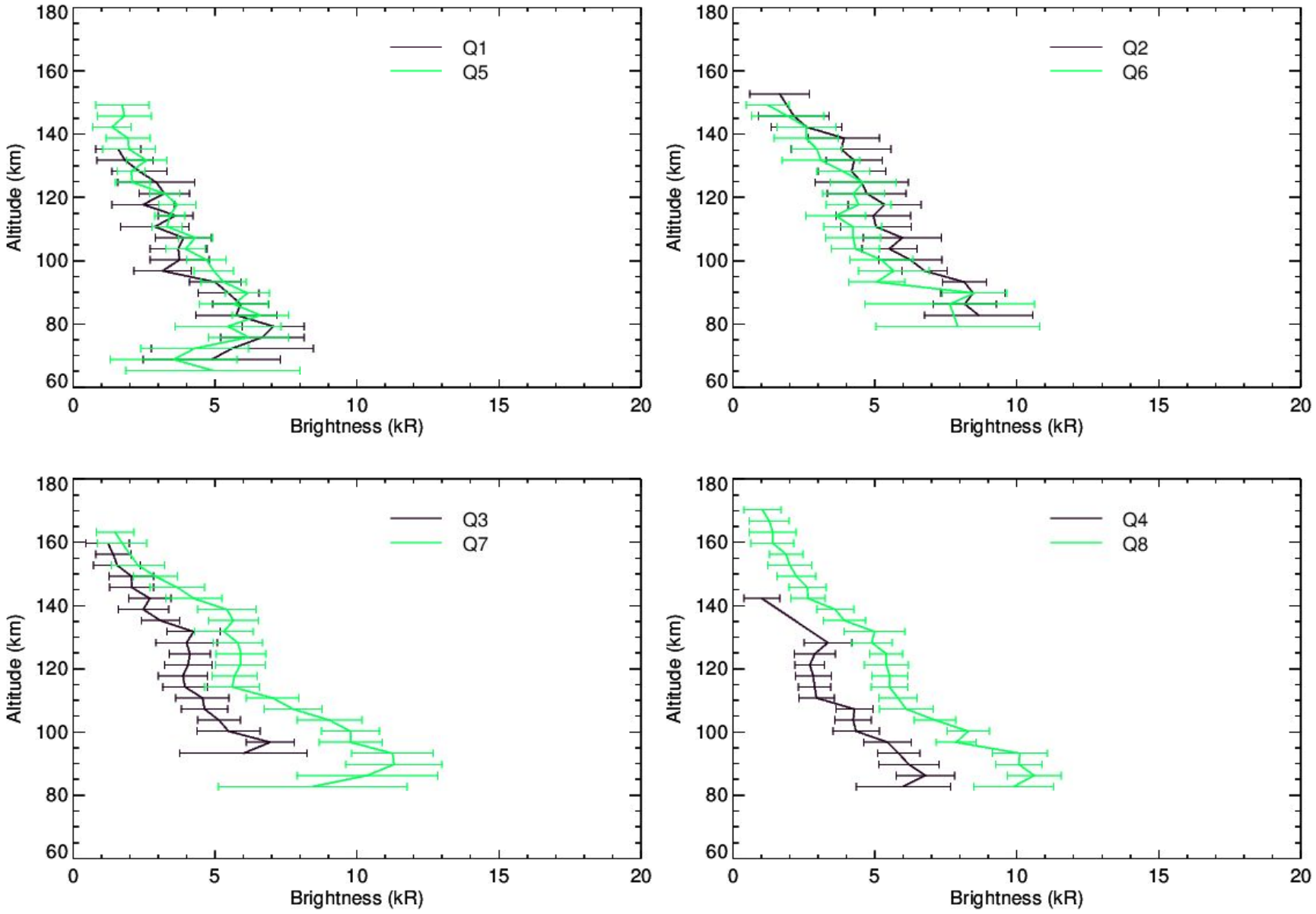


Figure 5.2.2: Average limb profiles of the 297.2 nm emission for the different quadrants. Each subplot represents a different solar longitude range: 26°-116° (Q1-Q5), 116°-206° (Q2-Q6), 206°-296° (Q3-Q7) and 296°-26° (Q4-Q8).

## 5.3 630 nm limb profiles

The 630 nm red emission line was observed during both Revolution 1 and 2. Unfortunately, the low intensity of this emission did not allow for an analysis of the seasonal variation. The limb profiles of the 630 nm airglow for the two revolutions are given in Figure 5.3.1. Second degree polynomial fits of the brightness are also given in order to approximate the peak altitude and intensity. As we can clearly see on the figure, the error margins are larger than the variations. We should therefore be cautious when analysing the data point by point and rather focus on the general trends.

The R1 profile shows a peak intensity of 6.8 ± 3.9 kR at an altitude of 166.75 km, but its associated quadratic approximation has a maximum of 6.30 ± 0.63 kR at an altitude of 149.25 km. The R2 profile shows a peak of intensity of 6.8 ± 2.6 kR at an altitude of 128.25 km, but its associated quadratic approximation has a maximum of 6.11 ± 0.61 kR at an altitude of 128.25 km. The average ratio between the R2 profile and the R1 profile is 1.10.

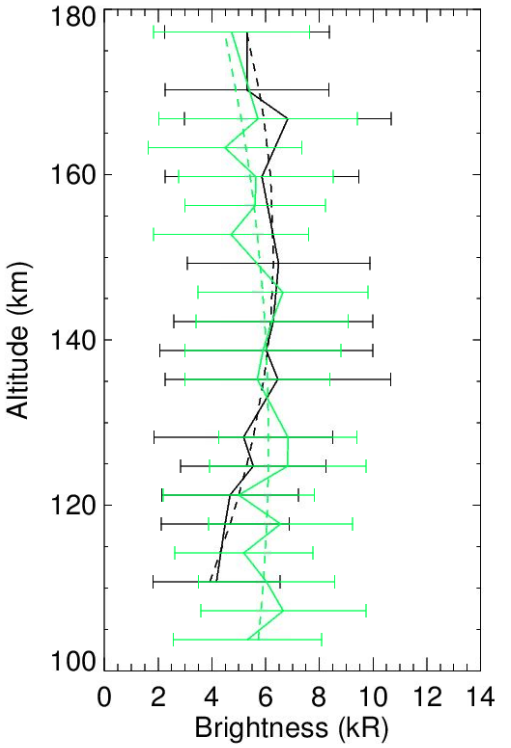


Figure 5.3.1: Average limb profiles for the 630 nm oxygen line for Revolution 1 (black line) and Revolution 2 (green line) as defined in Table 4.0.1. The dashed lines are the best second degree polynomial fit. Intensities have been gathered in bins of 3.5 km in altitude.

## 5.4 UVD limb profiles

The typical limb profile at the UVD frequency is a broad peak around 130 km. The intensity tends to drastically increase under 90 km, but this brightness is due to scattering rather than an airglow itself. We will therefore not discuss this part of the plots.
The limb profile for the UVD emissions of R1 shows a maximum of intensity of 22.4 ± 1.8 kR at 128.25 km, while the one of R2 shows a maximum of intensity of 30.5 ± 2.3 kR at 121.25 km. The ratio of the brightness for R2 to R1 above 90 km is 1.47. Both limb profiles are given in Figure 5.4.1.

The seasonal limb profiles are given in Figure 5.4.2. The profile for Q1 has a maximum of 19.6 ± 3.6 kR at 114.25 km high, while the profile for Q5 has a maximum of 23.6 ± 2.2 kR at 117.75 km. The ratio of the brightness between Q5 and Q1 above 90 km is 1.10.

The Q2 profile has a maximum of 28.6 ± 3.9 kR at 124.75 km, while the Q6 profile has a maximum of 32.2 ± 2.5 kR at 124.75 km. The ratio between Q6 and Q2 above 90 km is 1.05.

The Q3 profile has a maximum of 25.5 ± 3.4 kR at 128.25 km, while the Q7 profile has a maximum of 43.0 ± 3.7 kR at 128.25 km. The ratio between Q7 and Q3 above 90 km is 1.86.

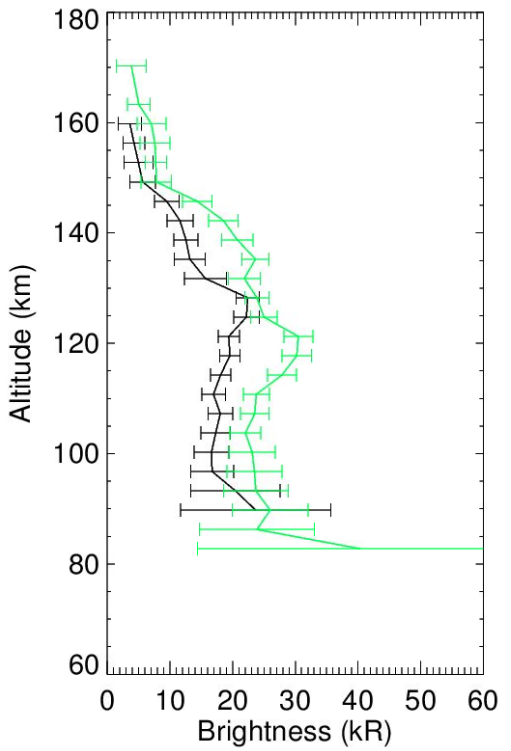


Figure 5.4.1: Average limb profiles for the UVD for Revolution 1 (black line) and Revolution 2 (green line) as defined in Table 4.0.1. Intensity have been gathered in bins of 3.5 km in altitude.

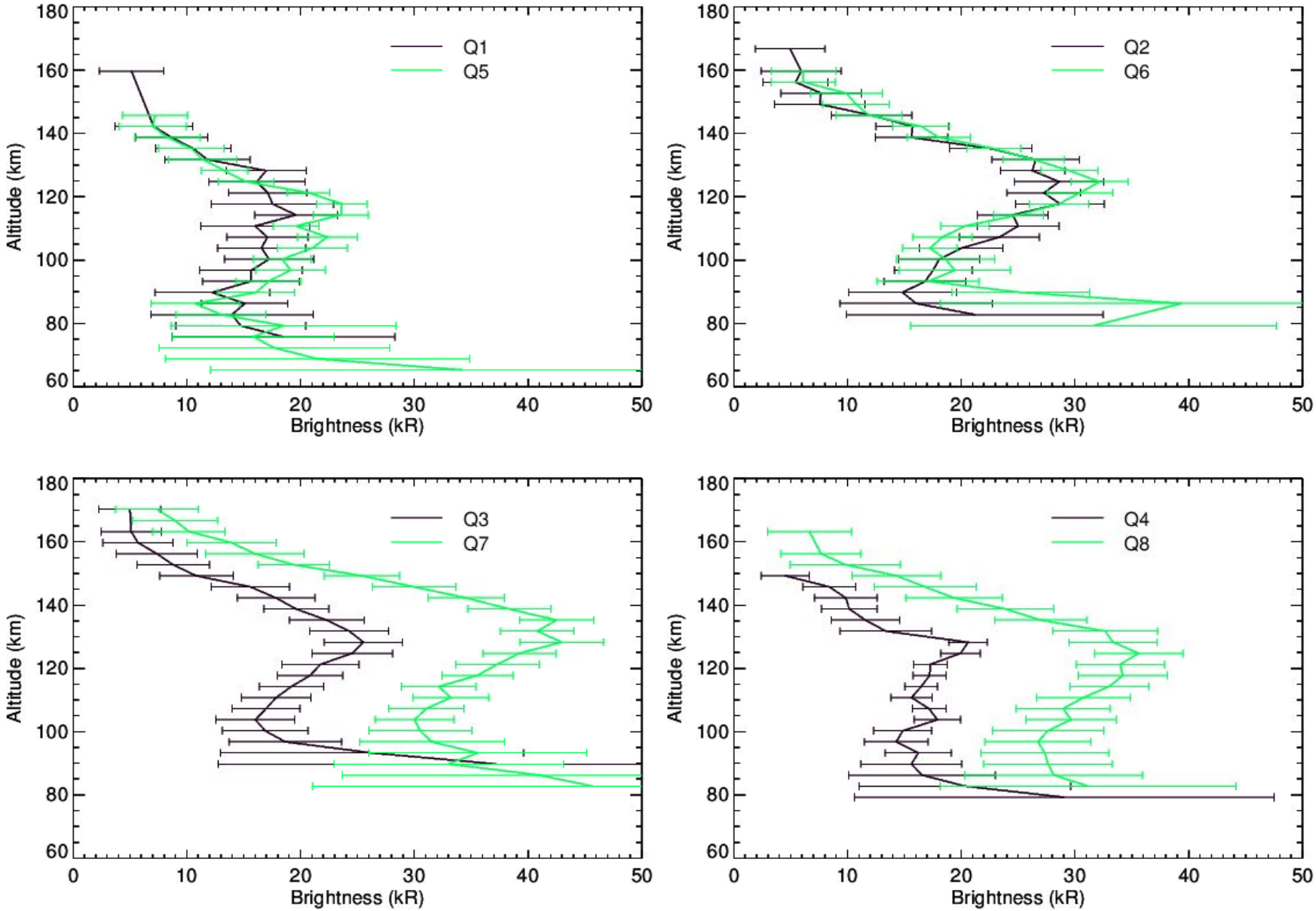


Figure 5.4.2: Average limb profiles of the UVD emission for the different quadrants. Each subplot represents a different solar longitude range: 26°-116° (Q1-Q5), 116°-206° (Q2-Q6), 206°-296° (Q3-Q7) and 296°-26° (Q4-Q8).

The Q4 profile has a maximum of 20.6 ± 1.7 kR at 128.25 km, while the Q8 profile has a maximum of 35.6 ± 3.9 kR at 124.75 km. The ratio between Q8 and Q4 above 90 km is 2.02.

The general trend is similar to the one of the green line. We observe lower peak altitudes and weaker intensities near aphelion, and higher peak altitudes and stronger intensities near perihelion.

## 5.5 Cameron limb profiles

The R1 profile shows a peak of 161 ± 35 kR at an altitude 128.25 km, while the R2 profile shows a peak of 174 ± 41 kR at an altitude of 121.25 km. Both profiles are given on Figure 5.5.1. It is important to note, that the variations are lower than the error margins associated to the observations. Cameron bands emission limb profiles are very similar in shape and altitude as the UVD profile. This phenomenon is expected as the reactions leading to the formation of both excited state of CO and $CO_2^+$ are primarily controlled by the same mechanisms, namely the density of $CO_2$ and of photoelectrons [Cox et al., 2010].

The seasonal profiles are presented in Figure 5.6.1. Once again, the variations observed are lower than the error margins associated to our observations. While we can have some degree of confidence in the general trends, point by point values should be taken cautiously.

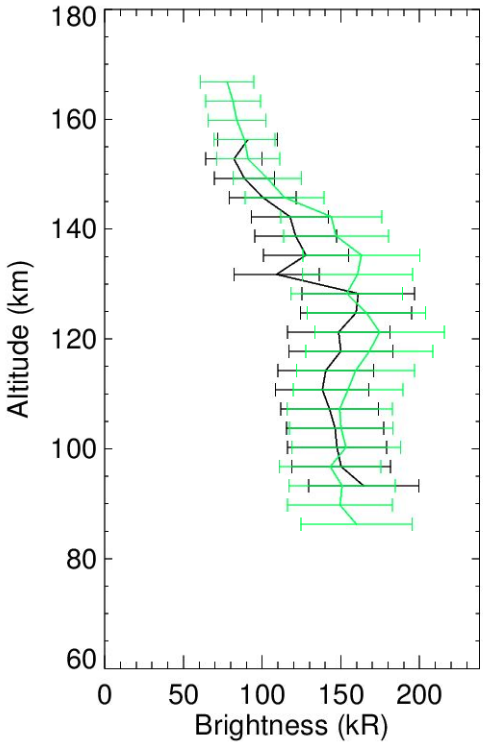


Figure 5.5.1: Average limb profiles for the Cameron band for Revolution 1 (full line) and Revolution 2 (dotted line) as defined in Table 4.0.1. Intensities have been gathered in bins of 3.5 km in altitude.

The Q1 profile has a peak of 166 ± 36 kR at 124.75 km, while the Q5 profile has a peak of 167 ± 36 kR at 121.25 km. The mean ratio between Q5 and Q1 is 1.18.

The Q2 profile has a peak of 233 ± 52 kR at 124.75 km, while the Q6 profile has a peak of 192 ± 47 kR at 124.75 km. The mean ratio between Q6 and Q2 is 0.80.

The Q3 profile has a peak of 195 ± 43 kR at 128.25 km, while the Q7 profile has a peak of 235 ± 57 kR at 135.25 km. The mean ratio between Q7 and Q3 is 1.14.

The Q4 profile has a peak of 129 ± 28 kR at 117.75 km, while the Q8 profile has a peak of 160 ± 42 kR at 124.75 km. The mean ratio between Q8 and Q4 is 1.21.

## 5.6 FDB limb profiles

The FDB profiles suffer from the same problem as the 630 nm ones. The lack of data makes an inter-seasonal analysis impossible, thus we had to limit this study to an inter-annual analysis. Figure 5.6.2 shows the average limb profiles for both R1 and R2. Once again, second degree polynomial fits were made in order to approximate the peak brightness and altitudes. The R1 profile has a maximum of 83.0 ± 7.8 kR at an altitude of 128.25 km, but its quadratic approximation shows a maximum of intensity of 76 ± 18 kR at an altitude of 128.25 km. The R2 profile has a maximum of 70.6 ± 7.8 kR at an altitude of 135.25 km, but its quadratic approximation shows a maximum of intensity of 67 ± 10 kR at an altitude of 124.75 km. The average ratio between the

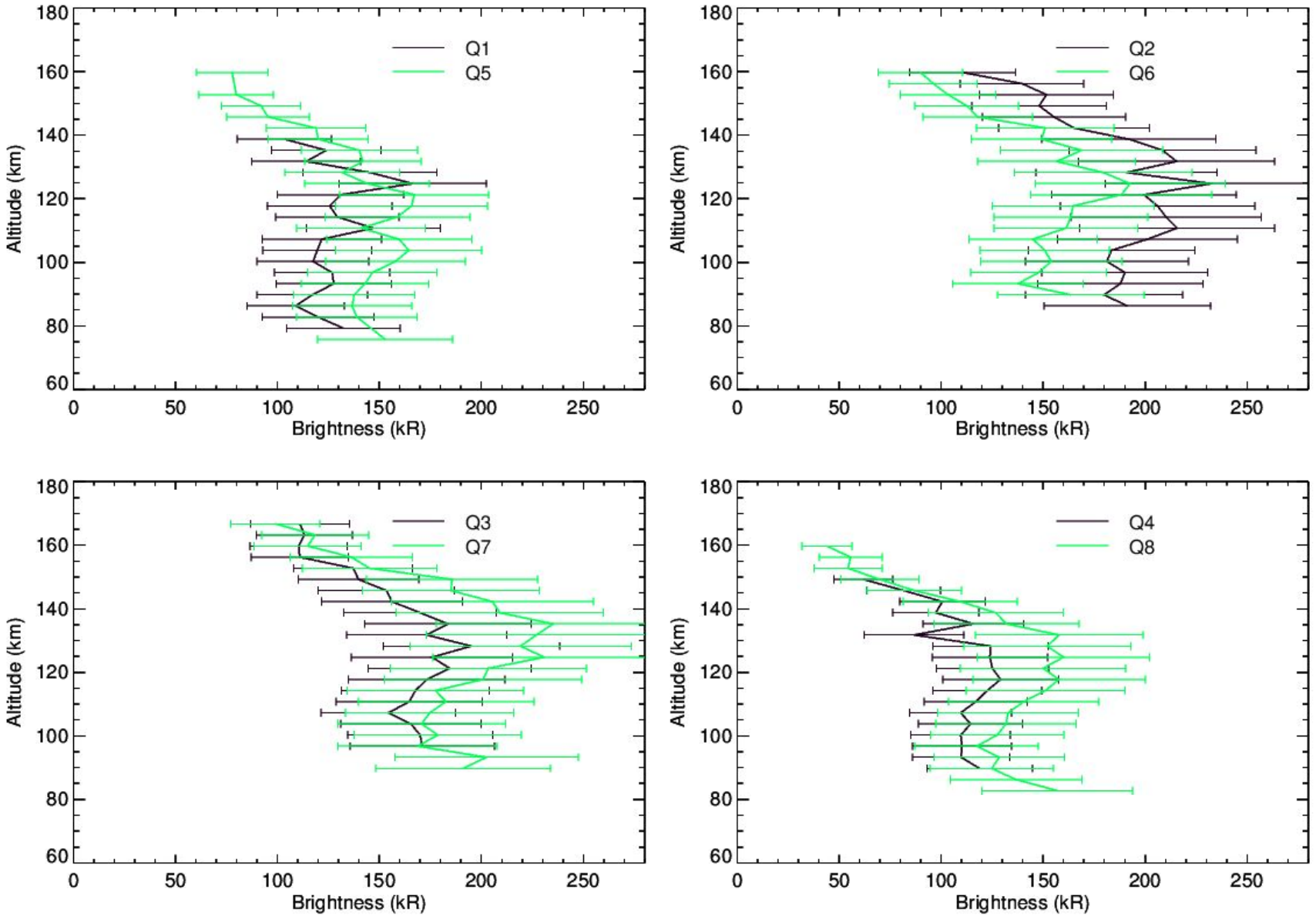


Figure 5.6.1: Average limb profiles of the Cameron band emission for the different quadrants. Each subplot represents a different solar longitude range: 26˚-116˚ (Q1-Q5), 116˚-206˚ (Q2-Q6), 206˚-296˚ (Q3-Q7) and 296˚-26˚ (Q4-Q8).

R2 profile and the R1 profile is 1.21.

Soret et al.[Soret et al., 2023] found similar results with a measured FDB peak of 75 kR at an altitude of 122.5 km.

It is difficult to make quantitative conclusion on the variation of the FDB emissions from one year to the next due to the error margins being larger than the variation itself. We can nonetheless say that the variations are very slight and could be the result of the difference in sampling.

## 5.7 Comparison with modeled data

We decided to modeled the production of the O($^1$S) state using the model described by Gkouvelis et al., 2018 [Gkouvelis et al., 2018]. We are notably trying reproduce the seasonal variation observed in the UVIS data. The temperature and the $CO_2$, CO and O density profiles were obtained from the Mars Climate Database. All data were modelled at the latitude 0° and longitude 0° point, at noon, using the dust and EUV scenario for the martian year 35. Unfortunately, we did not have acces to the MY36 scenario, thus only the results of the first revolution were reproduced. For each quadrant, we modeled the data at their midpoint (Ls = 71°, 161°, 251° and 341°), using the average SZA of the corresponding observation data, between 60 and 200 km. As prescribed by Soret et al. [Soret et al., 2022] a scaling of the density was applied to the number densities in order to compensate for the inability of MCD to correctly quantitatively describe the increase in the density of the $CO_2$ close to the perihelion. As only the scaling factors at the perihelion (1.4) and aphelion (0.5) were given, we chose an intermediate value (0.95) for both Q2 and Q4. The solar irradiance values were obtained from the data of the EUVM instrument on the MAVEN orbiter.

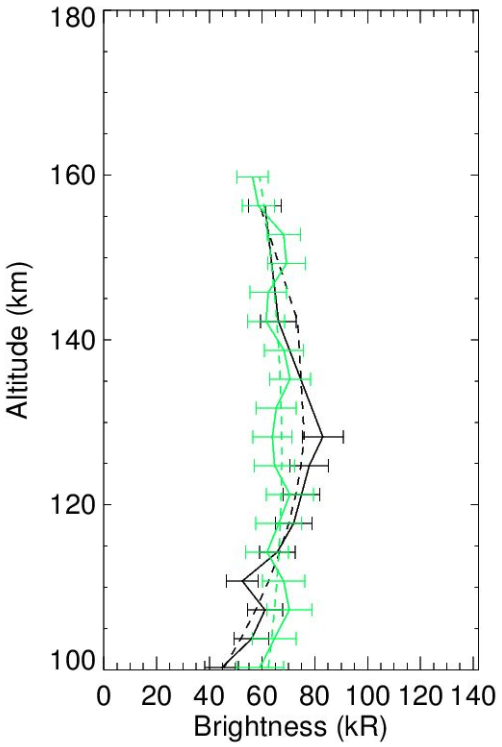


Figure 5.6.2: Average limb profiles for the FDB emission for Revolution 1 (black line) and Revolution 2 (green line) as defined in Table 4.0.1. The dashed lines are the best second degree polynomial fit. Intensities have been gathered in bins of 3.5 km in altitude.

The resulting emission density profiles are given in Figure 5.7.2. For comparison sake, Figure 5.7.1 shows the results of the modeling made by Gkouvelis et al. of the production rate in the conditions of the landing of the Viking 1 lander. It illustrates the relative importance of the different reactions in the production of the O($^1$S). Tables 5.7.1 and 5.7.2 present the quantitative results of our modeling. For each column, the quantity is given on the left and the normalised values compare to Q1 is given on the right. We only presents the results of the 557.7 nm emission as its production rate is always proportional to the one of the 297.2 nm emission.

Some caution needs to be taken when comparing the model and observation data, as one is expressed in term of volume production rate, while the other is given in intensity. This problem was previously described in Section 1. Due to time constrains, we were unfortunately not able to calculate the integral of the volume production rate over the line of sight in order to acquire the corresponding intensity. This process could be done in a following study using the method described by Hubert et al. [Hubert et al., 2022]. We opted to calculate the normalised values of the different quantities in order to offer a better mean of comparison.

The production rate and the intensity of the lower peak follow similar trends. As expected, we can see that the peak of emission given by our model are always above the peaks of intensity measured. Both altitudes show similar behavior especially if we consider the 3.5 km bin we used

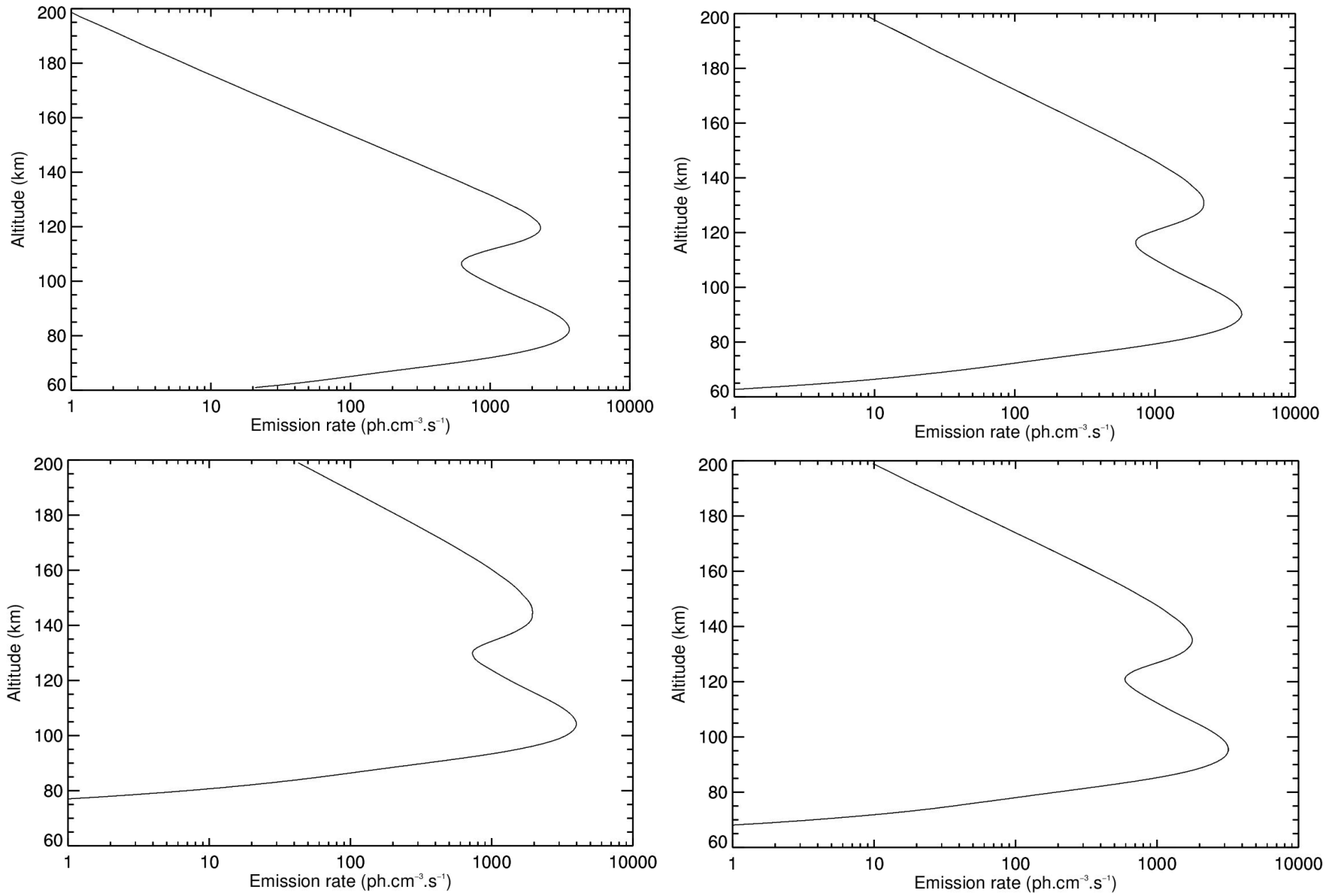


Figure 5.7.2: Volume emission rates obtained from the phtochemical model. Each figure is associated to a different quadrant. Top left is Q1, top right is Q2, bottom left is Q3 and bottom right is Q4.

for the limb profile. Overall, we see a good agreement between the modelled data and the observed data.

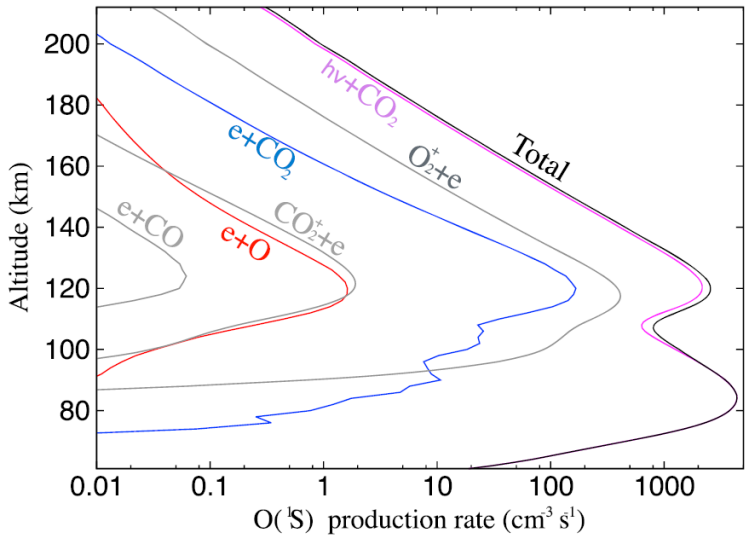


Figure 5.7.1: Volume production rate of O($^1$S) in the condition of the Viking 1 lander descent as modelled by Gkouvelis et al.[Gkouvelis et al., 2018].

Table 5.7.1: Lower peak emission rate obtained by the model compared to the lower peak intensity observed for each quadrant, as well as their altitudes. Emission rates are given in photons per cm$^3$ per second, the intensity in kR and the altitude in km.

| Quadrant | Model | | | | Observation | | | |
|---|---|---|---|---|---|---|---|---|
| | Emission rate | | Altitude | | Intensity | | Altitude | |
| Q1 | 3696.98 | 1 | 82 | 1 | 123.8 | 1 | 75.75 | 1 |
| Q2 | 4159.45 | 1.125 | 90 | 1.098 | 140.5 | 1.135 | 86.25 | 1.135 |
| Q3 | 3981.61 | 1.077 | 104 | 1.257 | 132.7 | 1.072 | 89.75 | 1.185 |
| Q4 | 3188.02 | 0.862 | 96 | 1.170 | 111.7 | 0.902 | 89.75 | 1.185 |

Table 5.7.2: Upper peak production rate obtained by the model compared to the upper peak intensity observed for each quadrant, as well as their altitudes. Emission rates are given in photons per cm$^3$ per second, the intensity in kR and the altitude in km. Asterisks indicate that there was no observation of an upper peak in the profile.

| Quadrant | Model | | | | Observation | | | |
|---|---|---|---|---|---|---|---|---|
| | Emission rate | | Altitude | | Intensity | | Altitude | |
| Q1 | 2296.40 | 1 | 120 | 1 | 57.5 | 1 | 114.25 | 1 |
| Q2 | 2225.58 | 0.969 | 131 | 1.092 | * | * | * | * |
| Q3 | 1945.95 | 0.847 | 145 | 1.208 | 59.9 | 1.042 | 128.25 | 1.123 |
| Q4 | 1778.94 | 0.774 | 135 | 1.125 | 48.4 | 0.841 | 124.75 | 1.092 |

## 5.8 Conclusion

In an attempt to identify the seasonal variation, we decided to normalize the intensity of the peaks by the intensity of the peak in the first quadrant. This treatment was applied for each emission. These results are given in Table 5.8.1. We can see that contrary to what would be expected from the purely seasonal variation, the perihelion quadrant, Q3, does not present the highest peak intensity. The highest peak intensity for R1 is instead earlier during Q2. Concerning R2, the most intense peak does occur at the perihelion during Q7. Values for Q8 tends to be higher than Q6. R1 varies much less and R2 varies much more. Overall, we can conclude that there must be another effect, on the same order as the orbital radius, affecting the intensity. We will proceed in our analysis, and see in Section 6 that this additional effect is the solar cycle.

Table 5.8.1: Average peak intensity for each quadrant for the different dayglow emissions. Values are given in kR on the left and normalized by the Q1 peak intensity on the right.

| Quadrant | 557.7 nm | | 297.2 nm | | UVD | | Cameron | |
|---|---|---|---|---|---|---|---|---|
| Q1 | 123.8 | 1 | 7.1 | 1 | 19.6 | 1 | 166 | 1 |
| Q2 | 140.5 | 1.135 | (>8.7) | (>1.225) | 28.6 | 1.459 | 233 | 1.403 |
| Q3 | 132.7 | 1.072 | 6.95 | 0.979 | 25.5 | 1.301 | 195 | 1.175 |
| Q4 | 111.7 | 0.902 | 6.8 | 0.958 | 20.6 | 1.051 | 129 | 0.777 |
| Q5 | 107.4 | 0.868 | 6.61 | 0.931 | 23.6 | 1.204 | 167 | 1.006 |
| Q6 | 142.8 | 1.153 | 8.5 | 1.197 | 32.2 | 1.643 | 192 | 1.157 |
| Q7 | 187.6 | 1.515 | 11.3 | 1.592 | 43.0 | 2.19 | 235 | 1.416 |
| Q8 | 171.1 | 1.382 | 10.61 | 1.494 | 35.6 | 1.816 | 160 | 0.964 |

# 6. Time variations

As the airglow results from photochemical processes, solar irradiance variations will lead to variation of the airglow itself. The two main phenomena controlling the incoming light intensity are the solar cycle and the position of Mars on its orbit.

The solar cycle is an 11-year periodic variation of the Sun surface conditions, which in turn produces a cyclic variation of the solar radiation. We are currently in the Solar Cycle 25, the 25th cycle since 1755 the beginning of recording of the number of solar sunspots, a good indicator of the solar activity. The ultraviolet irradiance tends to vary more than the rest of the solar spectrum. Those are important frequencies as they fuel the photochemical network in the Martian atmosphere. Figure 6.0.1 shows the solar cyles since 1980 through the number of sunspots over time, as well as the time periods R1 and R2.

The second phenomenon is simply the ellipticity of the Martian orbit. A simple analysis of the orbit using the Kepler formula can give us the ratio between the orbital radius at aphelion and perihelion. Since the Martian ellipticity is 0.0934, we have $\frac{r_{min}}{r_{max}} = \frac{1-e}{1+e} = 0.829$. In turn, the irradiance varies as $R^{-2}$, where R is the distance between the Sun and Mars. The ratio between the aphelion and the perihelion irradiances is therefore $\frac{I_{min}}{I_{max}} = \frac{R_{min}^{-2}}{R_{max}^{-2}} = 1.455$. This back-of-the-envelope calculation give us a good estimate of the variation of irradiance we can expect between the perihelion and the aphelion.

Let us consider once more the result of the previous section. We reproduced Table 5.8.1 as Table 6.0.1 for ease of reading. It is interesting to note that the variations between aphelion and perihelion are nowhere close to the approximation of 1.455 we just made. We will see that this a consequence of the variation in the solar activity from R1 to R2.

The outcome of the two effects on the irradiance is being precisely observed from orbit around Mars, by the EUV Monitor on-board the MAVEN spacecraft (see Sect. 2). In the following analysis, we will compare the evolution of the intensity and the altitude of the peak brightness with the irradiance measured by EUVM, at the wavelength responsible for the airglow. For example, we paire the 557.7 nm airglow intensity with the Lyman $\alpha$ irradiance. Then, in a second time, we will correlate the intensity of emission peak with the reaction rate constant of the main reaction leading to the formation of the source of our different airglow emission and the altitude with the inverse of the square of the orbital radius.

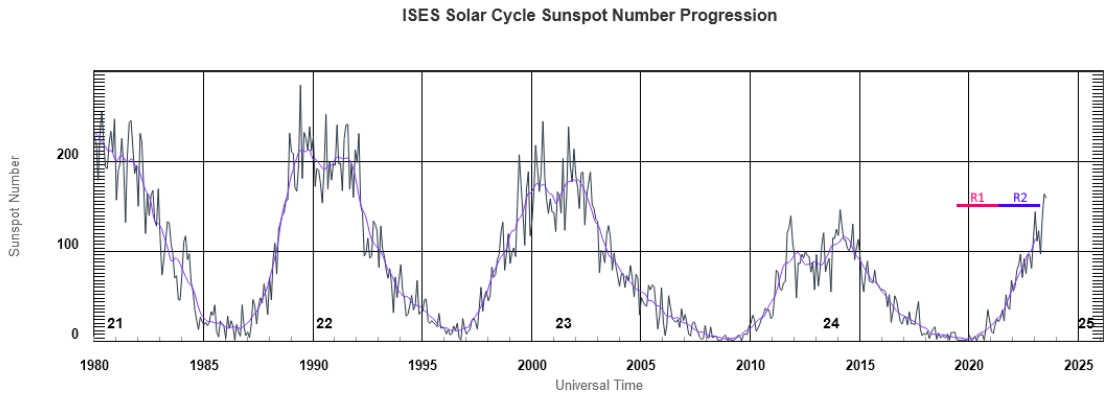


Figure 6.0.1: In black, the mean monthly sunspot number, and in purple, the sunspot number smoothed over 13-month. The R1 and R2 time periods have been drawn respectively in red and blue. Number above the horizontal axis marks the number of the solar cycles. This plot was generated on an online tool provided by NOAA/SWPC (https://www.swpc.noaa.gov/products/solar-cycle-progression) using data from both NOAA/SWPC/SWO and ROB/SIDC-SILSO.

Table 6.0.1: Average peak intensity for each quadrant for the different dayglow emissions. Values are given in kR on the left and normalized by the Q1 peak intensity on the right.

| Quadrant | 557.7 nm | | 297.2 nm | | UVD | | Cameron | |
|---|---|---|---|---|---|---|---|---|
| Q1 | 123.8 | 1 | 7.1 | 1 | 19.6 | 1 | 166 | 1 |
| Q2 | 140.5 | 1.135 | (>8.7) | (>1.225) | 28.6 | 1.459 | 233 | 1.403 |
| Q3 | 132.7 | 1.072 | 6.95 | 0.979 | 25.5 | 1.301 | 195 | 1.175 |
| Q4 | 111.7 | 0.902 | 6.8 | 0.958 | 20.6 | 1.051 | 129 | 0.777 |
| Q5 | 107.4 | 0.868 | 6.61 | 0.931 | 23.6 | 1.204 | 167 | 1.006 |
| Q6 | 142.8 | 1.153 | 8.5 | 1.197 | 32.2 | 1.643 | 192 | 1.157 |
| Q7 | 187.6 | 1.515 | 11.3 | 1.592 | 43.0 | 2.19 | 235 | 1.416 |
| Q8 | 171.1 | 1.382 | 10.61 | 1.494 | 35.6 | 1.816 | 160 | 0.964 |

Before we can properly analyse our data, a correction has to be applied. Indeed, problems may arise when one tries to draw conclusions from a large sample of data collected at different points in time and space. For example, as we draw the average limb profiles for the eight quadrants defined previously, we are combining measurements made in drastically different conditions. The solar zenithal angle, for example, may theoretically vary from 0° to 70° from one spectrum to the next. A correction is necessary if we want to dampen this variation and isolate the one we are studying, in this case temporal variation.

Using the Chapman layer theory, a model of the absorption by a single absorber of a monochromatic radiation, Gkouvelis et al. [Gkouvelis et al., 2018] found the following expressions for the corrections of the emission :

$$B_o = \frac{B}{cos(\theta)},$$

where $B$ is the peak intensity measured at a SZA of $\theta$, $B_o$ the peak intensity in the same conditions at a SZA of 0°. This is a direct consequence of the geometry of the problem. Figure 6.0.2 shows the peak intensity of the green emission normalised by the Lyman $\alpha$ irradiance as a function of the SZA. We can clearly see that when we dampen the irradiance effect, the peak intensity is proportional to the cosinus of the SZA.

The correction of the altitude is less straight forward. Gkouvelis et al. (2018) propose, based on results from climate model, the following formula for the altitude of the maximum of intensity of the 297.2 nm emission :

$$Z^{\theta}_{max} = z_o + H \ln([CO_2]_{z_o} \sigma_{Ly-\alpha} H / \cos\theta),$$

where $Z^{\theta}_{max}$ is the altitude of the peak of intensity for a SZA of $\theta$, $z_o$ is a reference altitude, H is the scale height of the $CO_2$, $[CO_2]_{z_o}$ is the number density of the $CO_2$ at the reference altitude $z_o$, $\sigma_{Ly-\alpha}$ is the absorption cross-section of the $CO_2$ at the Lyman-$\alpha$ wavelength. It is possible to rearrange this formula into a more practical form, with the following operations :

$$\begin{aligned}
Z^{\theta}_{max} &= z_o + H \ln([CO_2]_{z_o} \sigma_{Ly-\alpha} H) + \ln(1/\cos\theta), \\
Z^{\theta}_{max} &= Z^{0}_{max} + H \ln(1/\cos\theta), \text{ where } Z^{0}_{max} = z_o + H \ln([CO_2]_{z_o} \sigma_{Ly-\alpha} H) \\
Z^{0}_{max} &= Z^{\theta}_{max} - H \ln(1/\cos\theta),
\end{aligned}$$

where $Z^{0}_{max}$ is the altitude of the maximum of intensity in the same conditions as $Z^{\theta}_{max}$, with the exception of a SZA equal to 0°.

Gkouvelis et al. [Gkouvelis et al., 2020] describe how in theory, the peak of emission of the 297.2 nm airglow should occur at a pressure of $39 \pm 3$ mPa for SZA lower than 75°. Furthermore, they found a best fitting value of the scale height to be 7.1 km based on photochemical model, with a correlation of 0.98 on their fit . This value was used by Soret et al. [Soret et al., 2022] to study the temporal variation of the 297.2 nm airglow emission.

The validity of this correction is limited by the approximation of the model, which requires a monochromatic radiation. We can nonetheless notice that the final expression of the altitude, that the difference between the corrected and non-corrected altitudes only depend on the geometry

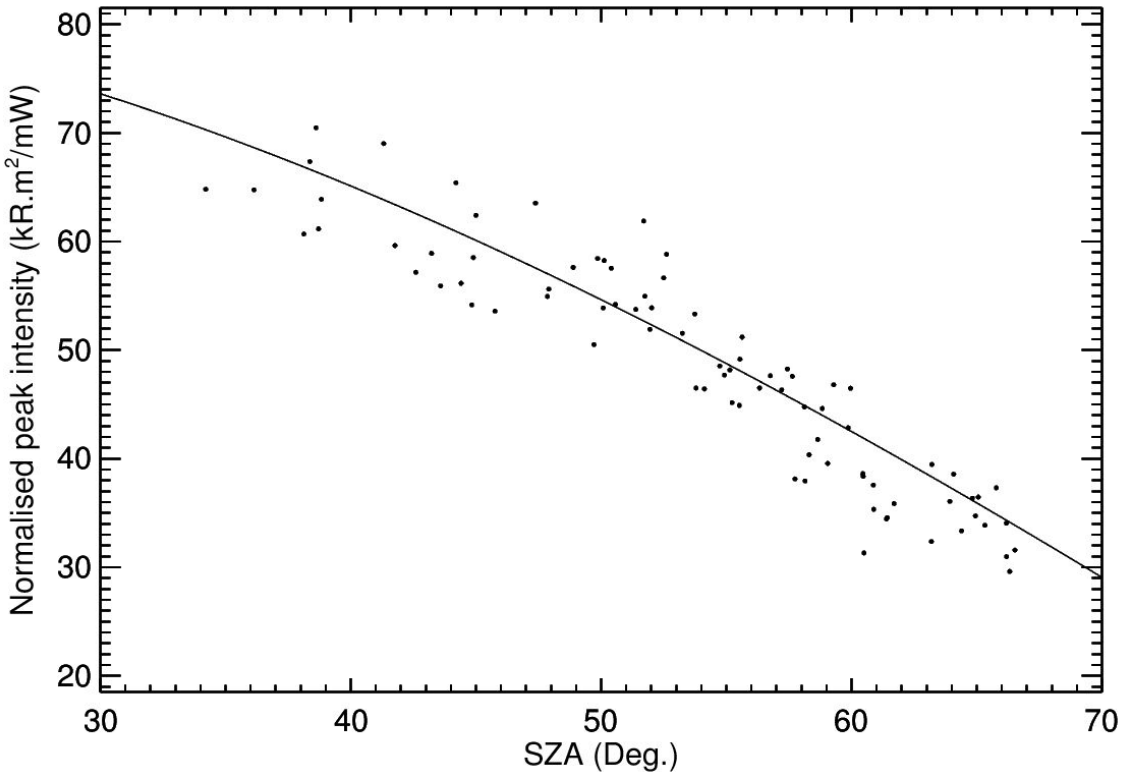


Figure 6.0.2: Dots show peak intensities normalised by the Lyman $\alpha$ irradiance as a function of the SZA. Black line is the cosine of the SZA.

of the situation. We predict that this correction is still a good approximation of the correction to the altitude, even in the case of a polychromatic absorption of light. In an attempt to verifiy this claim, we will discuss in the current section both corrected to non-corrected values when the monochromatic radiation cannot be expected.

The workflow used to analyse the time variation is the following :
First, we subdivided the dataset into the different limb scans. The resulting data will lose in precision for the intensity, but offer the largest sample of data. If a correction should be applied to the brightness and altitude, it was applied at this time. For each spectrum, we identified the intensity and respective error margins for the different wavelengths of interest. This allowed us to find the peak of the limb profile. Using the EUVM data, we identified the effective irradiance for the wavelengths of interest. Some data points needed to be rejected, as the dataset of EUVM has some gap periods. We rejected any data where we couldn't find a corresponding EUVM measurement closer than three days apart. As the EUVM measurements are averaged over a period of 6 hours, most of the data pair have less than 6 hours of difference.

Two types of plots were produced during this analysis. The first type is a plot of the variation of the airglow peak intensity over time, correlated with another data, either the irradiance or the reaction rate. The second is a plot of the airglow peak intensity as a function of the correlated data itself, with a linear model fit drawn on top. The analysis of this linear model produced multiple results. We will be using the R-value to estimated this fit. It is defined as follows:

$$R = \sqrt{1 - \frac{\sum (y_f^i - y_d^i)^2}{\sum (\bar{y} - y_d^i)^2}},$$

where $y_f^i$ is the value predicted by our model, $y_d^i$ is the value measured and $\bar{y}$ is the mean value of our dataset. This formula produces an R-value between 0 and 1. The closer the value is from 1, the better the fit of our model to our data.

A similar analysis was made for the altitude of the peak, but correlated this time with either the irradiance or the inverse of the square of the orbital radius. Indeed, this value reflects more accurately the expansion of the Martian atmosphere than any single-wavelength irradiance value

[Haberle, 2015]. Cox et al.[Cox et al., 2010] suggest that the prime factor controlling the peak altitude of both the UVD and Cameron emissions is the $CO_2$ density profile, itself related to the seasonal expansion of the atmosphere.

## 6.1 557.7 nm airglow variations

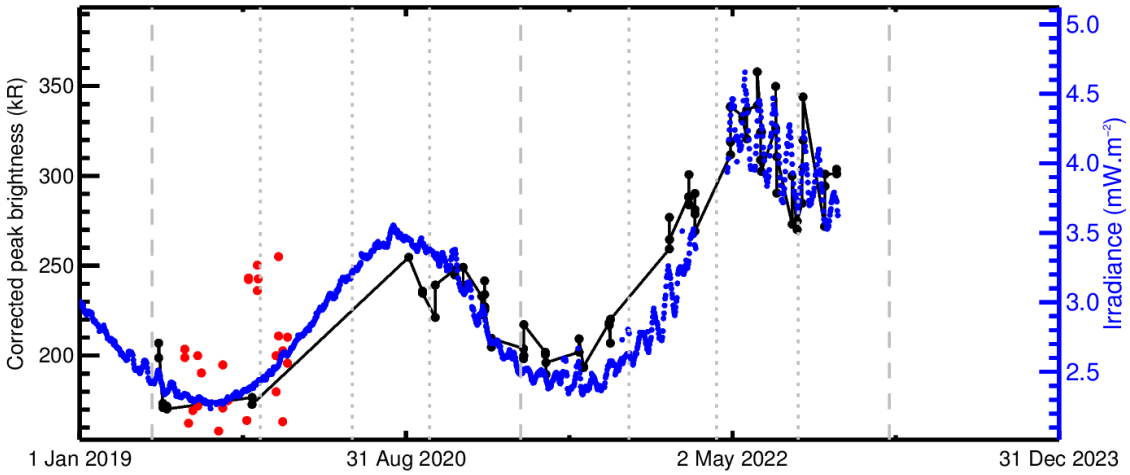


Figure 6.1.1: In black, the corrected peak brightness of the 557.7 nm airglow obtained from the 1024 bin data, given in kR. In red, the corrected peak brightness of the 557.7 nm airglow obtained from the 256 bin data. In blue, the 121.5 nm irradiance over time, given in $\mathrm{mW.m^{-2}}$. Both axes have been scaled and cropped to fit both curves as close as possible in order to present the correlation.

Let us consider the main reaction responsible for the formation of the $O(^1s)$ state.

$$CO_2 + h\nu \longrightarrow CO + O(^1s)$$

We need to remember that we are studying the lower peak of intensity, which finds its origin from the Lyman-$\alpha$ photons. While the irradiance presents a strong peak of intensity at this wavelength, the cross-section is very low. At lower altitude, around 90 km, the density becomes high enough and produces a second peak [Gkouvelis et al., 2018]. We can therefore consider the intensity of the Lyman-$\alpha$ peak as our effective irradiance for the oxygen emission. Concretely, we integrate the irradiance from 120.5 to 122.5 nm.

We were able to measure a peak in 89 of the limb profiles. We also found 29 peaks for the 256-bin observations. We can observe in Figure 6.1.1 that there seems to be a good correlation between the corrected peak brightness of the 557.7 nm airglow and the Lyman $\alpha$ irradiance. To quantitatively describe this relation, we found the best-fitting linear model between both data. We can write it in the following form:

$$a \times I + b = B,$$

where $a$ and $b$ are two parameters that have to be estimated, $I$ is the irradiance and $B$ is the resulting brightness of the airglow. The $a$ parameter represents how the intensity increases per unit of irradiance. The $b$ parameter is the intensity when the irradiance is zero. This parameter does not hold much physical signification, as the linear model most likely does not stand for near zero irradiance.

For the 557.7 nm airglow, the best fit has the parameter values $a = 77.69$ and $b = 0.01$. The R-value of our model is very good, reaching 0.939. Figure 6.1.2 presents both our dataset and the best fit. As previously mentioned, this model is only based on the 1024-bin data. We can see in Figure 6.1.4 the fit and the scatter plot of the corrected peak altitude as a function of the Lyman-$\alpha$ effective irradiance.

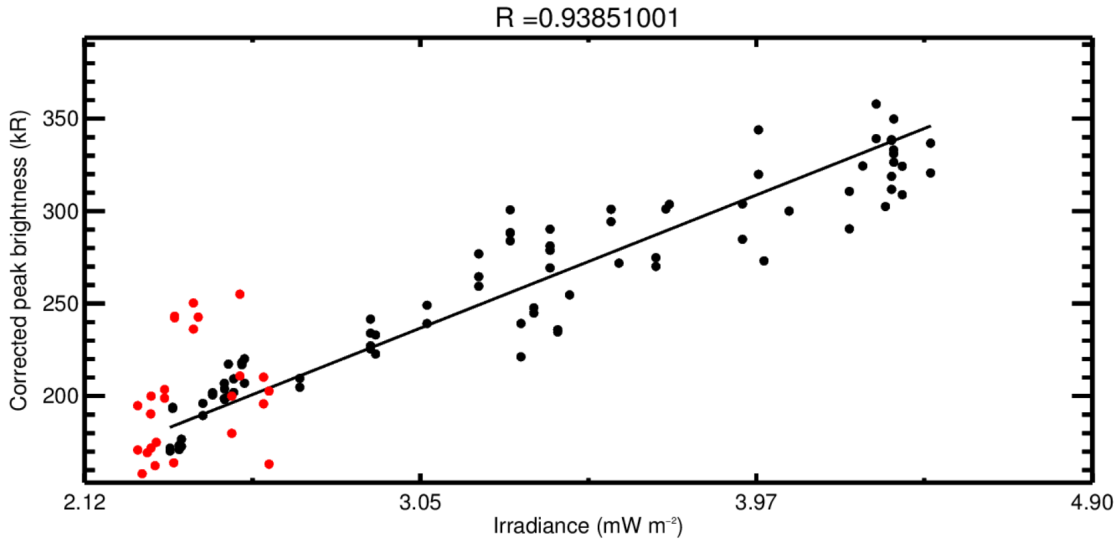


Figure 6.1.2: Black and red dots represent the corrected peak intensity for respectively the 1024 and 256 bin data. The black line shows the best fitting linear model for the 1024 bin dataset.

Regarding the altitude variation, we can identify a similar correlation with the Lyman-$\alpha$ irradiance. Its statistical significance is not as good as the one for the intensity. Figure 6.1.3 shows the corrected altitude of the peak of intensity of the 557.7 nm emissions, overlaid with the effective irradiance of the 557.7 nm emissions.

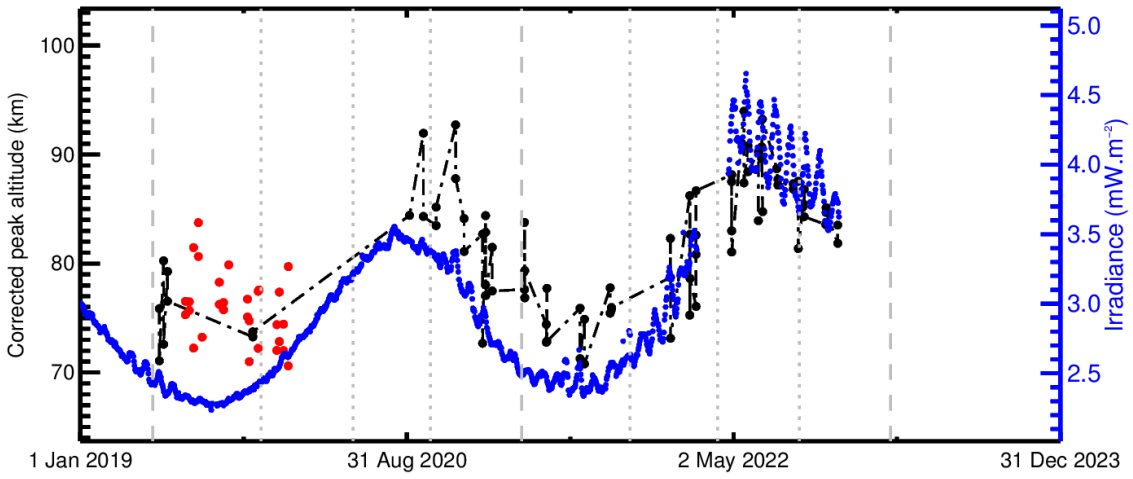


Figure 6.1.3: In black, the corrected altitude of the 557.7 nm airglow peak of intensity over time, given in km. In red, the corrected altitude of the 557.7 nm airglow peak of intensity over time for the 256-bin data. In blue, the Lyman-$\alpha$ irradiance over time, given in mW.m$^{-2}$. Both axes have been scaled and cropped to fit both curves as close as possible in order to present the correlation.

A linear model was also made for the corrected altitude as a function of the irradiance of the Lyman-$\alpha$ peak. The resulting parameters are $a = 6.59$ and $b = 60.02$. The associated R-value is 0.797. While this correlation is not as good as the one found for the brightness or the one for the altitude correction found by Gkouvelis et al. [Gkouvelis et al., 2020], it remains nonetheless significative. A previous study crossing data from UVIS and the Martian Climate Database atmospheric model suggests that the density of the overlying $CO_2$ column was the sole variable controlling the altitude of the lower peak of the 297.2 nm airglow [Gkouvelis et al., 2018]. As the 297.2 nm and the 557.7 nm airglow share a common origin, both should produce a peak of intensity at the same altitude.

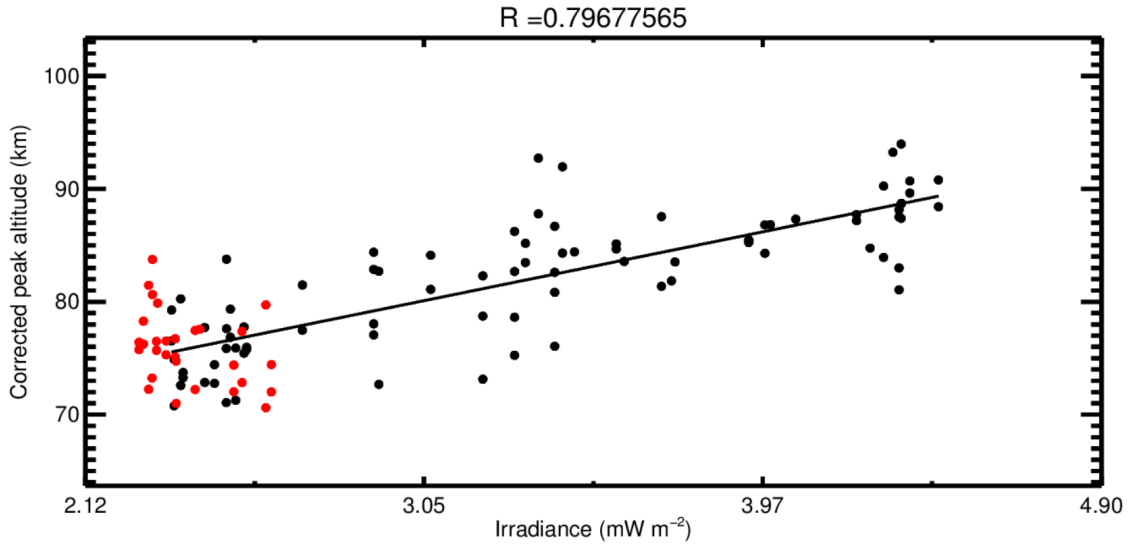


Figure 6.1.4: Black and red dots represent the corrected altitude of the peak intensity respectively for the 1024 and 256-bin data. The black line shows the best fitting linear model for the dataset.

## 6.2 297.2 nm airglow variation

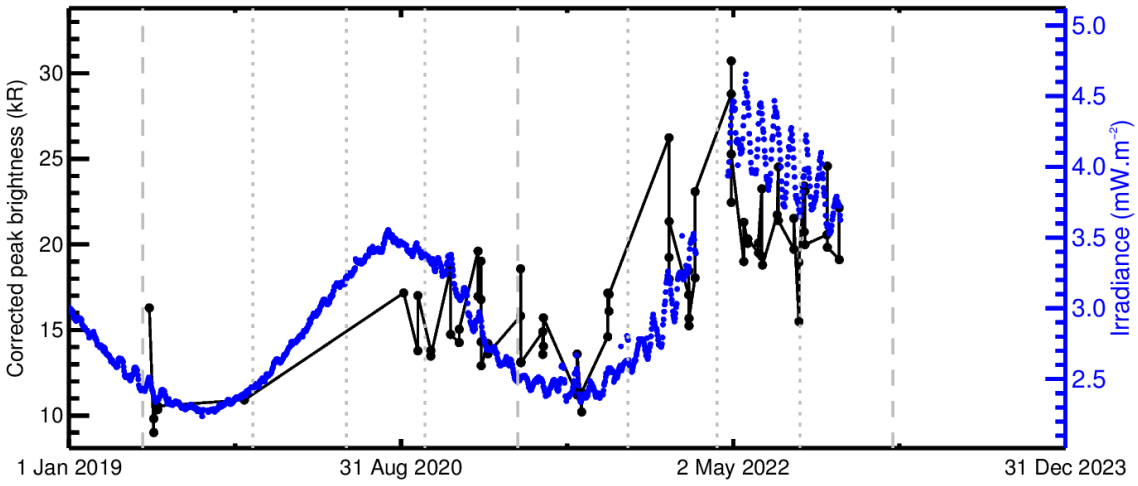


Figure 6.2.1: In black, the corrected peak brightness of the 297.2 nm airglow over time, given in kR. In blue, the 121.5 nm irradiance over time, given in mW.m$^{-2}$. Both axes have been scaled and cropped to fit both curves as close as possible in order to present the correlation.

We were able to measure a peak in the limb profile 83 times. Figure 6.2.1 shows both the brightness of the 297.2 nm line and the Lyman $\alpha$ irradiance as a function of time. The 297.2 nm peak uses the same correction as the 557.7 nm. The parameters of the best fit are $a = 5.30$ and $b = -0.63$. The associated R-value is 0.735. The fit is presented in Figure 6.2.2.

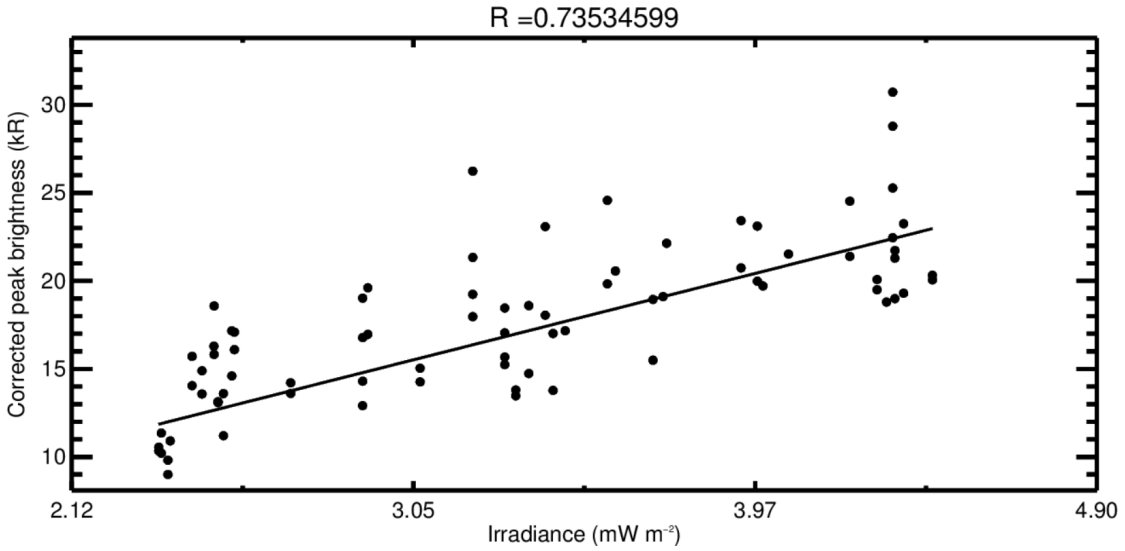


Figure 6.2.2: Black dots represent the corrected peak intensity of the 297.2 nm as a function of the irradiance. The black line shows the best fitting linear model for the dataset.

Concerning the altitude, we expect in theory to observe the same value for the 297.2 nm than for the 557.7 nm. Figure 6.2.3 presents both the corrected altitude of the peak in intensity of the 297.2 nm airglow and the Lyman $\alpha$ irradiance over time.

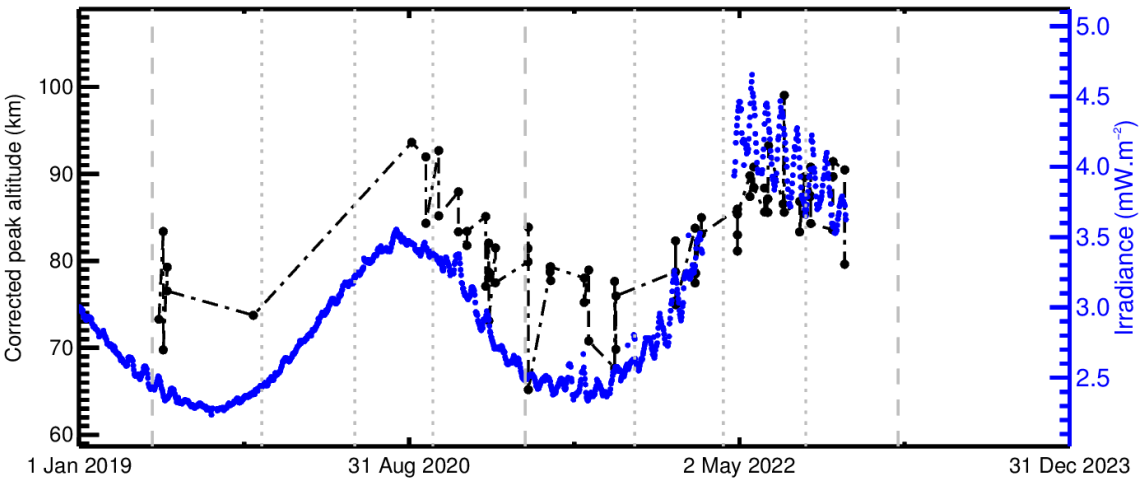


Figure 6.2.3: In black, the corrected altitude of the 297.2 nm airglow peak of intensity over time, given in kR. In blue, the Lyman-$\alpha$ irradiance over time, given in mW.m$^{-2}$. Both axes have been scaled and cropped to fit both curves as close as possible in order to present the correlation.

The best fit for the corrected altitude of the peak of the 297.2 nm airglow as a function of the Lyman $\alpha$ irradiance has the associated parameters $a = 6.43$ and $b = 61.03$. The R-value of the model is 0.700. A conclusion similar to the one of the 557.7 nm case can be made and, as expected, the 557.7 nm and 297.2 nm altitude have similar parameter values. We can see in Figure 6.2.4 the fit and the corrected peak altitude as a function of the Lyman-$\alpha$ irradiance.

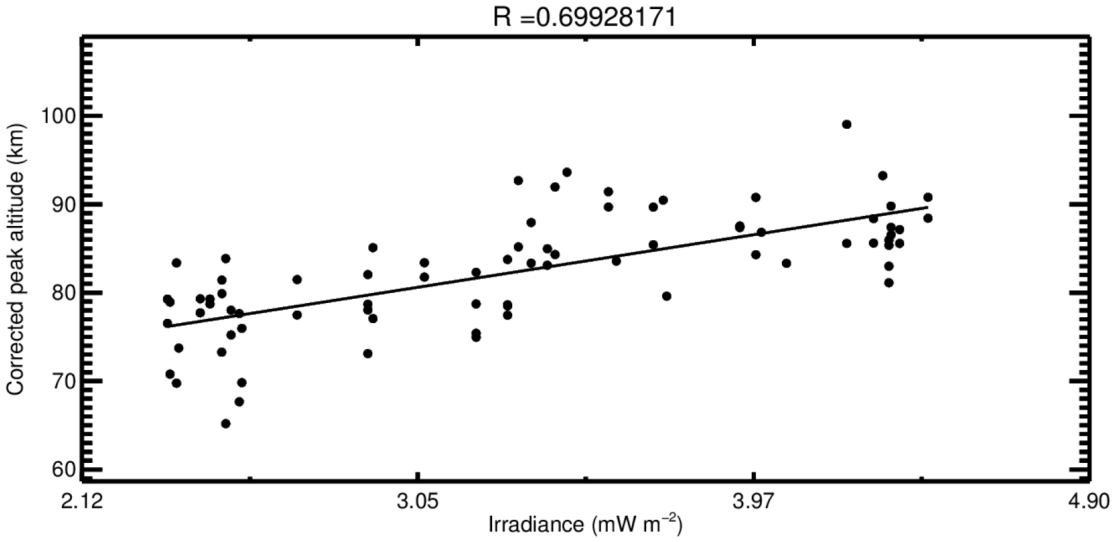


Figure 6.2.4: Black dots represent the corrected altitude of the peak intensity of the 297.2 nm as a function of the Lyman-$\alpha$ irradiance. The black line shows the best fitting linear model for the dataset.

## 6.3 UVD airglow variation

The main production reaction of the $CO_2{}^+(B^2\Sigma)$ energy state, responsible for the UVD emissions, is the following photodissociation :

$$CO_2 + h\nu \longrightarrow CO_2{}^+(B^2\Sigma) + e,$$

with photons of wavelength shorter than 69 nm. We therefore selected the range of the irradiance where wavelengths are shorter than this value and integrated it to form our effective irradiance for the UVD emission process. Although lower, the resulting energy flux is on the same order of magnitude as the one of the Lyman-$\alpha$ peak. The solar irradiance at the aphelion of MY35 is given in Figure 6.3.1. We can clearly see this portion of the spectrum is dominated by the 30.4 nm He II line.

As mentioned earlier, the corrections based on the Chapman layer theory only apply for a monochromatic radiation. We will demonstrate that Gkouvelis correction for the oxygen is nonetheless an adequate approximation for other emissions.

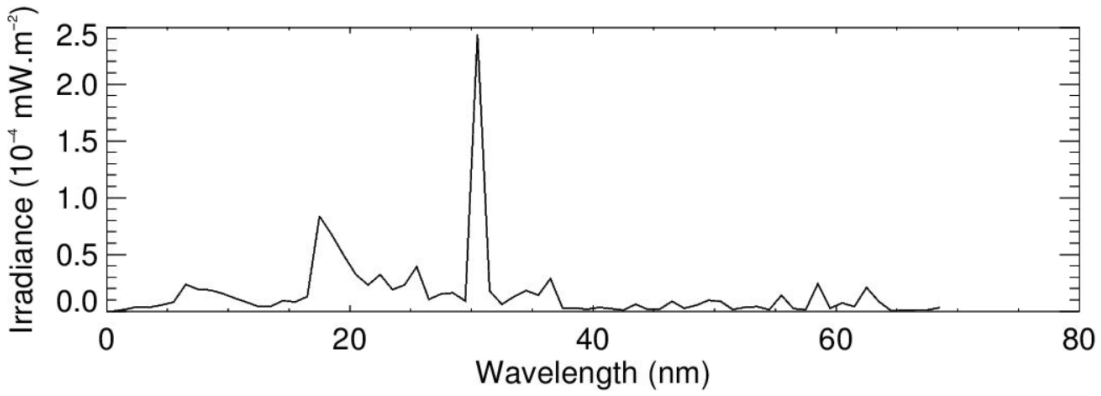


Figure 6.3.1: Spectrum of the effective Solar irradiance for the production of the $CO_2{}^+(B^2\Sigma)$ energy state, responsible for the UVD airglow. The highest peak is the 30.4 nm He II emission line.

### 6.3.1 Uncorrected data

The peak brightness in the UVD limb profile for the uncorrected data was measured 89 times. Figure 6.3.2 shows both the brightness of the UVD emission and the UVD effective irradiance as a function of time. The parameters of the best-fitting model are $a = 28.29$ and $b = 3.45$. The associated R-value is 0.759. The fit is presented in Figure 6.3.3.

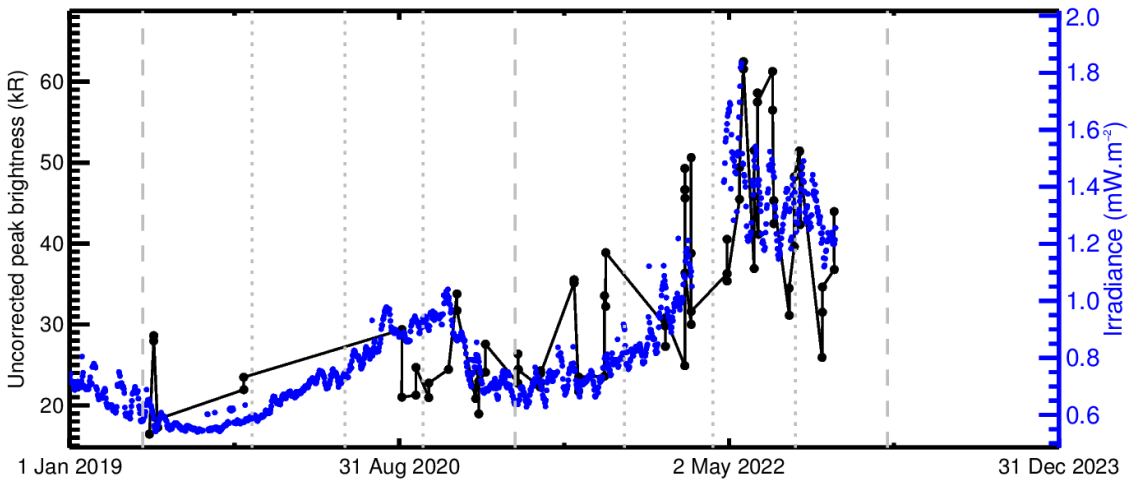


Figure 6.3.2: In black, the uncorrected peak intensity of the UVD airglow over time, given in kR. In blue, the UVD effective irradiance over time, given in $\mathrm{mW.m^{-2}}$. Both axes have been scaled and cropped to fit both curves as close as possible in order to present the correlation.

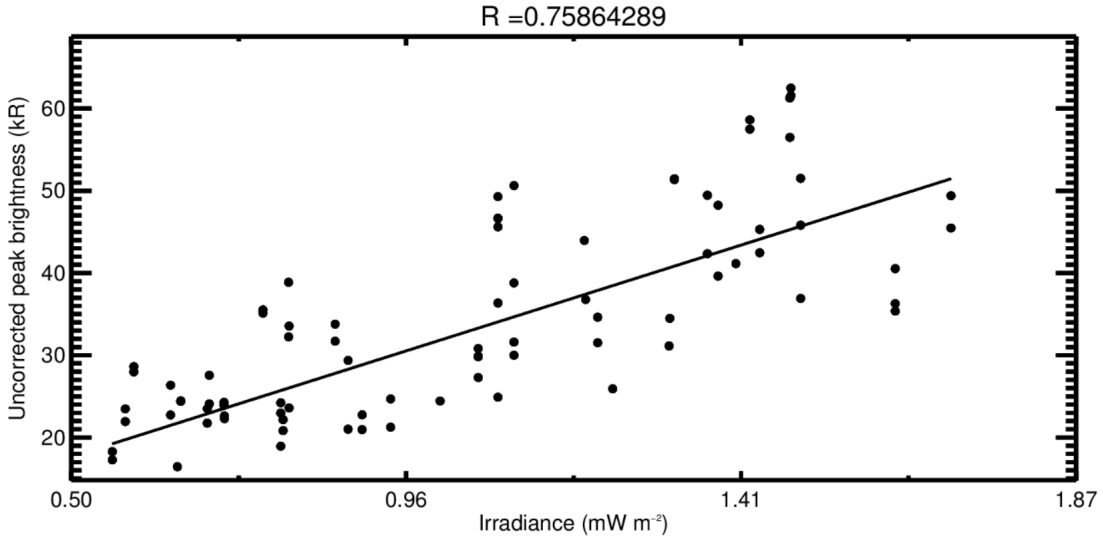


Figure 6.3.3: Black dots represent the uncorrected peak intensity of the UVD emission as a function of the irradiance. The black line shows the best fitting linear model for the dataset.

Figure 6.3.4 presents both the uncorrected peak altitude of the UVD airglow and the UVD effective irradiance over time.

The best fit for the uncorrected peak altitude of the UVD airglow as a function of the UVD effective irradiance has the associated parameters $a = 16.92$ and $b = 105.63$. The associated R-value of the model is 0.625. We can see in Figure 6.3.5 the fit and the scatter plot of the corrected peak altitude as a function of the UVD effective irradiance.

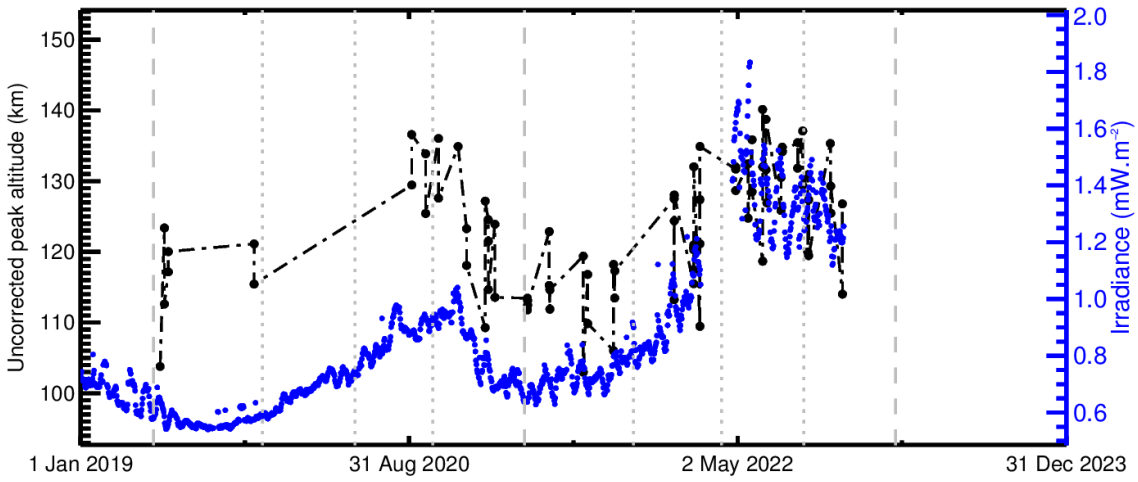


Figure 6.3.4: In black, the uncorrected altitude of the UVD airglow peak altitude over time, given in km. In blue, the UVD effective irradiance over time, given in $\mathrm{mW.m^{-2}}$. Both axes have been scaled and cropped to fit both curves as close as possible in order to present the correlation.

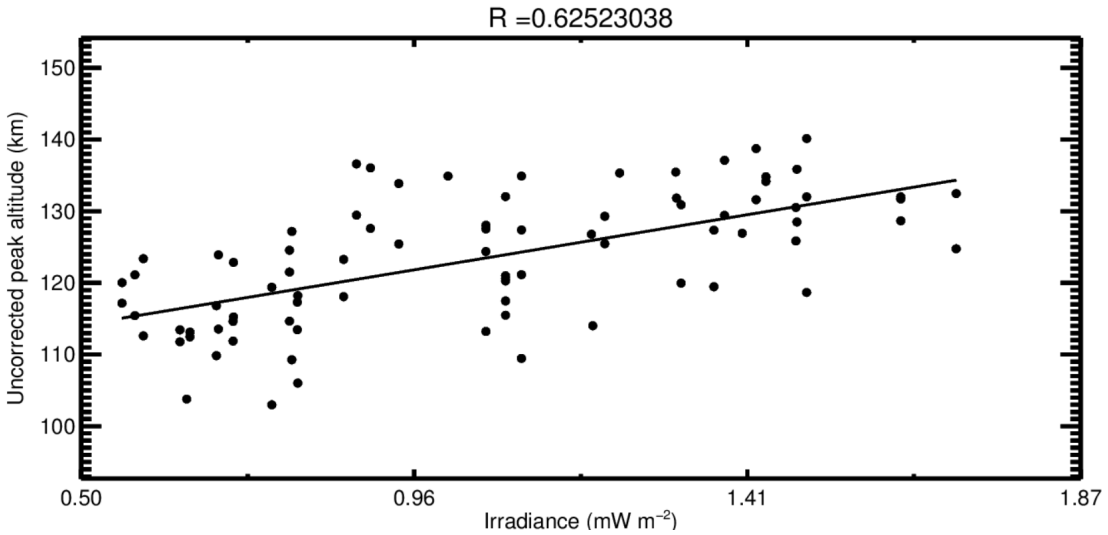


Figure 6.3.5: Black dots represent the uncorrected altitude of the peak intensity of the UVD emissions as a function of the irradiance. The black line shows the best fitting linear model for the dataset.

### 6.3.2 Corrected data

The peak in the UVD limb profile was measured 90 times. Figure 6.3.6 shows both the brightness of the UVD emissions and the UVD effective irradiance as a function of time. The parameters of the best-fitting model are $a = 56.39$ and $b = -0.76$. The associated R-value is 0.912. The fit is presented in Figure 6.3.7.

Figure 6.3.8 presents both the corrected altitude of the peak in intensity of the UVD airglow and the UVD effective irradiance over time.

The best fit for the corrected altitude of the peak in intensity of the UVD airglow as a function of the UVD effective irradiance has the associated parameters $a = 7.95$ and $b = 95.28$. The R-value of the fit is 0.690. We can see in Figure 6.3.9 the fit and the scatter plot of the corrected peak altitude as a function of the Lyman $\alpha$ irradiance.

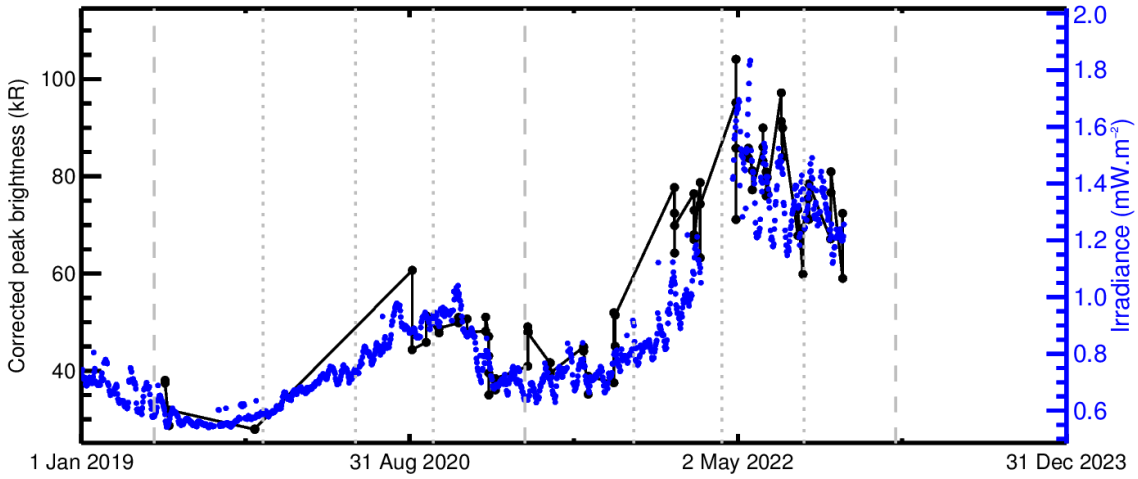


Figure 6.3.6: In black, the corrected peak intensity of the UVD airglow over time, given in kR. In blue, the UVD effective irradiance over time, given in $\mathrm{mW.m^{-2}}$. Both axes have been scaled and cropped to fit both curves as close as possible in order to present the correlation.

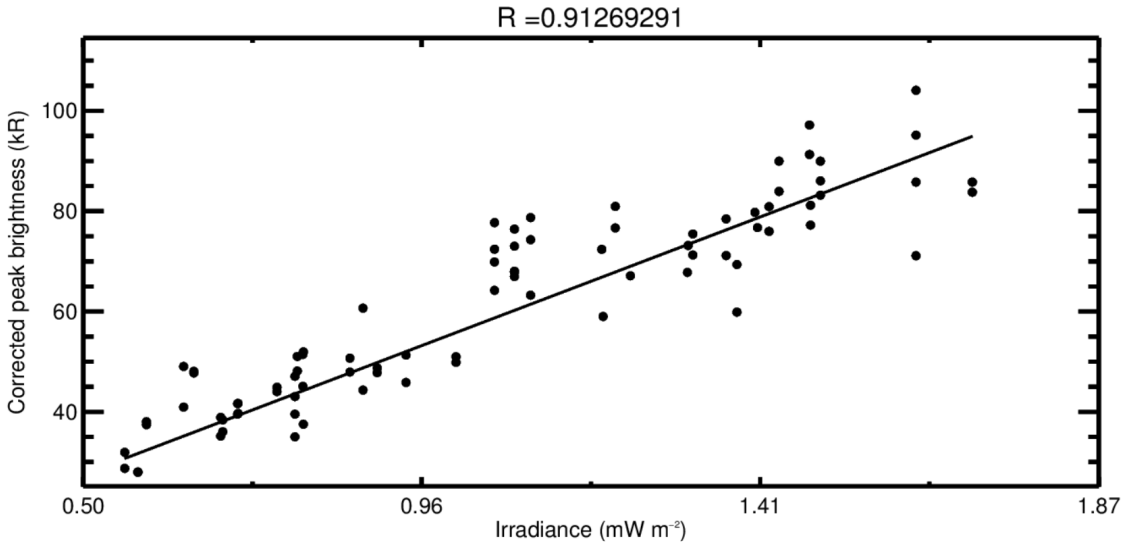


Figure 6.3.7: Black dots represent the corrected peak intensity of the UVD emission as a function of the irradiance. The black line shows the best fitting linear model for the dataset.

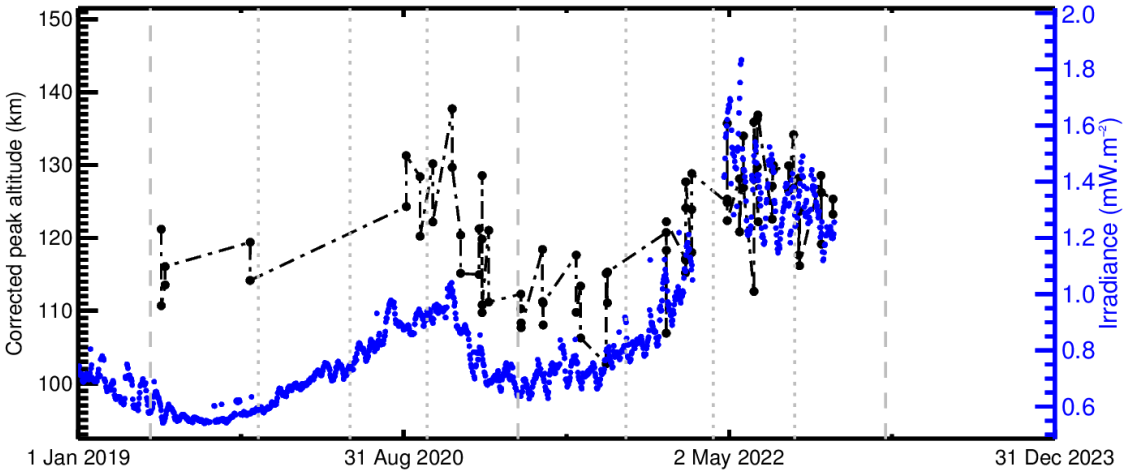


Figure 6.3.8: In black, the corrected altitude of the UVD airglow peak of intensity over time, given in kR. In blue, the 121.5 nm irradiance over time, given in mW.m$^2$. Both axes have been scaled and cropped to fit both curves as close as possible in order to present the correlation.

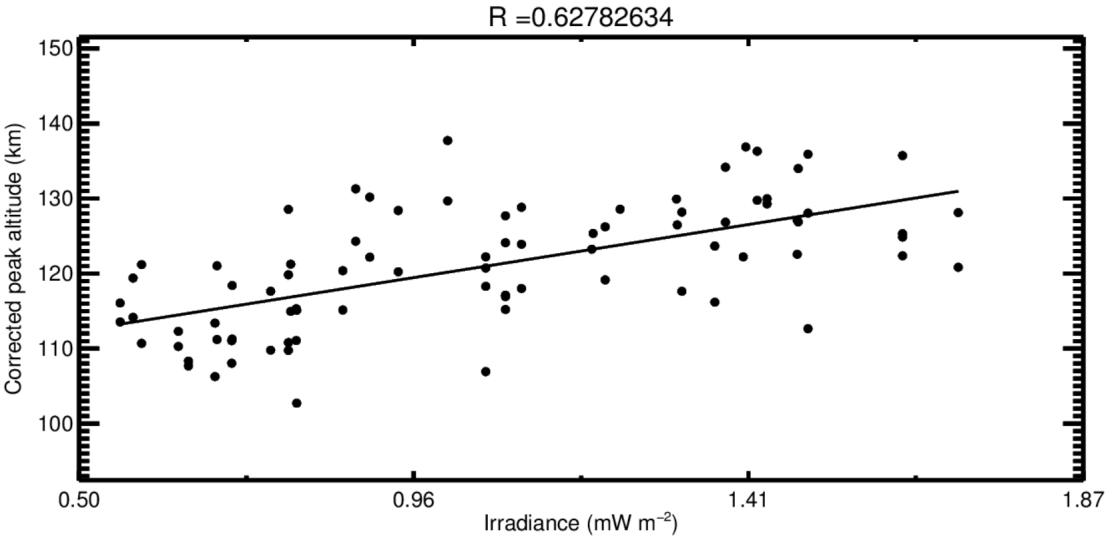


Figure 6.3.9: Black dots represent the corrected altitude of the peak intensity of the UVD altitude as a function of the UVD effective irradiance. The black line shows the best fitting linear model for the dataset.

## 6.4 Cameron airglow variation

Contrary to the case of the UVD emission where its emitter $CO_2{}^+(B^2\Sigma)$ had a predominant reaction of formation, $CO(a^3\Pi)$ formation results from a combination of electrodissociation and photodissociation of $CO_2$. It is difficult to reduce the intensity of this complex process into a single number. As a first estimate, we decided to consider only the photodissociation and its associated effective irradiance for our analysis.

This effective spectrum for the Cameron emission includes all wavelengths shorter than 108 nm. The Solar irradiance at the perihelion of MY35 is given in Figure 6.4.1. Similarly to the UVD effective irradiance, the Cameron effective irradiance is on the same order as the one of the Lyman-$\alpha$ peak and is dominated by the 30.4 nm He II line.

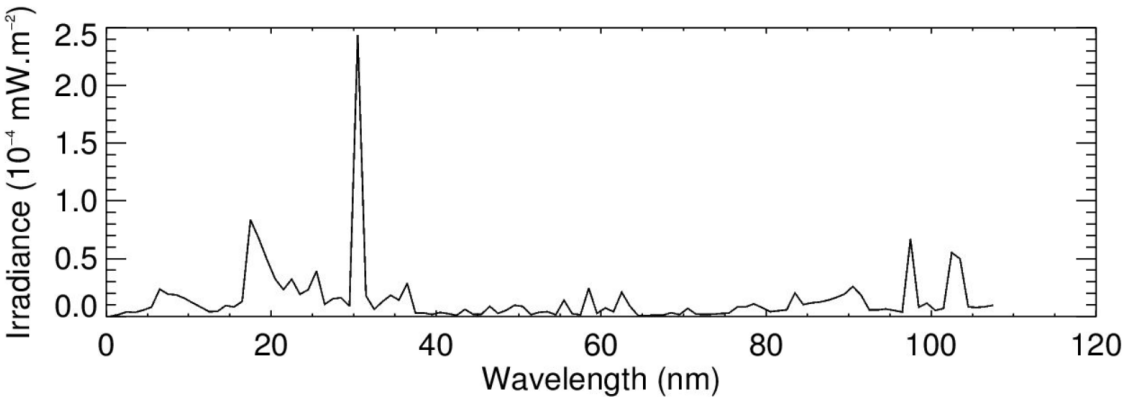


Figure 6.4.1: Spectrum of the effective Solar irradiance for the production by photodissociation of the CO($a^3\Pi$) energy state, responsible for the Cameron airglow. The highest peak is the 30.4 nm He II emission line.

### 6.4.1 Uncorrected data

The peak brightness in Cameron emissions for the uncorrected data was measured 77 times. Figure 6.4.2 shows both the brightness of the Cameron emissions and the Cameron effective irradiance as a function of time. The parameters of the best-fitting model are $a = 40.43$ and $b = 117.48$. The associated R-value is 0.236. This is not a very significant fit. It is presented in Figure 6.4.3.

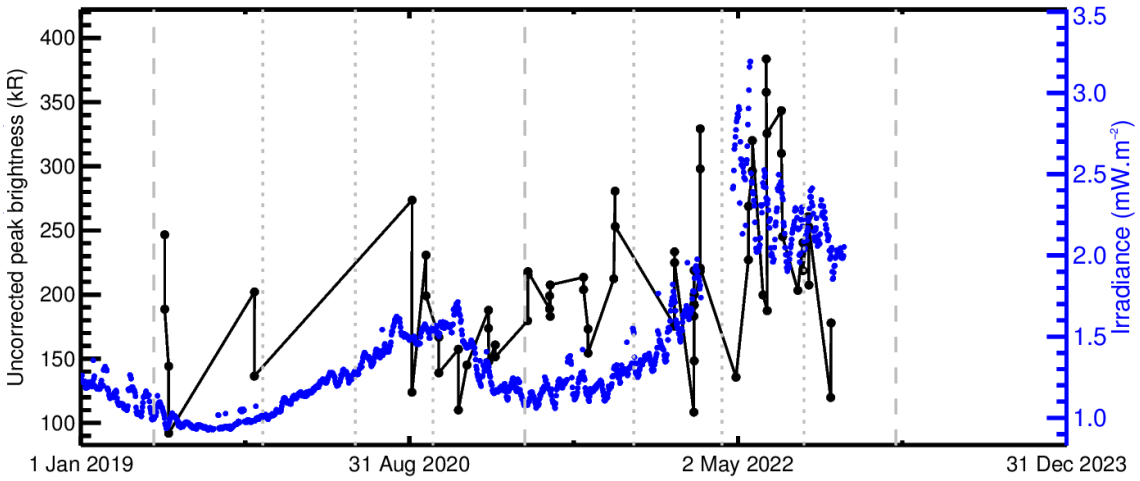


Figure 6.4.2: In black, the uncorrected altitude of the Cameron airglow peak of intensity over time, given in kR. In blue, the Cameron effective irradiance over time, given in mW.m$^{-2}$. Both axes have been scaled and cropped to fit both curves as close as possible in order to present the correlation.

Figure 6.4.4 presents both the uncorrected altitude of the peak in intensity of the Cameron airglow and the Cameron effective irradiance over time.

The best fit for the uncorrected altitude of the peak in intensity of the Cameron airglow as a function of the Cameron effective irradiance has the associated parameters $a = 7.62$ and $b = 109.94$, while the associated R-value of the model is 0.445. We can see in Figure 6.4.5 the fit and the scatter plot of the corrected peak altitude as a function of the Cameron effective irradiance.

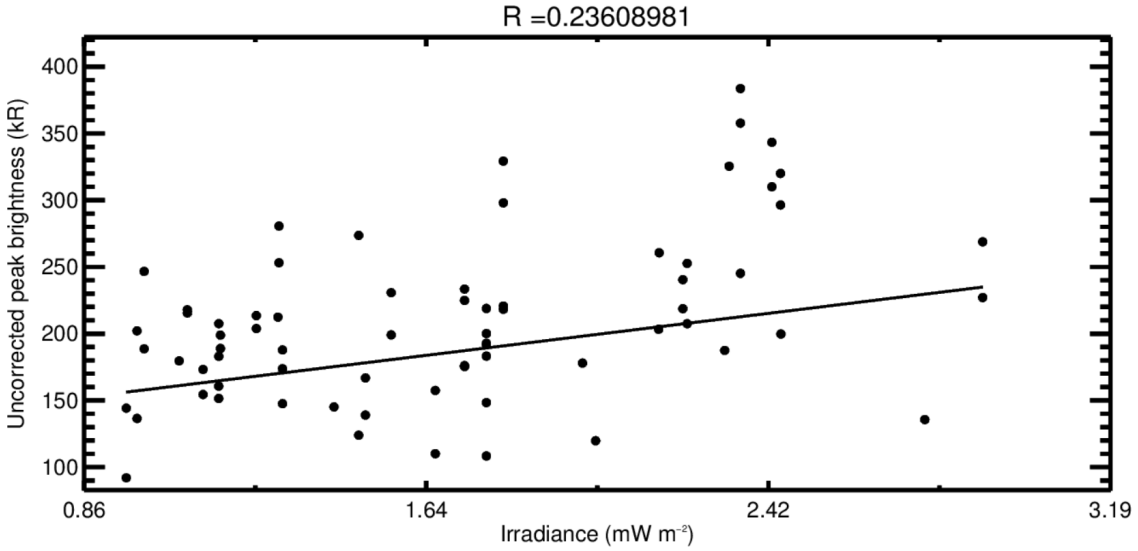


Figure 6.4.3: Black dots represent the corrected peak intensity of the Cameron emission as a function of the irradiance. The black line shows the best fitting linear model for the dataset.

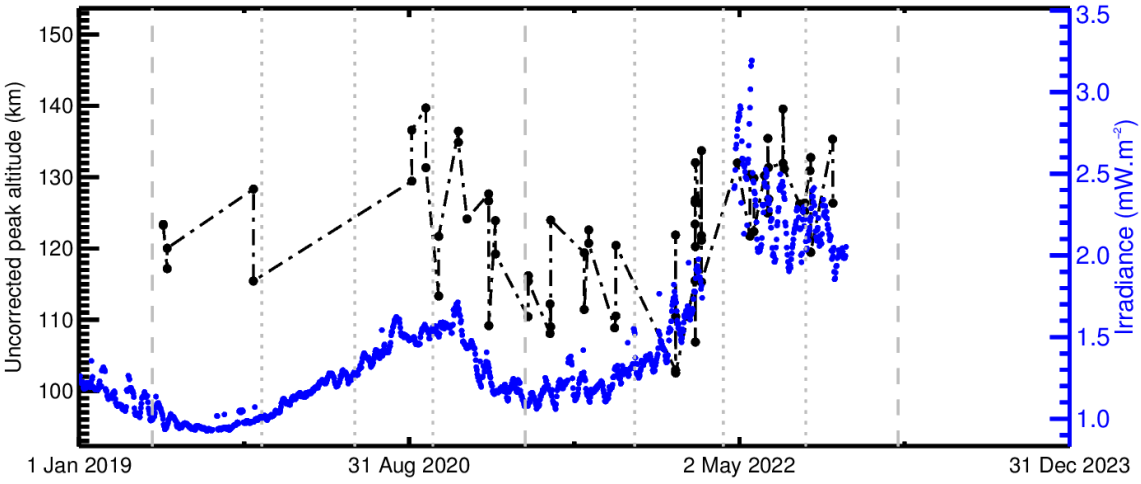


Figure 6.4.4: In black, the uncorrected altitude of the Cameron airglow peak of intensity over time, given in kR. In blue, the Cameron effective irradiance over time, given in $\mathrm{mW.m^{-2}}$. Both axes have been scaled and cropped to fit both curves as close as possible in order to present the correlation.

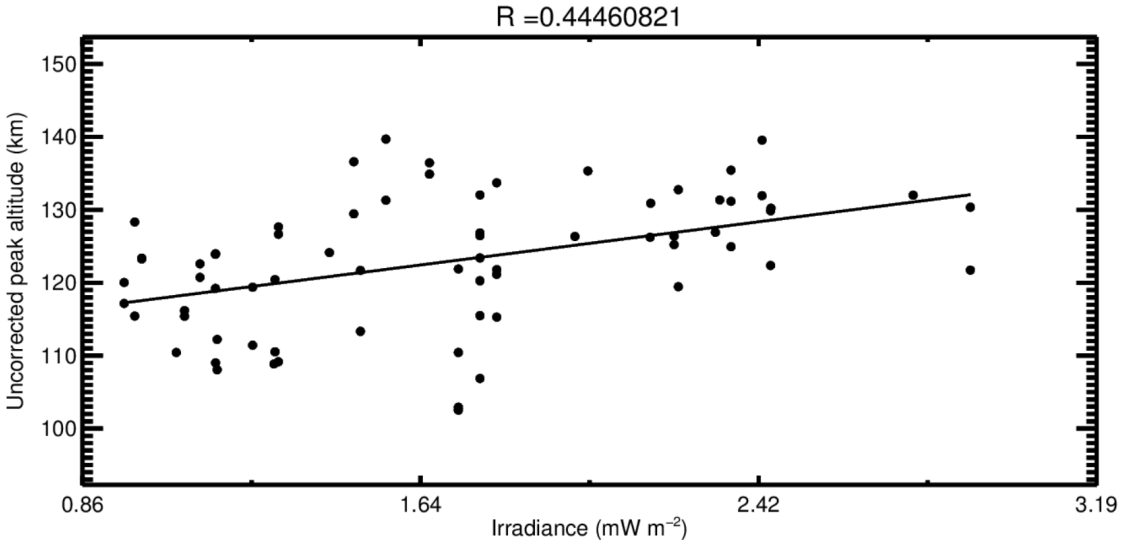


Figure 6.4.5: Black dots represent the uncorrected altitude of the peak intensity of the Cameron emissions as a function of the irradiance. The black line shows the best fitting linear model for the dataset.

### 6.4.2 Corrected data

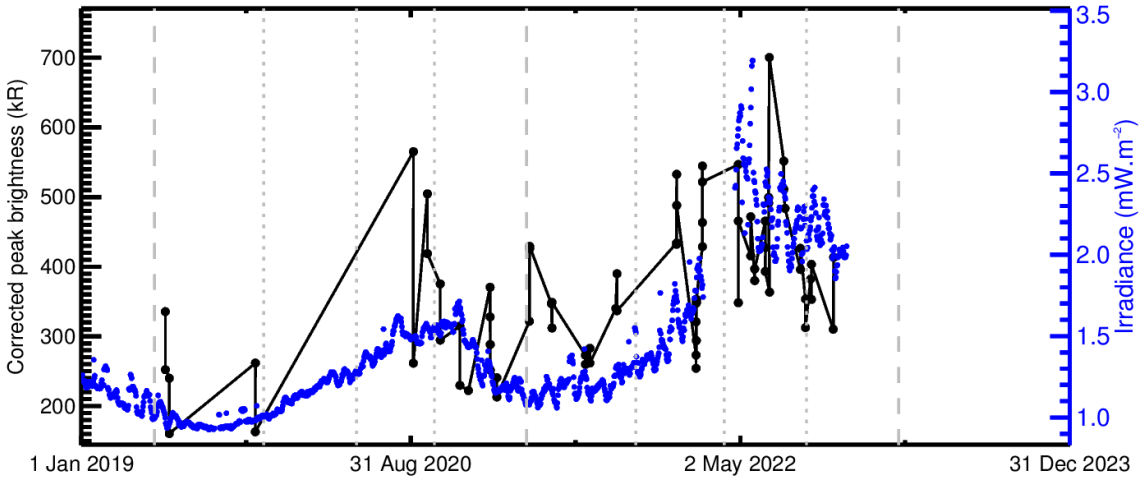


Figure 6.4.6: In black, the corrected altitude of the Cameron airglow peak of intensity over time, given in kR. In blue, the Cameron effective irradiance over time, given in $\mathrm{mW.m^{-2}}$. Both axes have been scaled and cropped to fit both curves as close as possible in order to present the correlation.

The peak of brightness in Cameron emissions for the corrected data was measured 81 times. Figure 6.4.6 shows both the brightness of the Cameron emissions and the Cameron effective irradiance as a function of time. The parameters of the best-fitting model are $a = 129.31$ and $b = 120.30$. The associated R-value is 0.503. This is a vast improvement compared to the model based on uncorrected data. The fit is presented in Figure 6.4.7.

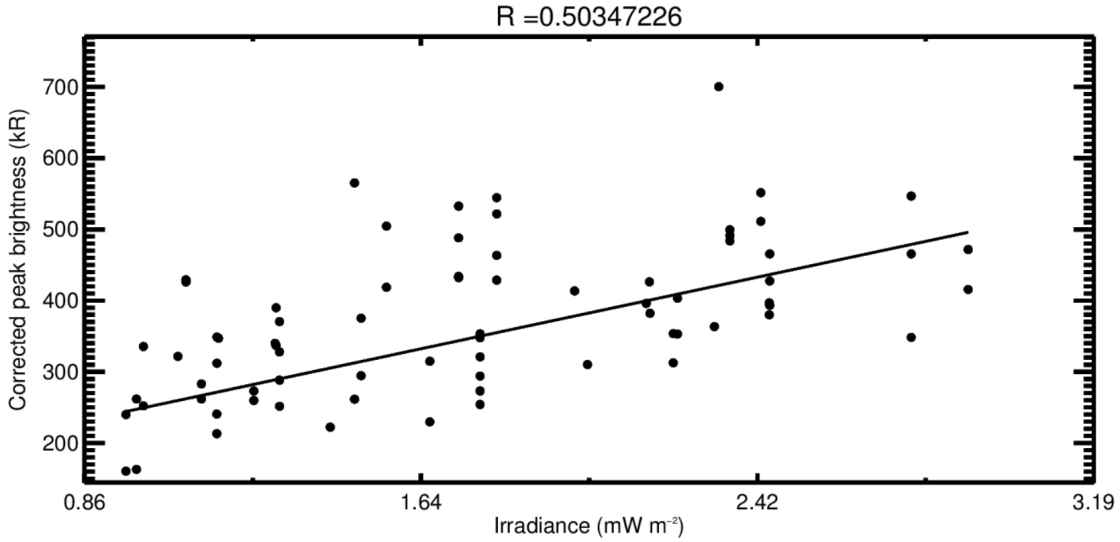


Figure 6.4.7: Black dots represent the corrected peak intensity of the Cameron emission as a function of the irradiance. The black line shows the best fitting linear model for the dataset.

Figure 6.4.8 presents both the corrected altitude of the peak in intensity of the Cameron airglow and the Cameron effective irradiance over time. The best fit for the corrected altitude of the peak in intensity of the Cameron airglow as a function of the Cameron effective irradiance has the associated parameters $a = 7.93$ and $b = 106.86$. The R-value of the model is 0.460. We can see in Figure 6.4.9 the fit and the scatter plot of the corrected peak altitude as a function of the Cameron effective irradiance.

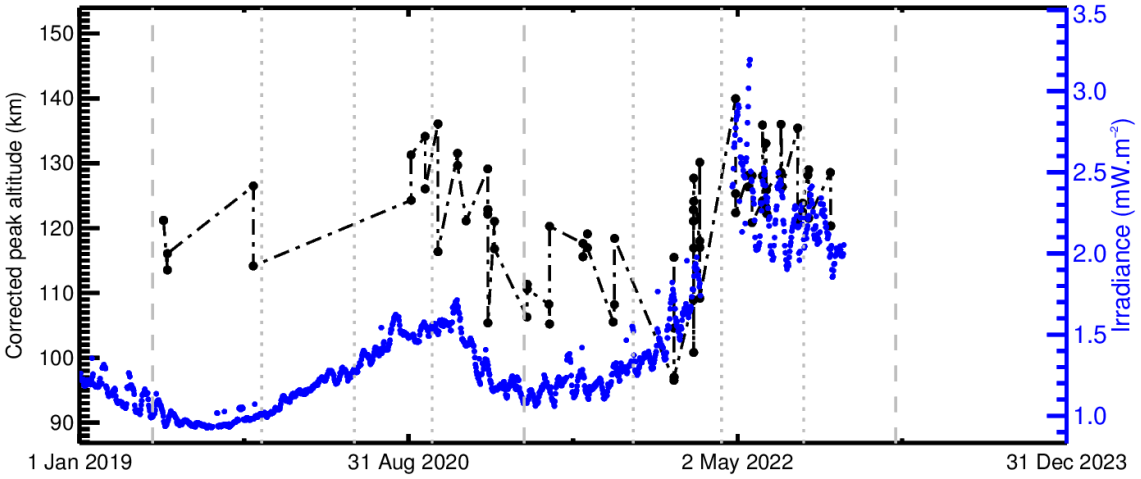


Figure 6.4.8: In black, the corrected altitude of the Cameron airglow peak of intensity over time, given in kR. In blue, the Cameron effective irradiance over time, given in $\mathrm{mW.m^{-2}}$. Both axes have been scaled and cropped to fit both curves as close as possible in order to present the correlation.

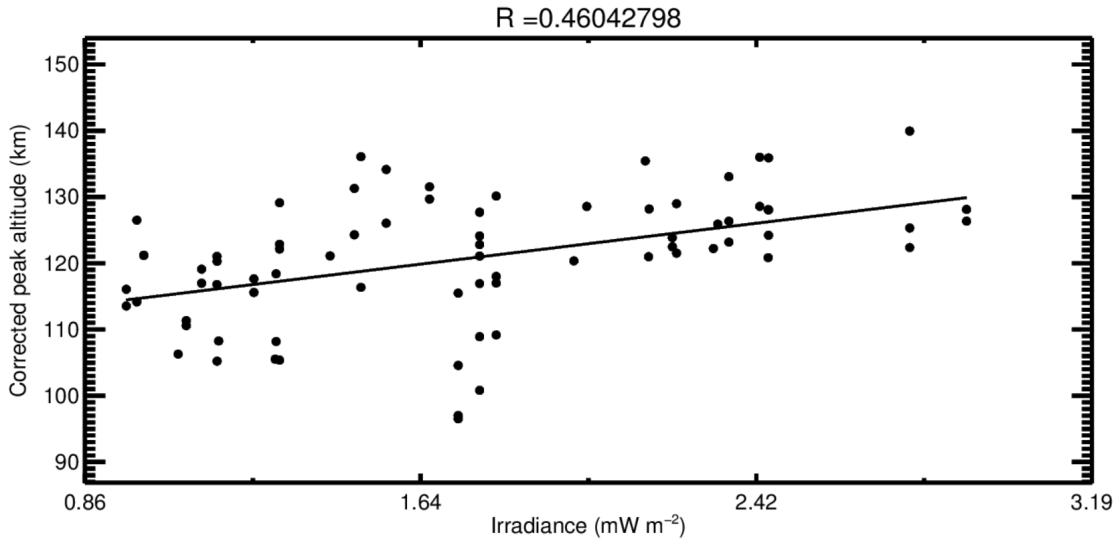


Figure 6.4.9: Black dots represent the corrected altitude of the peak intensity as a function of the irradiance. The black line shows the best fitting linear model for the dataset.

## 6.5 Comparison

Conclusions can be drawn from the results of the different models for the UVD and Cameron emissions, based on both uncorrected and corrected data. Table 6.5.1 and 6.5.2 compile the different model parameters.

First, we can see that the corrected values show better R-values than the uncorrected ones, especially for the intensity fits. The $a$ parameter of the intensity model increase when correcting the value, which is expected as the corrected intensities are always higher than the uncorrected ones. The opposite effect on the $a$ parameter of the altitude model can be seen, as the correction always decreases the altitude. It is interesting to note the high values for the $b$ parameters for the intensity model. We theorize that it is a consequence of the neglected reactions, such as the electrodissociation. Overall, we can conclude that this correction, while not exact, can still find usefulness in the treatment of the values of the intensity and altitude of the peak of brightness in preparation for an analysis of their temporal variation.

Table 6.5.1: Parameters and R-values of the linear models for the peak intensity of the UVD and Cameron emissions.

| Emissions | Uncorrected | | | Corrected | | |
|---|---|---|---|---|---|---|
| | a | b | R | a | b | R |
| UVD | 28.29 | 3.45 | 0.759 | 56.39 | -0.76 | 0.912 |
| Cameron | 41.33 | 116.54 | 0.247 | 129.31 | 120.30 | 0.503 |

Table 6.5.2: Parameters and R-values of the linear models for the peak altitude of the UVD and Cameron emissions.

| Emissions | Uncorrected | | | Corrected | | |
|---|---|---|---|---|---|---|
| | a | b | R | a | b | R |
| UVD | 16.92 | 105.63 | 0.625 | 7.95 | 95.28 | 0.690 |
| Cameron | 7.62 | 109.94 | 0.445 | 7.93 | 106.86 | 0.460 |

## 6.6 Correlation with the reaction rate

Now that we have found a method of correcting the Cameron and UVD data to compensate the effect of the variable SZA, we can look into other variables offering better correlation with our data. From now on, only the corrected values will be used. First, we will study the reaction rate constant.

Let us consider either a photodissociation or photoionisation process :

$$A + h\nu \longrightarrow B + C \tag{6.1}$$

The rate at which the number density of the specie A will vary, can therefore be written as follows :

$$\frac{d[A]}{dt} = -k_p[A] \tag{6.2}$$

The parameter $k_p$ is the reaction rate constant. For a photodissociation or photoionisation, it can be obtained from the following integration :

$$k_p = \int_\lambda Q(\lambda)\sigma(\lambda)F(\lambda)d\lambda \tag{6.3}$$

where Q is the quantum yield of the considered reaction for a reacting photon of wavelength $\lambda$, $\sigma$ is the absorption cross-section of the absorbing molecule and F is the actinic flux, the total incident light intensity, for the wavelength $\lambda$. The latter differs from the irradiance, as the incoming light flux is integrated over all solid angles, instead of a flat surface. They only are equal when the light source is zenithal and at an infinite distance. In the case of the Martian atmosphere, the sun rays can be approximated as parallel, and the irradiance and the actinic flux will therefore be equal for a SZA of 0° [Finlayson-Pitts and Pitts, 2000].

Since the reaction rates are calculated using the flux of photons at the top of the atmosphere, they will not exactly reflect the kinetic of the reaction in the lower atmosphere. We need to consider the depletion of photons as they pass through the atmosphere when choosing the range of wavelengths we will use for our integral. This was already done in the case of the oxygen emissions, as we are studying their lower peaks.

The theoretical correlation between the reaction rate of the photodissociation and the airglow intensity is straightforaward. According to Equation 6.2, the product of $k_p$ with the number density of the specie A gives the amount of molecule of A dissociate per cubic meter per second. From Equation 6.1 we can observe that it also amounts to the number of product create per cubic meter per second, and therefore in turn one photon emission. It should therefore be correlated to the intensity of the peaks.

The case of the oxygen emissions will not produce interesting results, as the effective irradiance is limited to a very short range of wavelengths. We will present them nonetheless for the sack of completion. To determine the reaction rate of O($^1$S) by photodissociation, we used Equation 6.3 and considered only the wavelengths of the Lyman-$\alpha$ irradiance. Using the simple relation between the energy and the wavelength of a photon,

$$E = h.\nu = \frac{h.c}{\lambda},$$

we can convert the EUVM measurements of the energy flux into a photon flux. The cross-section and the quantum yield were obtained from Gkouvelis et al. [Gkouvelis et al., 2018]. The Lyman-$\alpha$ cross-section of the $CO_2$ is $6.536 \times 10^{-24}$ m$^2$ and the quantum yield is 7.5%.

Figure 6.6.1 presents the peak intensity of the 557.7 nm emissions over time, with the reaction rate overlaid. The best fit has the parameters $a = 2.56 \times 10^{11}$ and $b = 0.15$, with a R-value of 0.939. Figure 6.6.2 presents the model and the data.

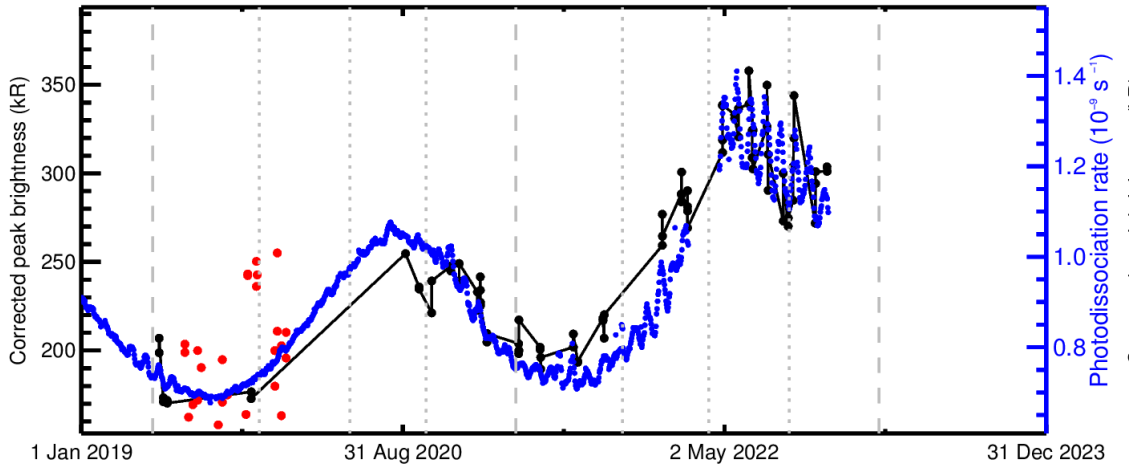


Figure 6.6.1: In black, the corrected peak brightness of the 557.7 nm airglow obtained from the 1024 bin data, given in kR. In red, the corrected peak brightness of the 557.7 nm airglow obtained from the 256 bin data. In blue, the photodissociation rate over time, given in s$^{-1}$. Both axes have been scaled and cropped to fit both curves as close as possible in order to present the correlation.

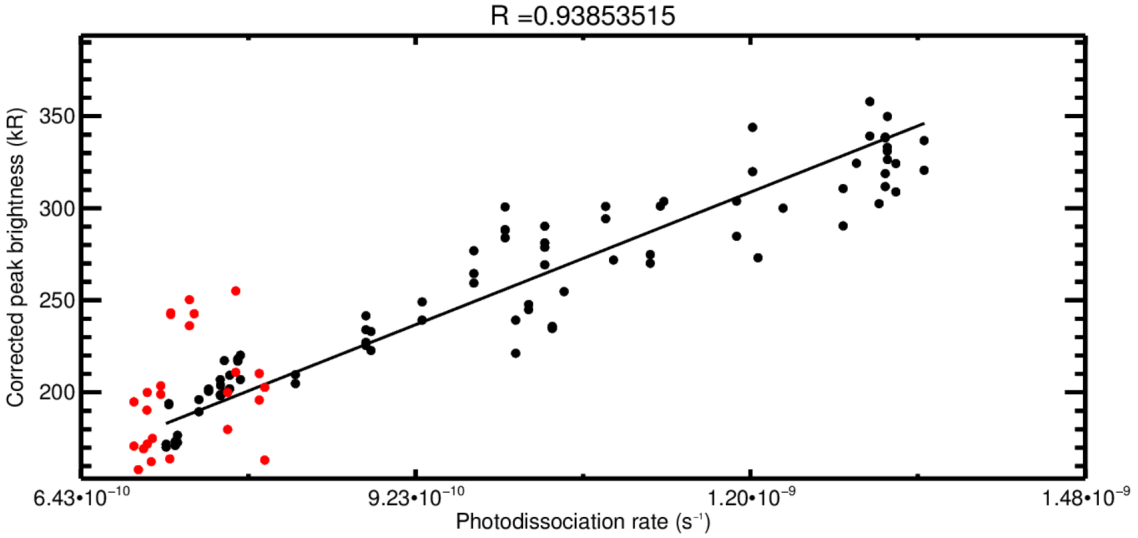


Figure 6.6.2: Black and red dots represent the corrected peak intensity of the 557.7 nm emissions for respectively the 1024 and 256 bin data. The black line shows the best fitting linear model for the 1024 bin dataset.

The 297.2 nm emissions show similar result as the 557.7 nm ones, as is expected. Figure 6.6.3 presents both the 297.2 nm peak intensity and its associated reaction rate overlaid. The best fit has the parameters $a = 1.75 \times 10^{10}$ and $b = -0.62$, with a R-value of R = 0.735. This fit is shown on Figure 6.6.4.

Concerning the UVD emissions, we need to reconsider the photoionisation process responsible for the formation of the $CO_2{}^+(B^2\Sigma)$,

$$CO_2 + h\nu \longrightarrow CO_2{}^+(B^2\Sigma) + e.$$

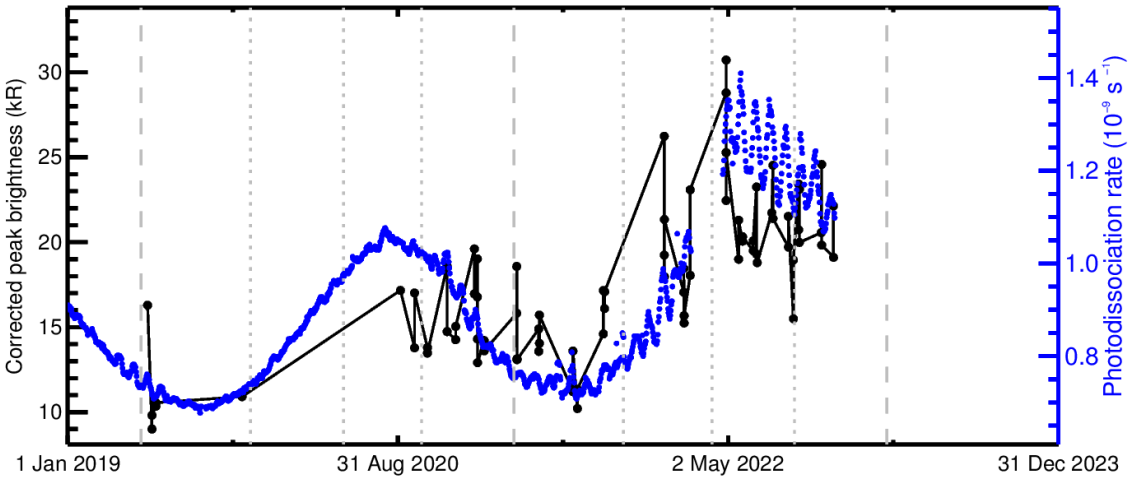


Figure 6.6.3: In black, the corrected peak brightness of the 297.2 nm airglow, given in kR. In blue, the photodissociation rate over time, given in $s^{-1}$. Both axes have been scaled and cropped to fit both curves as close as possible in order to present the correlation.

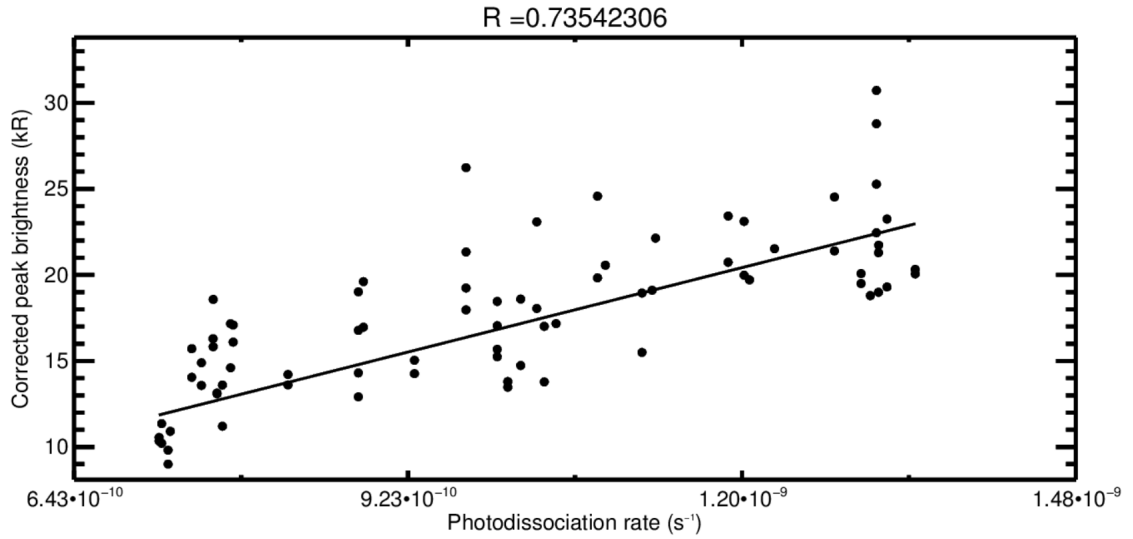


Figure 6.6.4: Black dots represent the corrected peak intensity of the 297.2 nm emissions. The black line shows the best fitting linear model for the dataset.

We can use the same methodology, as the one used for the photodissociation in the oxygen case, replacing the cross-section and quantum yield of the $CO_2$ photodissociation with the corresponding values of the $CO_2$ photoionisation. The cross-section values were described by Gallagher et al. [Gallagher et al., 1988] and the quantum yield by Avakyan et al. [Avakyan et al., 1998]. The resulting contribution of each wavelength to the reaction rate is given in Figure 6.6.5. While the He II 30.4 nm peak remains important, it is interesting to note the variation in the other most contributing wavelengths.

Figure 6.6.6 shows the peak intensity of the UVD emissions, overlaid with the reaction rate for the photoionisation of $CO_2$. The best fit for our dataset has the parameters $a = 1.39 \times 10^9$ and $b = -5.04$, with a R-value of 0.912. The model is presented in Figure 6.6.7 with its dataset. This model has the same R-value as the correlation between the UVD intensity and the UVD effective irradiance, as the reaction rate follows an evolution very similar to the UVD effective irradiance. We can conclude that the reaction rate of the photoionisation of $CO_2$ is not significantly more correlated with the peak intensity than the effective irradiance.

For the Cameron emissions, as for the irradiance case, we will only consider the photodissociation of the $CO_2$ and neglect the other reactions responsible for the production of the $CO(a^3\Pi)$ energy state. The cross-section of the formation of $CO(a^3\Pi)$ by photodissociation of $CO_2$ was

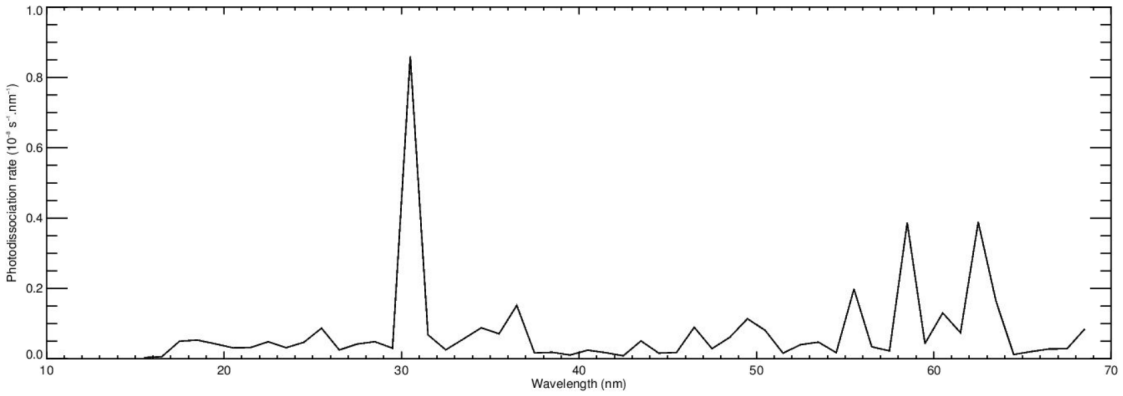


Figure 6.6.5: Reaction rate of the photoionisation, leading to the formation of the $CO_2{}^+(B^2\Sigma)$ energy state. Values are based on the irradiance at the aphelion of MY35.

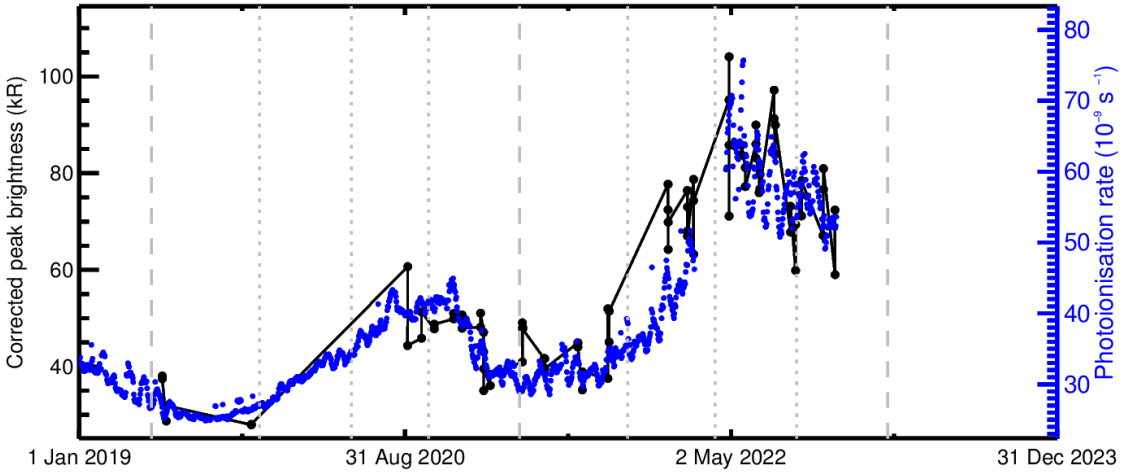


Figure 6.6.6: In black, the peak intensity of the UVD emissions. In blue, the reaction rate of the photoionisation leading to the formation of the $CO_2{}^+(B^2\Sigma)$ energy state.

measured by Lawrence et al. [Lawrence, 1972]. The resulting photodissociation rate is presented in Figure 6.6.8. We can note a peak of reaction rate per wavelength around 90 nm, corresponding to the maximum in the cross-section. We expect a greater change in the R-value than for the case of the UVD from the more drastic difference between the irradiance spectrum and the reaction rate spectrum.

Figure 6.6.9 shows the peak intensity of the Cameron emissions, overlaid with the reaction rate of the $CO(a^3\Pi)$ energy state by photodissociation. The best fit has the parameters $a = 1.52 \times 10^9$ and $b = 55.90$, with an associated R-value of $R = 0.532$. This fit is presented in Figure 6.6.10 with its dataset.

We compiled the values of the parameters of the models for the irradiance and the reaction rate in Table 6.6.1. We can conclude that the usage of the reaction rate for the correlation of the peak intensity does not offer significantly better results than the effective irradiance, with the single slight exception of the Cameron band. Both the oxygen and the UVD emissions originate mostly from one peak of irradiance, respectively the Lyman-$\alpha$ and the He II 30.4 nm lines. The temporal variation of the effective irradiance and reaction rate will therefore closely follow the variations of the intensity of the corresponding solar lines. The case of the Cameron is more interesting, as Figures 6.4.1 and 6.6.8 show that the most intense wavelengths in the effective irradiance of the Cameron emissions are not the ones responsible for most of the photodissociation.

The method of drawing the reaction rate per wavelength might be the most useful results from this analysis. It allows the reader to compare at a glance the relative importance of the different wavelengths in the solar spectrum in the production of the airglow.

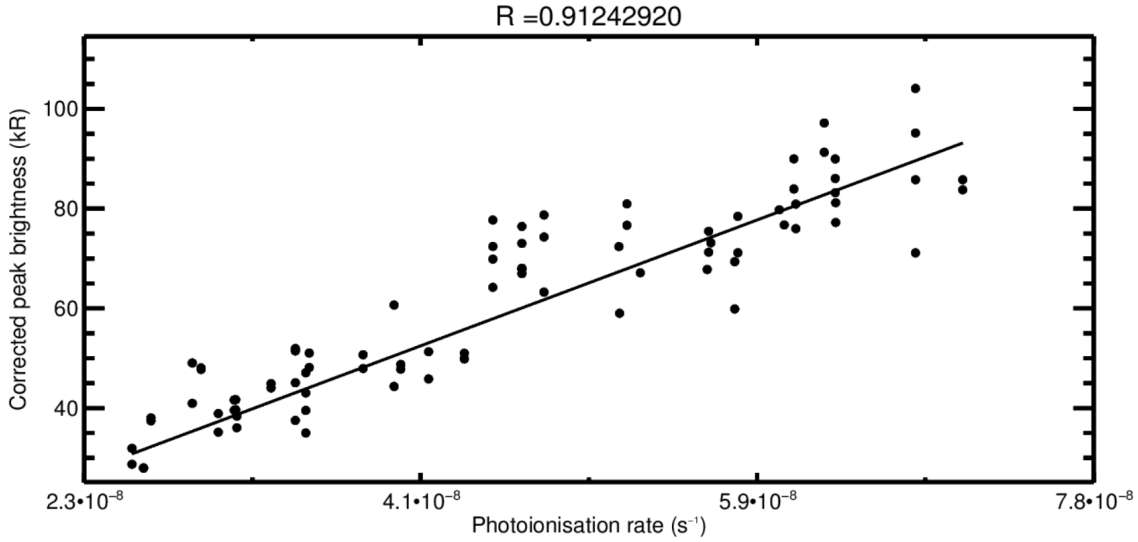


Figure 6.6.7: The dots are the intensity of the UVD emission, given as a function of the reaction rate. The black line shows the best fitting linear model for the dataset.

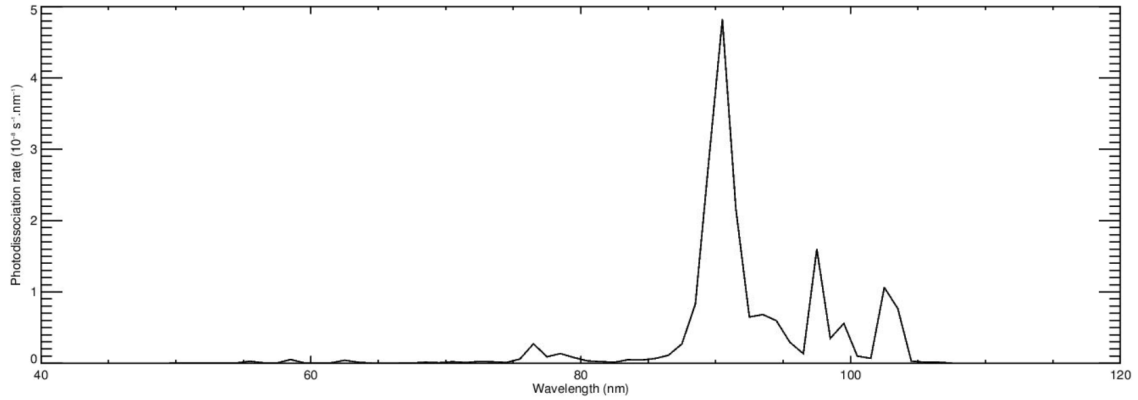


Figure 6.6.8: Reaction rate of the photodissociation, leading to the formation of the CO($a^3\Pi$) energy state. Data are based on the irradiance at the aphelion of MY35.

Table 6.6.1: Parameters and R-values of the linear models for the correlation of the peak intensity with the effective irradiance and the reaction rate constant.

| Emissions | Irradiance | | | Reaction rate | | |
|---|---|---|---|---|---|---|
| | a | b | R | a | b | R |
| 557.7 nm | 77.69 | 0.01 | 0.939 | $2.56 \times 10^{11}$ | 0.15 | 0.939 |
| 297.2 nm | 5.30 | -0.63 | 0.735 | $1.75 \times 10^{10}$ | -0.62 | 0.735 |
| UVD | 56.39 | -0.76 | 0.912 | $1.39 \times 10^{9}$ | -5.04 | 0.912 |
| Cameron | 129.31 | 120.30 | 0.503 | $1.52 \times 10^{9}$ | 55.60 | 0.532 |

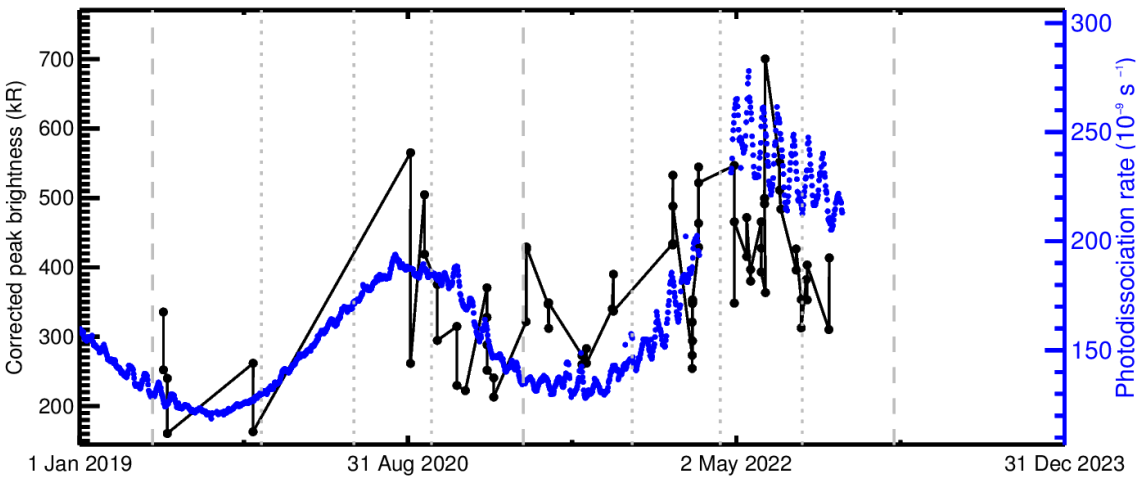


Figure 6.6.9: In black, the peak intensity of the Cameron emissions. In blue, the reaction rate of the photodissociation leading to the formation of the CO($a^3\Pi$) energy state.

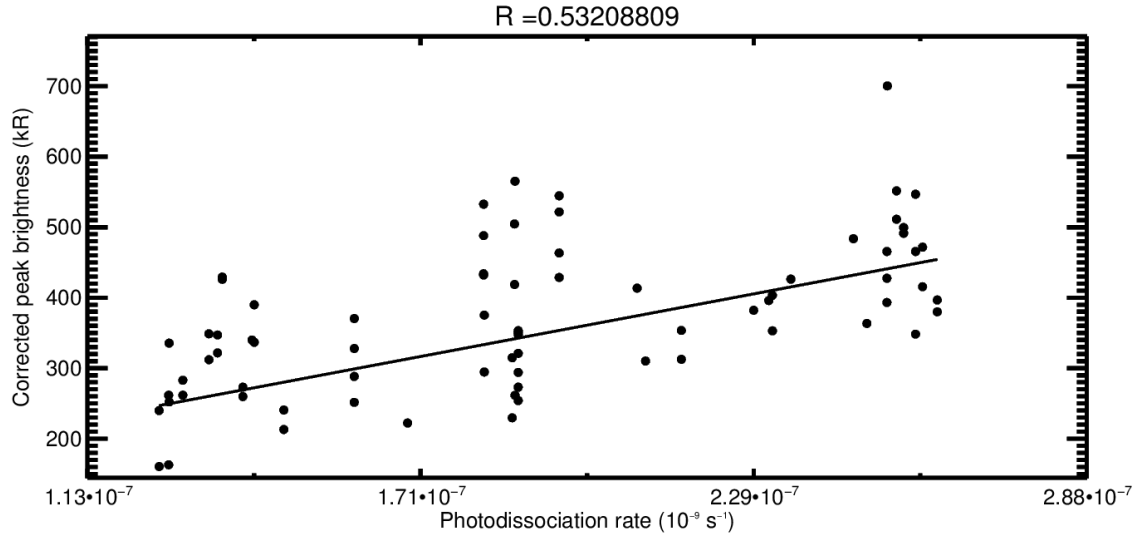


Figure 6.6.10: The dots are the intensity of the Cameron emission, given as a function of the reaction rate. The black line shows the best fitting linear model for the dataset.

## 6.7 Correlation with the orbital radial distance

We have so far correlated the peak altitude of the emissions with the irradiance. The most common pairing in the scientific literature when analysing the time variation of the altitude is with the Lyman-$\alpha$ [Soret et al., 2022] or the F10.7[Cox et al., 2010]. This is due in part to a lack of measurement of the solar irradiance spectrum from Mars orbit until recently. We disagree with this method, as the main variable controlling the altitude of the airglow is the $CO_2$ column density, which varies vastly from one season to the other with the polar caps cycle and the general expansion of the atmosphere. We therefore decided to correlate our altitude measurements with the inverse of the square of the orbital radius, hereafter simply refer as $R^{-2}$.

The values were calculated from the Kepler elliptical orbit formula using an eclipticity e = 0.09339 and normalising the semi-major axis, setting a = 1. The resulting radii are therefore given as multiple of the semi-major axis. This choice of unit is for simplicity, as we are only interested in the variation and relative values of the radius over time.

The peak intensities of the 557.7 nm airglow are given in Figure 6.7.1, overlaid with the values of $R^{-2}$. The missing section of the $R^{-2}$ curve corresponds to periods were the EUVM measurements were interrupted. We rejected data point in those time periods in order to use the same dataset as the previous analyses. We can see a clearer correlation, especially for the amplitude of the variation

on both year. The best fit has the parameters $a = 36.78$ and $b = 44.38$, with the associated R-value of 0.830. The model is shown in Figure 6.7.2.

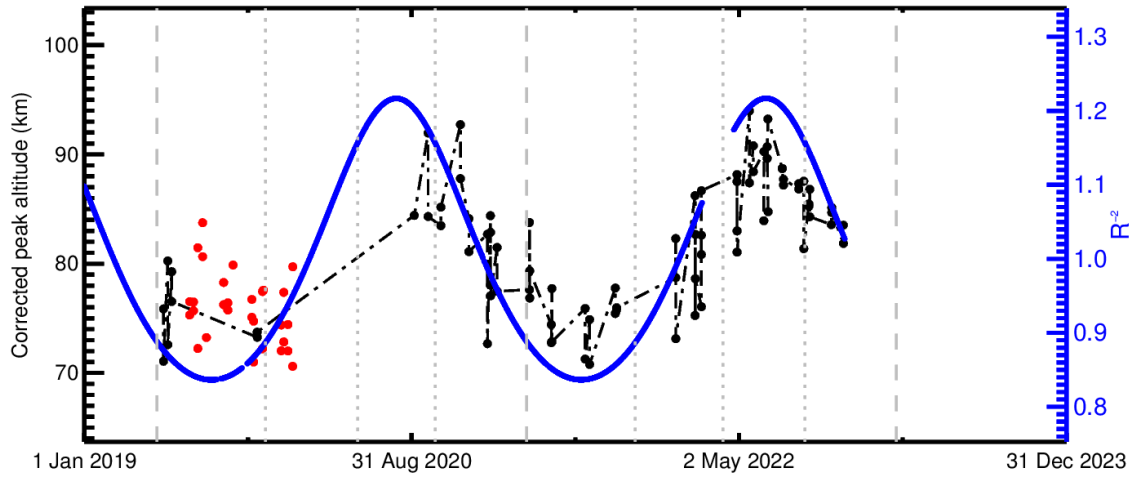


Figure 6.7.1: In black, the altitude of the peak of the 557.7 nm emissions. In blue, the inverse of the square of the orbital radius.

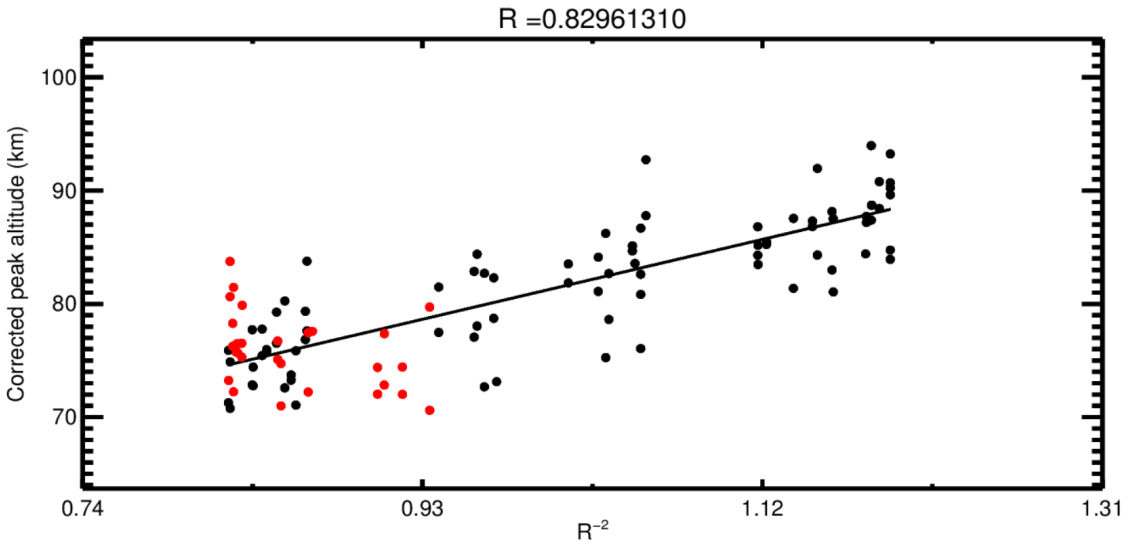


Figure 6.7.2: The dots are the intensity of the 557.7 nm emission, given as a function of the inverse of the square of the orbital radius. The black line shows the best fitting linear model for the dataset.

The peak altitude of the 297.2 nm airglow are given in Figure 6.7.3, overlaid with the values of $R^{-2}$. The best fit has the parameters $a = 37.28$ and $b = 44.36$, with the associated R-value of 0.760. The fit is shown in Figure 6.7.4.

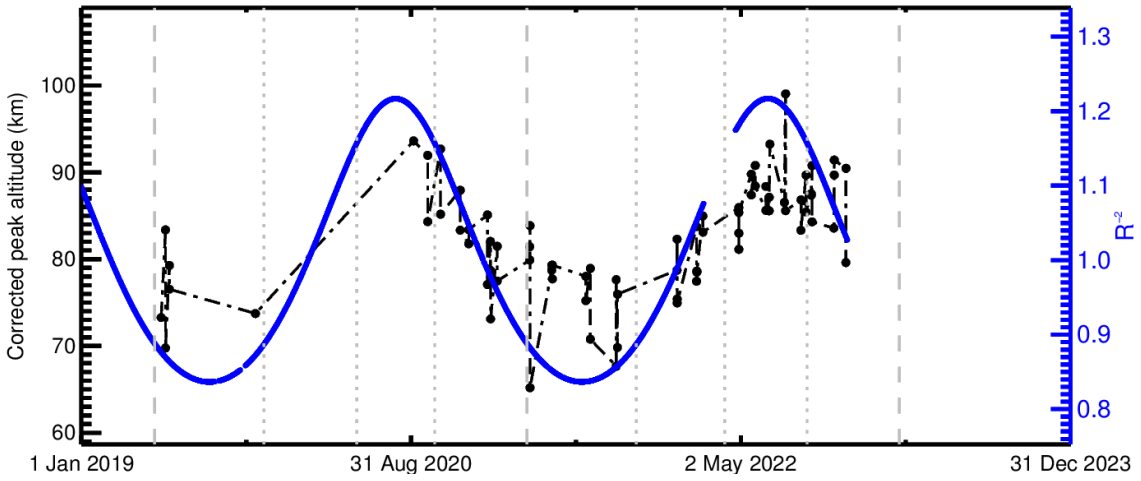


Figure 6.7.3: In black, the altitude of the peak of the 297.2 nm emissions. In blue, the inverse of the square of the orbital radius.

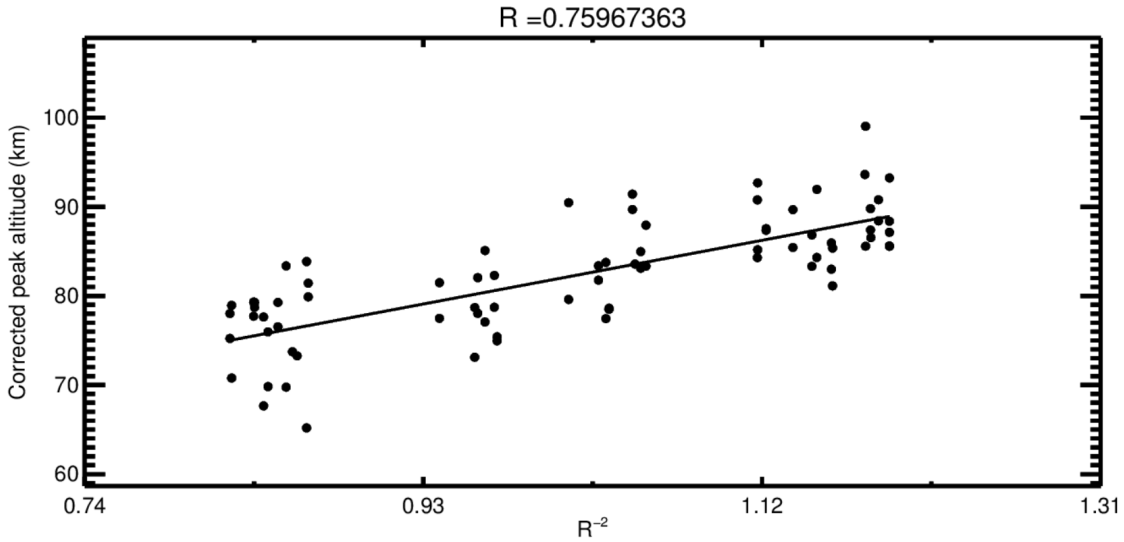


Figure 6.7.4: The dots are the intensity of the 297.2 nm emission, given as a function of the inverse of the square of the orbital radius. The black line shows the best fitting linear model for the dataset.

The peak intensity of the UVD airglow are given in Figure 6.7.5, overlaid with the values of $R^{-2}$. The best fit has the parameters $a = 46.11$ and $b = 73.63$, with the associated R-value of 0.740. The fit is shown in Figure 6.7.6.

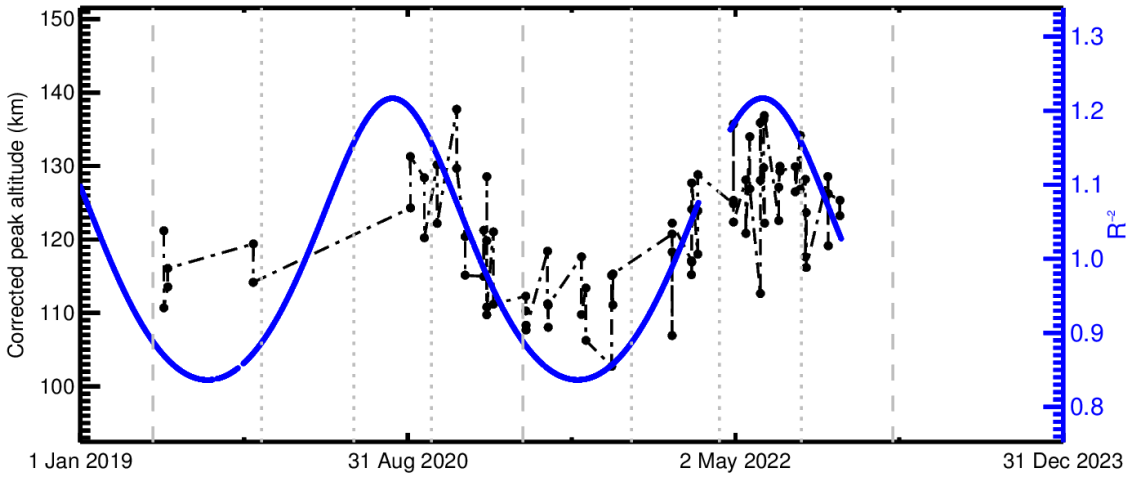


Figure 6.7.5: In black, the altitude of the peak in UVD emissions. In blue, the inverse of the square of the orbital radius.

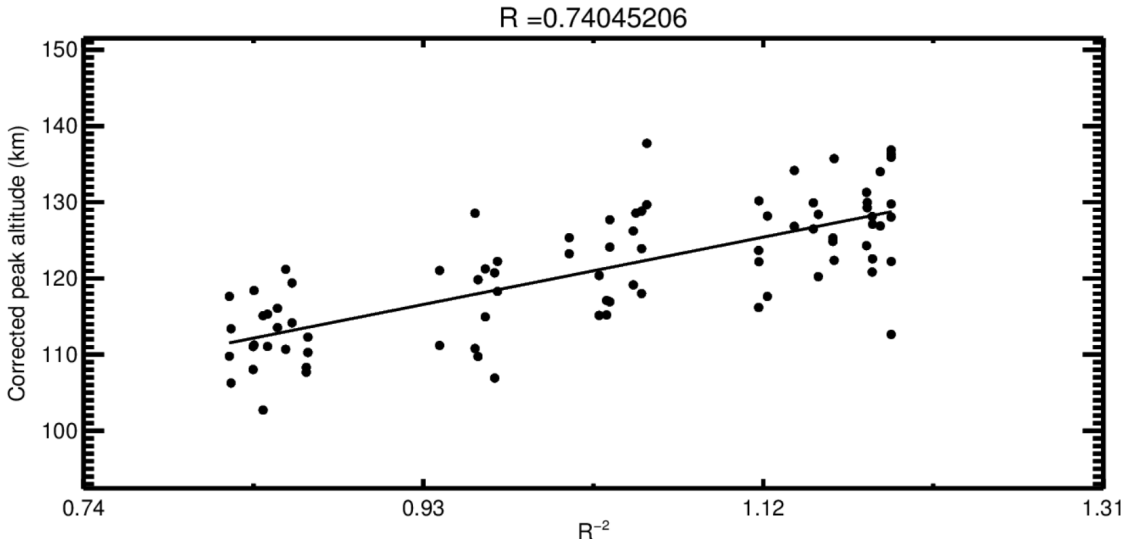


Figure 6.7.6: The dots are the intensity of the UVD emission, given as a function of the inverse of the square of the orbital radius. The black line shows the best fitting linear model for the dataset.

The peak intensity of the Cameron airglow are given in Figure 6.7.7, overlaid with the values of $R^{-2}$. The best fit has the parameters $a = 42.23$ and $b = 77.20$, with the associated R-value of 0.594. The fit is shown in Figure 6.7.8.

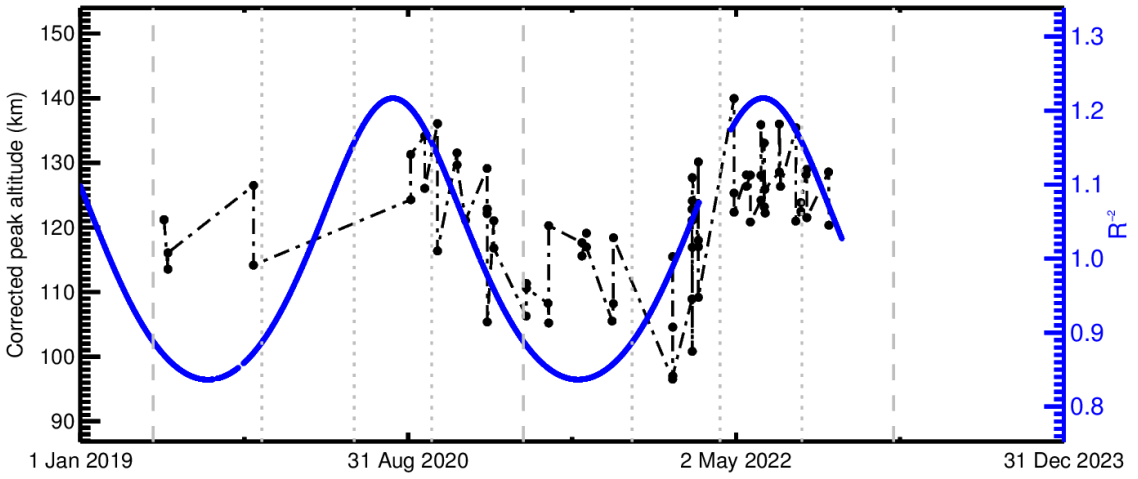


Figure 6.7.7: In black, the altitude of the peak in Cameron emissions. In blue, the inverse of the square of the orbital radius.

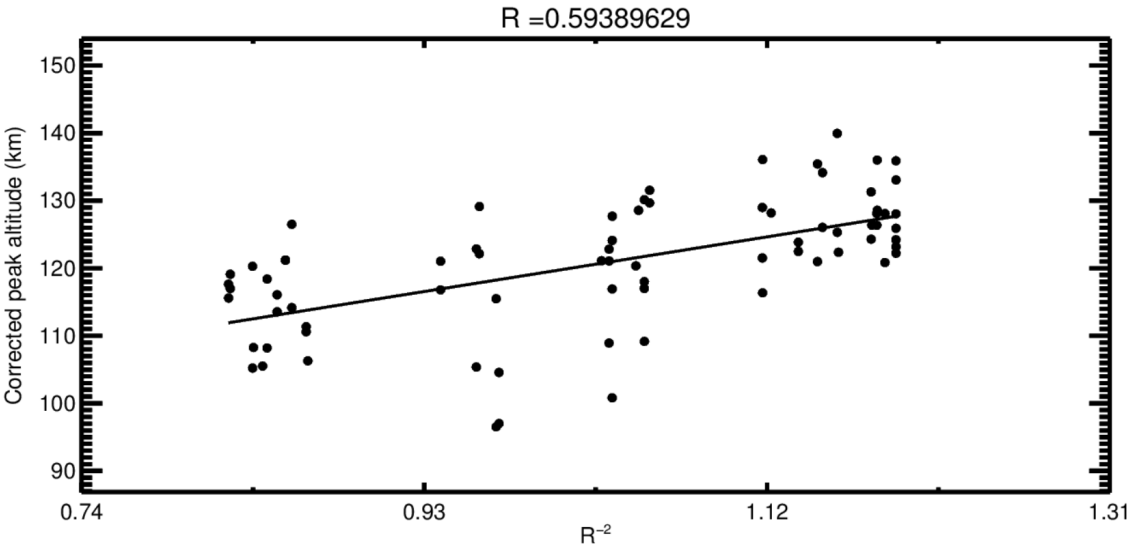


Figure 6.7.8: The dots are the intensity of the Cameron emission, given as a function of the inverse of the square of the orbital radius. The black line shows the best fitting linear model for the dataset.

We have compiled in Table 6.7.1 those results, as well as the parameters of the models for the corrected altitude found previously. Contrary to the case of the reaction rate, this new quantity seems to offer better correlation results than the effective irradiance. The R-values are higher for all emissions. As expected, the $a$ parameter remains similar for the 557.7 nm and 297.2 nm emissions. While, $b$ already had similar values for the UVD and the Cameron emissions, we can see that they now also share similar values of $a$. This indicates a shared seasonal behaviour. Further studies crossing the altitude with data on the column density of $CO_2$ could offer more insights on this seasonal behaviour.

Table 6.7.1: Parameters and R-values of the linear models for the correlation of the peak altitude with the effective irradiance and the inverse of the square of the orbital radial distance.

| Emissions | Irradiance | | | $R^{-2}$ | | |
|---|---|---|---|---|---|---|
| | a | b | R | a | b | R |
| 557.7 nm | 6.59 | 60.02 | 0797 | 36.78 | 44.38 | 0.830 |
| 297.2 nm | 6.43 | 61.03 | 0.700 | 37.28 | 44.36 | 0.760 |
| UVD | 15.55 | 104.58 | 0.627 | 46.11 | 73.63 | 0.740 |
| Cameron | 7.93 | 106.86 | 0.460 | 42.23 | 77.21 | 0.594 |

## 6.8 Impact of the SZA on the R-values

Cox et al. previously observed a variation of the parameters of the linear model for the correlation of the Cameron and UVD airglow intensity and the irradiance based on the SZA [Cox et al., 2010]. We will determine if such a variation is also present for the 557.7 nm airglow. We decided to further subdivide the dataset based on the SZA. As the value of the SZA of the measured peaks varies between 34.2 and 66.5°, we created three subsets of 13.3° in order to cover a range of values from 30 to 70°.

Figure 6.8.1 presents the resulting fit plots for the modeling of the peak intensity and altitude in each SZA bin. Table 6.8.1 presents the resulting parameters for the best fit, as well as the R-value associated. We can observe an increase of the $a$ parameter with the SZA. This behaviour is similar to the observation made by Cox et al. (2010) for the Cameron and UVD emissions.

Concerning the R-values of the different fits, we can observe that they decrease with increasing SZA. We can therefore speculate that the linearity of the correlation breaks for larger values of SZA. This is far from surprising, as larger SZA imply a thicker optical depth on the path of light. Our irradiance data are taken from orbit and do not reflect the effect of the atmosphere on the light prior to the observed layer. This discrepancy in irradiance leads to decreasing a parameter and less-linearity for the intensity model as SZA increases.

Table 6.8.1: Parameters and R-values of the linear models for the different SZA ranges.

| SZA range | Intensity | | | Altitude | | |
|---|---|---|---|---|---|---|
| | a | b | R | a | b | R |
| 30 : 43.3 | 73.55 | 4.22 | 0.981 | 88.27 | -6.39 | 0.948 |
| 43.3 : 56.6 | 83.19 | -10.46 | 0.949 | 73.34 | 7.82 | 0.875 |
| 56.6 : 70 | 57.37 | 57.25 | 0.907 | 66.49 | 15.10 | 0.704 |

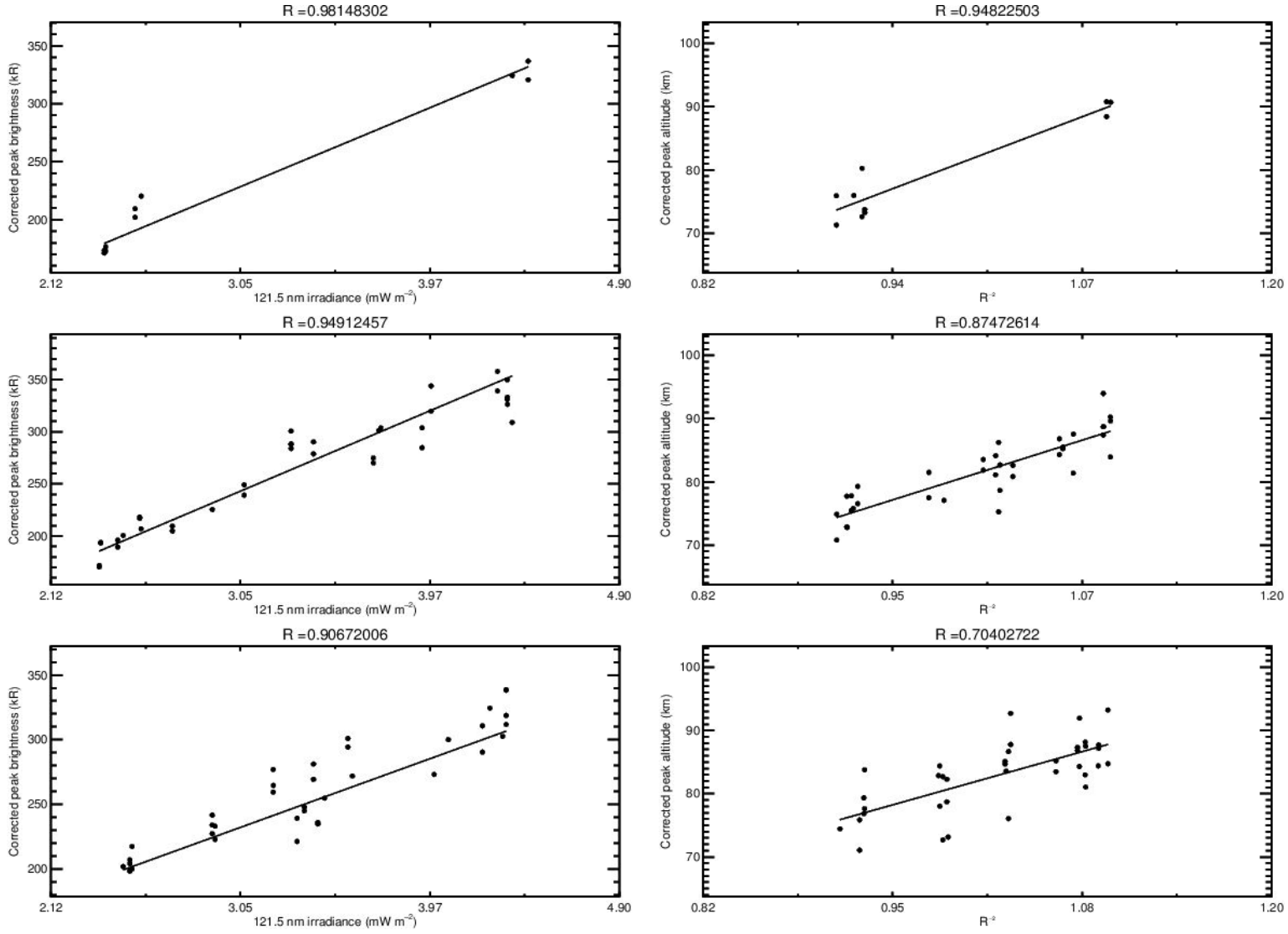


Figure 6.8.1: On the left side, the corrected peak intensity of the 557.7 nm airglow as a function of the Lyman $\alpha$ irradiance. On the right side, the corrected altitude of the peak of intensity of the 557.7 nm airglow as a function of the Lyman $\alpha$ irradiance. In both case, the lines are the best fitting linear model for the data. Each row of figures is associated to different ranges of SZA values, respectively from top to bottom, 30 to 43.3°, 43.3 to 56.6° and 56.6 to 70°.

## 6.9 Impact of the Solar activity

The 25th solar cycle began in late 2019 and the solar activity as been continuously increasing since then. We can identify, from the plots of the irradiance superposed on the peak intensity, that the mean intensity has followed a similar trend. To simplify the identification of this tendency, we used the linear models found previously to dampen the effect of the ellipticity of the orbit. We can determine the irradiance at a reference distance from the Sun by multiplying the measure irradiance by the square of the orbital radius, where the latter is express as a multiple of a reference distance. This reference distance will once again be the semi-major axis of the Martian orbit.

From the linear model of the brightness of the airglow, we have the following expression of the brightness (B) as a function of the irradiance (I) :

$$B = a \times I + b$$

We can therefore substitute the measured irradiance by the irradiance at the semi-major axis and find what would have been the most likely brightness at that point :

$$B' = a \times (I \times R^2) + b$$

The resulting brightness were drawn on Figures 6.9.1 to 6.9.4, with the respective effective irradiance at the semi-major axis. As the brightness values were obtained from the linear model, they cannot be used to measure any correlation. The figures are only given to illustrate the impact of the solar activity on the irradiance and the influence of the solar cycle on the airglow brightness. It is interesting to note the 27-day cyclic pattern occurring in the irradiance, a result of the rotation of the Sun.

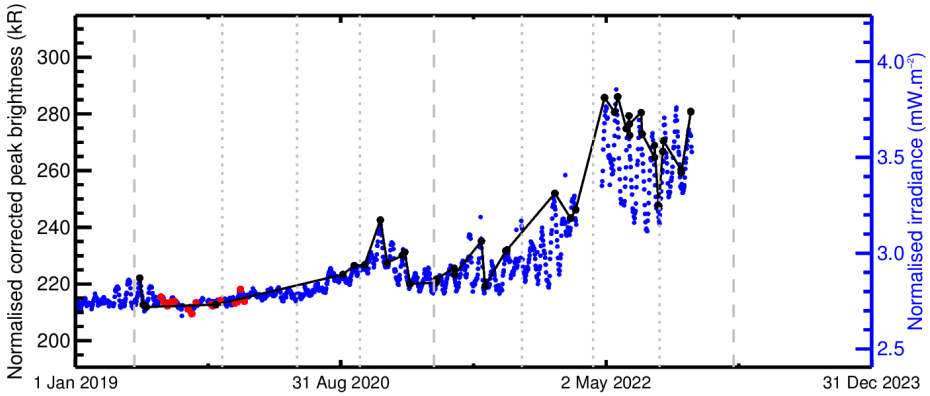


Figure 6.9.1: (a)

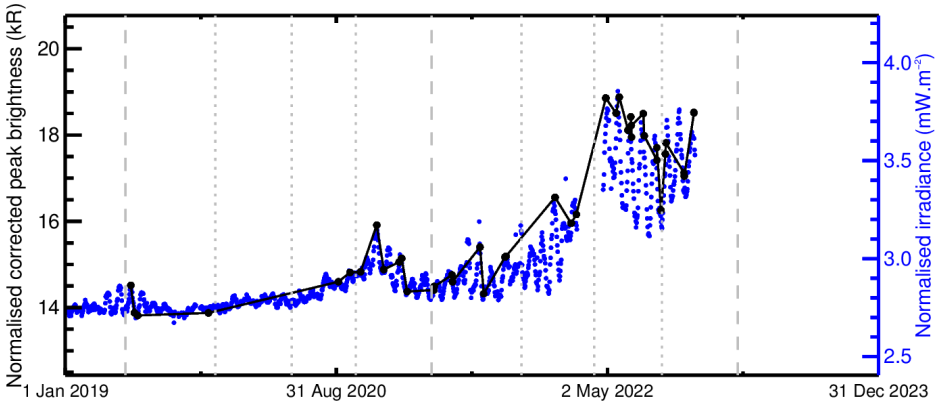


Figure 6.9.2: (b)

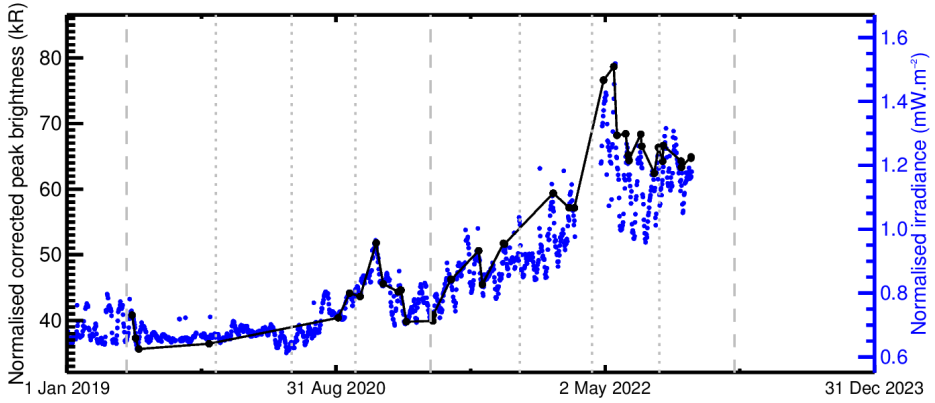


Figure 6.9.3: (c)

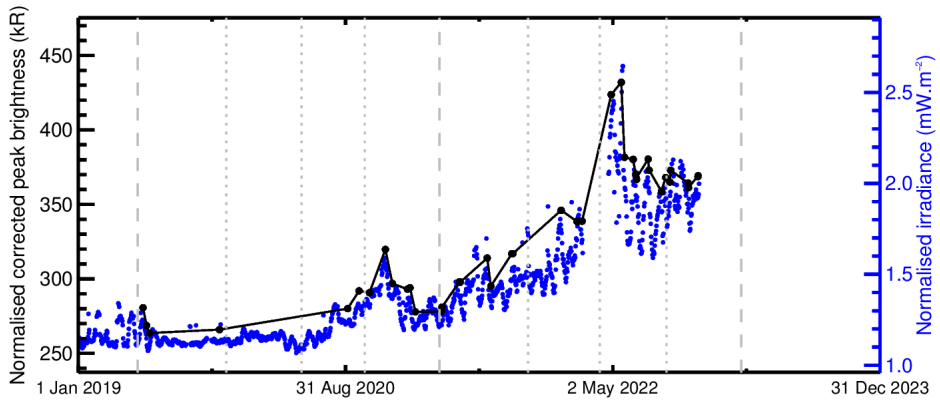


Figure 6.9.4: (d)

In black, the corrected peak intensities of the 557.7 nm (a), 297.2 nm (b), UVD (c) and Cameron (d) emissions, with their respective effective irradiances in blue. In red are given the 557.7 nm peak intensity associated to the 256-bin dataset. All quantities have been normalised to a reference distance to the Sun equal to the semi-major axis of the Martian orbit. The 27-days cycle of the irradiance is a consequence of the rotation of the Sun.

# 7. Conclusion

Airglows offer a unique opportunity to remotely study the upper atmosphere of Mars. The analysis of the intensity of these emissions and their variations through space and time may serve as proxy for the measurement of other quantities. It can also be used to deepen our understanding of the Martian atmosphere and the interactions existing between numerous atmospheric phenomena. From the history of the research on the topic, we may infer that the key to this knowledge lies in a combination of remote sensing, climate model and laboratory measurements.

### Limb profiles

We have demonstrated through this work that a simple combination of data and statistical analysis can prove insightful. Through analysis of UVIS data, we produced limb profiles for the green, UV, and red line emissions of atomic oxygen, the UVD and FDB emissions of $CO_2{}^+$ and the Cameron emissions of CO. Our study covers two Martian orbits, dividing the data in a total of 8 time periods. We observed the seasonal and annual variations of the limb profiles. The general trend was an increase of the intensity as we progress in the current solar cycle and the solar irradiance increases. No significant variation of the altitude from one orbit to the other hinted at an independence of the altitude with the irradiance itself. It rather seems correlated with the orbital radius. Furthermore, we were able to reproduce the observed seasonal variation of the 557.7 nm airglow in a photochemical model.

### Correlation with the effective irradiance

We determined the effective irradiance associated with each production process and correlated it with the peak intensity through time. We observed the correlation over two complete Martian orbits and reproduced previous results found in the scientific literature. Notably, we improved the statistical significance of the previous linear fit for the 557.7 nm airglow found in Soret et al. [Soret et al., 2022]. Moreover, we analysed using the same methodology the 297.2 nm oxygen line, the UVD and the Cameron bands airglows.

### Correction of the SZA effect

We analysed the validity of the Chapman layer theory in cases of a polychromatic light absorption. In particular, we found out that the correction developed based on this theory for the altitude of the peak of emission of the airglow could be applied to UVD and Cameron emissions and yield higher correlations. This possibility of correcting the effect of the variable SZA will surely prove itself useful for further studies of the variation of the UVD and Cameron airglow. We hope for a continuation of research on the topic.

### Correlation with the reaction rate

We studied the correlation of the intensity of the peak of emission with the reaction rate of the main reaction of formation of the emitter of the airglow. While it did not improve significantly our correlations, the study of the reaction rate per wavelength proved insightful in the determination of the most important part of the solar spectrum in the production of the different airglow emissions. It allowed us to identify the 30.4 nm He II line in the solar spectrum as the principal source of energy for the UVD airglow.

### Correlation with the orbital radius

The correlation of the altitude of the peak of emission with the inverse of the square of the orbital radius showed significant improvement over the correlation with the effective irradiance. We found a common variation of the altitude, independent of the irradiance and of the type of emissions. Gkouvelis et al. [Gkouvelis et al., 2018] describe how the airglow peak altitude is primarily controlled by the overlying $CO_2$ column density. The correlation we observed is therefore a clear consequence of the inflation of the atmosphere during the perihelion.

### Effect of the SZA of the linear fits

We measured the effect of the SZA on the parameters and statistical significance of our 557.7 nm models. By dividing our sample into 3 different ranges of SZA, we observed that the linear model worked better for smaller SZA. Furthermore, we observed a clear variation of the parameter of the best fit for the different ranges of SZA. Both results mirror observations made by Cox et al. [Cox et al., 2010] concerning the Cameron airglows.

### Follow-up research possibilities

This work opens the door to multiple follow-up studies. Due to the low precision in the measurement of the FDB intensity, we were not able to study the seasonal variation of these emissions, but we expect this could be made with a longer period of observation. Data from the next generation of orbiters will probably be needed before the same analysis can be made for the red emission of the oxygen. Further studies of the UVD, Cameron and FDB airglow using the correction by Gkouvelis et al. will likely be insightful. We think that an analysis of the correlation between the 557.7 nm airglow and the 27-days Sun cycle would provide much information on the short-term variation in the Martian atmosphere. The capacity of the current version of MCD to model the seasonal variation of the thermal structure of the atmosphere is a limiting factor for photochemical models. A scaling factor to the $CO_2$ column density is needed in order to obtain realistic values. A combination of observations and photochemical modelling could therefore lead to improvement of climate models. All in all, further researches on the Martian airglow may prove to be key factors in our understanding of the vertical structure and time variation of the atmosphere of Mars.

# Bibliography


[Allison and McEwen, 2000] Allison, M. and McEwen, M. (2000). A post-pathfinder evaluation of areocentric solar coordinates with improved timing recipes for mars seasonal/diurnal climate studies. *Planetary and Space Science*, 48(2-3):215–235.

[Ångström, 1868] Ångström, A. J. (1868). *Recherches sur le spectre solaire*. Schultz.

[Aoki et al., 2022] Aoki, S., Gkouvelis, L., Gérard, J.-C., Soret, L., Hubert, B., Lopez-Valverde, M., González-Galindo, F., Sagawa, H., Thomas, I., Ristic, B., et al. (2022). Density and temperature of the upper mesosphere and lower thermosphere of Mars retrieved from the OI 557.7 nm dayglow measured by TGO/NOMAD. *Journal of Geophysical Research: Planets*, 127(6):e2022JE007206.

[Avakyan et al., 1998] Avakyan, S. et al. (1998). Collision processes and excitation of UV emission from planetary atmospheric gases: a handbook of cross sections. *Collision processes and excitation of UV emission from planetary atmospheric gases: a handbook of cross sections/SV Avakyan...[et al.]; edited by SV Avakyan. Amsterdam*.

[Barth et al., 1969] Barth, C., Fastie, W., Hord, C., Pearce, J., Kelly, K., Stewart, A., Thomas, G., Anderson, G., and Raper, O. (1969). Mariner 6: Ultraviolet spectrum of Mars upper atmosphere. *Science*, 165(3897):1004–1005.

[Barth et al., 1971] Barth, C., Hord, C., Pearce, J., Kelly, K., Anderson, G., and Stewart, A. (1971). Mariner 6 and 7 ultraviolet spectrometer experiment: Upper atmosphere data. *Journal of Geophysical Research*, 76(10):2213–2227.

[Barth et al., 1973] Barth, C. A., Hord, C. W., Stewart, A. I., Lane, A. L., Dick, M. L., and Anderson, G. P. (1973). Mariner 9 ultraviolet spectrometer experiment: Seasonal variation of ozone on Mars. *Science*, 179(4075):795–796.

[Bertaux et al., 2006] Bertaux, J.-L., Korablev, O., Perrier, S., Quemerais, E., Montmessin, F., Leblanc, F., Lebonnois, S., Rannou, P., Lefèvre, F., Forget, F., et al. (2006). SPICAM on Mars Express: Observing modes and overview of UV spectrometer data and scientific results. *Journal of Geophysical Research: Planets*, 111(E10).

[Bhattacharyya et al., 2017] Bhattacharyya, D., Clarke, J., Bertaux, J.-L., Chaufray, J.-Y., and Mayyasi, M. (2017). Analysis and modeling of remote observations of the Martian hydrogen exosphere. *Icarus*, 281:264–280.

[Cox et al., 2010] Cox, C., Gérard, J.-C., Hubert, B., Bertaux, J.-L., and Bougher, S. W. (2010). Mars ultraviolet dayglow variability: SPICAM observations and comparison with airglow model. *Journal of Geophysical Research: Planets*, 115(E4).

[Feldman et al., 2000] Feldman, P. D., Burgh, E. B., Durrance, S. T., and Davidsen, A. F. (2000). Far-ultraviolet spectroscopy of Venus and Mars at 4 Å resolution with the Hopkins Ultraviolet Telescope on Astro-2. *The Astrophysical Journal*, 538(1):395.

[Finlayson-Pitts and Pitts, 2000] Finlayson-Pitts, B. J. and Pitts, J. N. (2000). Spectroscopy and photochemistry. In *Chemistry of the Upper and Lower Atmosphere*, pages 43–85. Elsevier.

[Fox and Dalgarno, 1979] Fox, J. L. and Dalgarno, A. (1979). Ionization, luminosity, and heating of the upper atmosphere of Mars. *Journal of Geophysical Research: Space Physics*, 84(A12):7315–7333.

[Gallagher et al., 1988] Gallagher, J., Brion, C., Samson, J., and Langhoff, P. (1988). Absolute cross sections for molecular photoabsorption, partial photoionization, and ionic photofragmentation processes. *Journal of physical and chemical reference data*, 17(1):9–153.

[Gérard, 1982] Gérard, J.-C. (1982). The Martian airglow and scattered sunlight: Future observations from a spinning orbiter. *The Planet Mars*, 185:73–81.

[Gérard et al., 2021] Gérard, J.-C., Aoki, S., Gkouvelis, L., Soret, L., Willame, Y., Thomas, I., Depiesse, C., Ristic, B., Vandaele, A., Hubert, B., et al. (2021). First observation of the oxygen 630 nm emission in the Martian dayglow. *Geophysical Research Letters*, 48(8):e2020GL092334.

[Gérard et al., 2020] Gérard, J.-C., Aoki, S., Willame, Y., Gkouvelis, L., Depiesse, C., Thomas, I., Ristic, B., Vandaele, A. C., Daerden, F., Hubert, B., et al. (2020). Detection of green line emission in the dayside atmosphere of Mars from NOMAD-TGO observations. *Nature Astronomy*, 4(11):1049–1052.

[Gérard et al., 2019] Gérard, J.-C., Gkouvelis, L., Ritter, B., Hubert, B., Jain, S., and Schneider, N. (2019). MAVEN-IUVS observations of the $CO_2{}^+$ UV doublet and CO Cameron bands in the Martian thermosphere: Aeronomy, seasonal, and latitudinal distribution. *Journal of Geophysical Research: Space Physics*, 124(7):5816–5827.

[Gkouvelis et al., 2018] Gkouvelis, L., Gérard, J.-C., Ritter, B., Hubert, B., Schneider, N., and Jain, S. (2018). The O($^1$S) 297.2-nm dayglow emission: a tracer of $CO_2$ density variations in the Martian lower thermosphere. *Journal of Geophysical Research: Planets*, 123(12):3119–3132.

[Gkouvelis et al., 2020] Gkouvelis, L., Gérard, J.-C., Ritter, B., Hubert, B., Schneider, N., and Jain, S. (2020). Airglow remote sensing of the seasonal variation of the Martian upper atmosphere: MAVEN limb observations and model comparison. *Icarus*, 341:113666.

[Haberle, 2015] Haberle, R. (2015). Solar system/Sun, atmospheres, evolution of atmospheres— Planetary atmospheres: Mars.

[Haberle et al., 2017] Haberle, R. M., Clancy, R. T., Forget, F., Smith, M. D., and Zurek, R. W. (2017). *The atmosphere and climate of Mars*. Cambridge University Press.

[Holsclaw et al., 2021] Holsclaw, G. M., Deighan, J., Almatroushi, H., Chaffin, M., Correira, J., Evans, J. S., Fillingim, M., Hoskins, A., Jain, S. K., Lillis, R., et al. (2021). The Emirates Mars Ultraviolet spectrometer (EMUS) for the EMM mission. *Space Science Reviews*, 217:1–49.

[Hubert et al., 2022] Hubert, B., Munhoven, G., Moulane, Y., Hutsemekers, D., Manfroid, J., Opitom, C., and Jehin, E. (2022). Analytic and numerical methods for the abel transform of exponential functions for planetary and cometary atmospheres. *Icarus*, 371:114654.

[Inn, 1964] Inn, E. C. (1964). Martian airglow. *Journal of Atmospheric Sciences*, 21(2):220–221.

[Korablev et al., 2006] Korablev, O., Bertaux, J.-L., Fedorova, A., Fonteyn, D., Stepanov, A., Kalinnikov, Y., Kiselev, A., Grigoriev, A., Jegoulev, V., Perrier, S., et al. (2006). SPICAM IR acousto-optic spectrometer experiment on Mars Express. *Journal of Geophysical Research: Planets*, 111(E9).

[Krasnopolsky and Gladstone, 1996] Krasnopolsky, V. and Gladstone, G. (1996). Helium on Mars: EUVE and PHOBOS data and implications for Mars' evolution. *Journal of Geophysical Research: Space Physics*, 101(A7):15765–15772.

[Krasnopolsky, 2010] Krasnopolsky, V. A. (2010). Venus night airglow: Ground-based detection of OH, observations of $O_2$ emissions, and photochemical model. *Icarus*, 207(1):17–27.

[Krasnopolsky, 2013] Krasnopolsky, V. A. (2013). *Photochemistry of the Atmospheres of Mars and Venus*, volume 13. Springer Science & Business Media.

[Krasovskij and Sefov, 1965] Krasovskij, V. and Sefov, N. (1965). Airglow. *Space Science Reviews*, 4:176–198.

[Lawrence, 1972] Lawrence, G. M. (1972). Photodissociation of $CO_2$ to produce CO(a 3Π). *The Journal of Chemical Physics*, 56(7):3435–3442.

[Leblanc et al., 2006] Leblanc, F., Chaufray, J.-Y., Lilensten, J., Witasse, O., and Bertaux, J.-L. (2006). Martian dayglow as seen by the spicam uv spectrograph on mars express. *Journal of Geophysical Research: Planets*, 111(E9).

[Lee et al., 2022] Lee, R. A., Ajello, J. M., Malone, C. P., Evans, J. S., Veibell, V., Holsclaw, G. M., McClintock, W. E., Hoskins, A. C., Jain, S. K., Gérard, J.-C., et al. (2022). Laboratory study of the Cameron bands and UV doublet in the middle ultraviolet 180–300 nm by electron impact upon $CO_2$ with application to Mars. *The Astrophysical Journal*, 938(2):99.

[McClintock et al., 2015] McClintock, W. E., Schneider, N. M., Holsclaw, G. M., Clarke, J. T., Hoskins, A. C., Stewart, I., Montmessin, F., Yelle, R. V., and Deighan, J. (2015). The imaging ultraviolet spectrograph (IUVS) for the MAVEN mission. *Space Science Reviews*, 195:75–124.

[Montmessin et al., 2017] Montmessin, F., Korablev, O., Lefèvre, F., Bertaux, J.-L., Fedorova, A., Trokhimovskiy, A., Chaufray, J.-Y., Lacombe, G., Reberac, A., Maltagliati, L., et al. (2017). SPICAM on Mars Express: A 10 year in-depth survey of the Martian atmosphere. *Icarus*, 297:195–216.

[Newcomb, 1901] Newcomb, S. (1901). A rude attempt to determine the total light of all the stars. *The Astrophysical Journal*, 14:297.

[Owen, 1982] Owen, T. (1982). The composition of the Martian atmosphere. *Advances in Space Research*, 2(2):75–80.

[Piqueux et al., 2015] Piqueux, S., Byrne, S., Kieffer, H. H., Titus, T. N., and Hansen, C. J. (2015). Enumeration of mars years and seasons since the beginning of telescopic exploration. *Icarus*, 251:332–338.

[Siddiqi, 2018] Siddiqi, A. A. (2018). *Beyond Earth: A chronicle of deep space exploration, 1958-2016*, volume 4041. National Aeronautis & Space Administration.

[Silverman, 1970] Silverman, S. (1970). Night airglow phenomenology. *Space Science Reviews*, 11(2-3):341–379.

[Soret et al., 2022] Soret, L., Gérard, J.-C., Aoki, S., Gkouvelis, L., Thomas, I., Ristic, B., Hubert, B., Willame, Y., Depiesse, C., Vandaele, A., et al. (2022). The Mars oxygen visible dayglow: A Martian year of NOMAD/UVIS observations. *Journal of Geophysical Research: Planets*, 127(6):e2022JE007220.

[Soret et al., 2023] Soret, L., Gérard, J.-C., Hubert, B., Vandaele, A., Thomas, I., Ristic, B., Willame, Y., Schneider, N., Jain, S., Gupta, S., et al. (2023). The ultraviolet Martian dayglow observed with NOMAD/UVIS on ExoMars Trace Gas Orbiter. *Journal of Geophysical Research: Planets*, page e2023JE007762.

[Stewart et al., 1972] Stewart, A. I., Barth, C., Hord, C., and Lane, A. (1972). Mariner 9 ultraviolet spectrometer experiment: Structure of Mars' upper atmosphere. *Icarus*, 17(2):469–474.

[Stiepen, 2014] Stiepen, A. (03 April 2014). *Dynamique et composition des atmosphères supérieures de Mars et Vénus observées par les spectrographes ultraviolets à bord de Mars Express et Vénus Express*. PhD thesis, ULiège - Université de Liège.

[Stiepen et al., 2015] Stiepen, A., Gérard, J.-C., Bougher, S., Montmessin, F., Hubert, B., and Bertaux, J.-L. (2015). Mars thermospheric scale height: CO Cameron and $CO_2{}^+$ dayglow observations from Mars Express. *Icarus*, 245:295–305.

[Tarasashvili et al., 2013] Tarasashvili, M., Sabashvili, S. A., Tsereteli, S., and Aleksidze, N. (2013). New model of mars surface irradiation for the climate simulation chamber 'artificial mars'. *International Journal of Astrobiology*, 12(2):161–170.

[Villanueva et al., 2015] Villanueva, G. L., Altieri, F., Clancy, T. R., Encrenaz, T., Fouchet, T., Hartogh, P., Lellouch, E., Lopez-Valverde, M. A., Mumma, M. J., Novak, R. E., et al. (2015). Unique spectroscopy and imaging of Mars with JWST. *arXiv preprint arXiv:1510.04619*.

[Willame et al., 2022] Willame, Y., Depiesse, C., Mason, J. P., Thomas, I. R., Patel, M. R., Hathi, B., Leese, M. R., Bolsée, D., Wolff, M. J., Trompet, L., et al. (2022). Calibration of the NOMAD-UVIS data. *Planetary and Space Science*, 218:105504.